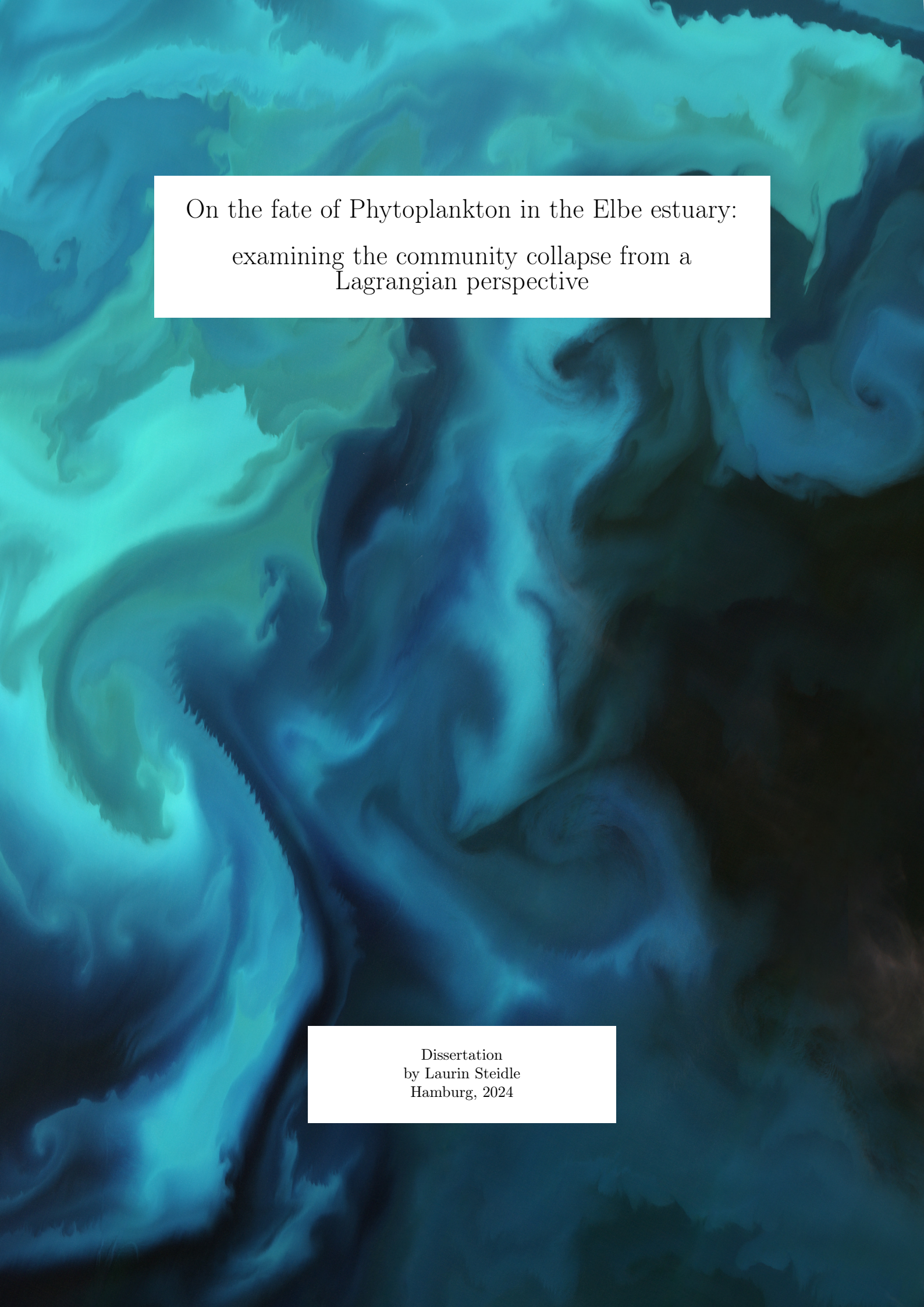

On the fate of Phytoplankton in the Elbe estuary:

examining the community collapse from a Lagrangian perspective

Dissertation
by Laurin Steidle
Hamburg, 2024

On the fate of Phytoplankton in the Elbe estuary: examining the community collapse from a Lagrangian perspective

Dissertation
with the aim of achieving a doctoral degree
at the Faculty of Mathematics, Informatics and Natural Sciences
Department of Earth Sciences
at Universität Hamburg

submitted by
Laurin Steidle

Hamburg, 2024

On the fate of Phytoplankton in the Elbe estuary: examining the community collapse from a Lagrangian perspective

ein Beitrag zum Dissertationsthema:

Ecosystem Modelling to assess carbon fluxes in estuarine channels

Department of Earth Sciences

Date of Oral Defense:	6. September 2024
Reviewers:	Prof. Dr. Inga Hense
	Dr. Johannes Pein
Members of the examination commission:	Prof. Dr. Lars Kutzbach
	Prof. Dr. Inga Hense
	Dr. Johannes Pein
	Prof. Dr. Elisa Schaum
	Dr. Ross Vennell
Chair of the Subject Doctoral Committee Earth System Sciences:	Prof. Dr. Hermann Held
Dean of Faculty MIN:	Prof. Dr.-Ing. Norbert Ritter

Eidesstattliche Versicherung | Declaration on Oath

Hiermit erkläre ich an Eides statt, dass ich die vorliegende Dissertationsschrift selbst verfasst und keine anderen als die angegebenen Quellen und Hilfsmittel benutzt habe.

I hereby declare upon oath that I have written the present dissertation independently and have not used further resources and aids than those stated.

Ort, den | City, date

Unterschrift | Signature

für Sina

Abstract

This dissertation aims to advance modeling capabilities in estuarine contexts and study phytoplankton community fate in the Elbe estuary. Eutrophication effects cause large upstream blooms that collapse in the deep, turbid waters of Hamburg's port, leading to oxygen depletion and environmental concerns. The prevailing narrative attributes this collapse primarily to zooplankton grazing, but we argue that underlying processes causing the mortality are not sufficiently well understood, necessitating improvements in estuarine ecosystem modeling.

To address this, we have developed a Lagrangian model of the Elbe estuary by extending the Oceantracker modeling framework to provide a new perspective on these problems. Our model offers improved performance, outperforming its closest alternative by over an order of magnitude, while providing a more accurate representation of key physical processes and maintaining flexibility.

Using this model, we challenge the prevailing narrative that phytoplankton collapse is primarily due to grazing pressure. Instead, we propose that collapse may be partly due to aggregation of phytoplankton with inorganic suspended sediment, resulting in sinking aggregates and light-limiting conditions in the highly turbid shipping channel. To test this, we incorporated an aggregation model into OceanTracker and evaluated different mortality mechanisms. Our results suggest that this aggregation process may play a significant role, especially for larger aggregates (50 µm), suggesting that light limitation-induced mortality may be more important than previously thought. This suggests that effective turbidity management in the fairway may be crucial for the maintenance of the phytoplankton community.

Furthermore, our study of phytoplankton retention mechanisms revealed that shallow marshes and mudflats are vital for the survival of the phytoplankton community in the Elbe estuary. These areas allow phytoplankton to persist through periods of stranding and resuspension. We suggest that careful management of these areas is essential for the long-term stability and resilience of the phytoplankton community in the estuary. We strive to bring new impulses, both in the field of Lagrangian modeling in coastal and estuarine environments and in ecosystem management of the Elbe estuary.

Zusammenfassung

Im Laufe der Jahrhunderte haben antropogene Einflüsse das Elbestuar erheblich verändert. Dazu gehören der Bau von Deichen zur Landgewinnung und zum Schutz vor Stürmen sowie das Ausbaggern der Fahrrinne, die sich von der Nordsee bis zum Hamburger Hafen erstreckt. Diese Veränderungen bringen eine Vielzahl von Umweltauswirkungen mit sich, die häufig zu Konflikten zwischen den beteiligten Interessenvertreter führen, wobei die jüngste Vertiefung der Fahrrinne ein aktuelles, kontroverses Beispiel ist. Die Auswirkungen auf das Ökosystem sind oft schwer vorherzusagen und werden nach der Fertigstellung nur selten verifiziert. Wir sind der Meinung, dass Fortschritte bei der Modellierung von Ökosystemen erforderlich sind, um die Auswirkungen von Ökosystemprojekten und des Klimawandels besser zu verstehen und vorherzusagen.

Die Eutrophierung, die durch landwirtschaftliche Abwässer im Einzugsgebiet verursacht wird, führt zu großen Phytoplanktonblüten in den flussaufwärts gelegenen Flüssen. Diese Phytoplanktongemeinschaft bricht jedoch schnell zusammen, wenn sie die tiefen und trüben Gewässer des Hamburger Hafens erreicht. Die daraus resultierende Sauerstoffverarmung, aufgrund der Remineralisierung des abgestorbenen Phytoplanktons, ist ein großes Problem für die Gesundheit des Ästuar-Ökosystems. Die vorherrschende Meinung führt diesen Kollaps in erster Linie auf das Abweiden des Zooplanktons zurück. Wir sind jedoch der Meinung, dass die zugrundeliegenden Prozesse, die die Mortalität verursachen, nicht hinreichend verstanden sind. Das Verständnis dieser Prozesse ist jedoch entscheidend für eine angemessene Bewirtschaftung des Ästuars und unterstreicht die dringende Notwendigkeit, unser Verständnis des Ästuar-Ökosystems und unsere Modellierungsmöglichkeiten zu verbessern.

Um dieses Problem anzugehen, haben wir ein Lagrangesches Modell des Elbe-Ästuars entwickelt, indem wir das Oceantracker-Modell erweitert haben, um eine neue Perspektive auf diese Probleme zu ermöglichen. Unser Modell ist leistungsfähiger und übertrifft seine engste Alternative um mehr als eine Größenordnung, während es gleichzeitig eine genauere Darstellung der wichtigsten physikalischen Prozesse bietet und dabei flexibel bleibt.

Mithilfe dieses Modells stellen wir die vorherrschende Meinung in Frage, dass der Kollaps des Phytoplanktons in erster Linie auf Zooplankton zurückzuführen ist. Stattdessen vermuten wir, dass der Kollaps zum Teil auf die Aggregation von Phytoplankton mit anorganischen Schwebstoffen zurückzuführen sein könnte, was zu sinkenden Aggregaten und lichtlimitierenden Bedingungen in der stark getrübten Fahrrinne führt. Um dies zu testen, haben wir ein Aggregationsmodell in OceanTracker integriert und verschiedene Mortalitätsmechanismen bewertet. Unsere Ergebnisse deuten darauf hin, dass dieser Aggregationsprozess und die von ihnen verursachte Mortalität durch Lichtlimitierung eine bedeutende Rolle spielen kann, insbesondere bei größeren Aggregaten (50 µm). Dies deutet darauf hin, dass ein wirksames Trübungsmanagement in der Fahrrinne für die Erhaltung der Phytoplanktongemeinschaft von entscheidender Bedeutung sein könnte.

Darüber hinaus hat unsere Studie über die Mechanismen der Phytoplanktonrückhaltung

gezeigt, dass flache Marsch- und Wattflächen für das Überleben der Phytoplanktongemeinschaft im Elbeästuar von entscheidender Bedeutung sind. Diese Gebiete ermöglichen es dem Phytoplankton, durch regelmäßiges stranden und resuspendieren zu überleben. Wir vermuten, dass eine sorgfältiges Managment dieser Gebiete für eine langfristige Stabilität und Widerstandsfähigkeit der Phytoplanktongemeinschaft im Ästuar unerlässlich ist. Mit dieser Arbeit möchten wir neue Impulse, sowohl auf dem Gebiet der Lagrange'schen Modellierung von Küsten- und Ästuarumgebungen als auch für das Ökosystemmanagement des Elbästuars setzten.

Contents

Chapter 1

Introduction

1.1 Ecology, ecosystems and their management

During the 1960s, ecological issues such as air and water pollution, deforestation, and loss of biodiversity became an increasingly apparent side effect of industrialization and population growth, fueling an environmental movement in both the scientific ecological community and the public at large (McIntosh, 1985, p. 308). As the vulnerability of these ecosystems became apparent, so did the need for their management. Although there is ongoing debate about the objectives and strategies, ecosystem management has now become a common practice.

In recent decades, ecosystem management has focused primarily on either maintaining or restoring existing systems. However, there is a growing trend to evaluate these efforts not only for their environmental benefits, but also for their potential to mitigate climate change impacts through carbon sequestration. This shift reflects a growing awareness that "healthy" ecosystems - those that are stable and resilient (Karr, 1999) - play a critical role in capturing and storing carbon dioxide, the primary greenhouse gas. Consequently, strategies to optimize ecosystem functions specifically to enhance carbon sequestration are gaining attention (Birkhofer et al., 2015). For example, there is concern about the melting of permafrost in Siberia, not only because of ecosystem changes due to anthropogenic pressures, but also because of the expected release of methane, which could further accelerate climate change (McGuire et al., 2018).

In January 2024, the 1.5 degree maximum global warming target set by the Paris Agreement was exceeded (Cop). This milestone has profound implications for global ecosystems, pushing many beyond their natural equilibrium and making traditional conservation strategies increasingly unfeasible. A prominent example is the continuing decline of coral reefs, which are particularly sensitive to rising ocean temperatures. Warming oceans cause coral bleaching,and ultimately lead to their death. It is expected that most of the world's coral reefs will be lost even if the increase in global mean temperature is limited to 2 degrees Celsius (Frieler et al., 2013). A similar fate is expected for many other ecosystems, which are being pushed out of their natural equilibrium by climate change (Hooper et al., 2012).

Unsurprisingly, there is a growing interest in reshaping remaining ecosystems or replacing lost ones to enhance their carbon sequestration capabilities. Research efforts have been conducted to evaluate the increased global carbon sink potential of ecosystems under more "optimal" management strategies (Kooten and Sohngen, 2007; Noormets et al., 2014; Sha et al., 2022). Given these developments, we suspect that ecosystem management is on the verge of a global paradigm shift.

However, engineering ecosystems requires a deeper understanding of the underlying ecological processes to avoid unintended consequences and achieve desired outcomes (Naeem et al., 2015). Traditionally, ecosystem management has had relatively simple objectives: either to protect ecosystems from external disturbances caused by human activities or other "non-natural" events such as invasive species, or, in the case of restoration, to reverse imposed changes (Beller et al., 2020). By definition, ecosystem engineering will push these systems out of their current, relatively well-understood steady states into new and unknown conditions where existing ecological principles may no longer apply. Consequently, this transition will require that these systems be understood and modeled with a more holistic approach and greater accuracy than before (Naeem et al., 2015).

One of the earliest and most notable attempts at ecosystem engineering was the 1996 "IRONEX" experiment, which explored the potential of iron fertilization. The open ocean is the largest sequesterer of carbon. It is estimated that the oceans absorb about 3 Gt of carbon per year, compared to about 2 Gt per year by the terrestrial biosphere of the 9 Gt of anthropogenic carbon emissions (Friedlingstein et al., 2022; Planchat et al., 2023). This made the oceans an attractive target for large-scale engineering projects. IRONEX attempted to increase the ocean's carbon sequestration potential by fertilizing the growth of phytoplankton, which would bind dissolved carbon in the ocean through photosynthesis and eventually transport it to the ocean floor. While the experiment successfully increased phytoplankton growth, subsequent research questioned the overall effectiveness of the method and raised concerns about its economic feasibility, potential side effects, and the political implications of such projects. Research continued, and after controversial discussions, a moratorium was placed on large-scale non-scientific iron fertilization projects in 2008 (Cullen and Boyd, 2008).

Ecosystems have also often been "inadvertently" engineered to achieve other goals. A large-scale example is the Dutch "Delta Works", a series of dikes and sluices built after the devastating 1953 storm surge to protect the Dutch coastline in the delta between Antwerp and Rotterdam (Pilarczyk, 2012). Most of the planning was done in the 1950s and 1960s, a time when environmental concerns were less important. As a result, major changes to the ecosystem were considered acceptable side effects rather than intended outcomes (Smaal et al., 1991; Nienhuis et al., 1994).

A somewhat similar engineering process took place in the Elbe estuary. In this case, however, the goal was not to keep the sea out, but to let it in, to improve access to the port of Hamburg for larger ships. Since the beginning of the 20th century, the main channel of the estuary has been dredged from a depth of about 5 to nearly 20 meters, with the most recent dredging campaign ending in 2021. Historically, ecosystem impacts have been an afterthought. However, the last dreadging campaign has been controversial and was one of the most contested infrastructure projects in Germany in recent years (Hein and Thomsen, 2023). While such trade-offs can of course be considered accaptable, it is often difficult to predict the extent of the impact of such projects on the ecosystem accurately and only rarely are they actually audited post completion (Gray, 2000).

We think that the Elbe estuary is a prime example of the challenges that come with ecosystem engineering. The estuary is a complex system with a long history of human intervention. It is well studies with long term observational data sets on many aspects of the physical and biochemical system. State-of-the-art coupled hydrodynamic-biogeochemical models have been developed and used to examine and predict many facets of the system. Nevertheless, significant challenges and uncertainties remain in understanding and managing the estuary which shows the difficulty of predicting the effects of ecosystem engineering on complex systems.

1.2 The Elbe estuary

In this work we will focus exclusively on the Elbe estuary. Originating in the Czech Republic, the Elbe River stretches 1094 km with a catchment area of 148 000 km^2, two-thirds of which is in Germany. Approximately 24.5 million people live in this catchment area. The Elbe estuary itself is about 140 km long and is characterized by tidal influences.

The Elbe is a lowland river, with only about half of its length rising above 200 m above sea level. The temperate climate of the region sees average air temperatures of 8 °C to 9 °C in the lowlands, and the highest flows typically occur in the spring. At Geesthacht Weir, the last gauge upstream of the tidal limit, the long-term mean freshwater discharge is 713 $m^3 s^{-1}$, with summer low flows averaging 301 $m^3 s^{-1}$ and winter high flows reaching 1870 $m^3 s^{-1}$ (HPA, 2014). The estuary, is typcally described as a well-mixed mesotidal or macrotidal coastal plain estuary, but effects of stratification during the summer months have been described as well (Holzwarth and Wirtz, 2018; Kappenberg and Grabemann, 2001; Middelburg and Herman, 2007; Pein et al., 2021). The estuarine delta extends 100 km inland to the Port of Hamburg, Germany's largest seaport and the third largest container port in Europe and rank 21 in the world (Nightingale, 2022).

Human activities have significantly altered the Elbe estuary over the centuries. Diking and drainage began around 1000 AD, and the first permanent port was established in the 12th century located at the river mouths of the tributaries Alster and Bille (Krieger, 2006). Reclamation of tidal marshes began in the 13th century (Renes, 2013), accelerated with industrialization about 150 years ago, and accelerated further since the 1960s (Hein and Thomsen, 2023).

Technological advances allowed for major hydrological interventions, including channel dredging and large-scale land reclamation projects (Ratter and Weig, 2012). Since 1868, there have been nine fairway adjustments, increasing its depth from about five meters in 1818 to 18 meters in 2022 (Boehlich and Trotmann, 2008, p. 302). The widening and deepening of the fairway, together with the reclamation of tidal floodplains - especially after the 1962 storm surge - have had a profound environmental impact and widened the tidal range.

In addition to geometric changes, human activities have significantly affected the biochemistry of the region's waters, with the most pronounced impacts on water quality observed in the 1980s before German reunification, when the highest levels of organic pollutants, phosphorus, and contaminants were recorded. Since then, water quality has generally improved. Yet, concentrations of nitrate and certain heavy metals remain elevated (Pusch and Fischer, 2006).

Elevated nutrient levels, specifically total nitrogen and total phosphorus, combined with favorable light conditions and prolonged retention times in river reaches, facilitate increased limnic primary production. (Pusch and Fischer, 2006; Quiel et al., 2011). Upon arrival in the turbid estuary, phytoplankton encounter unfavorable conditions, particularly in terms of light availability, resulting in a rapid decline in phytoplankton concentration. The resulting detriPtus is heterotrophically degraded, which consistently leads to the formation of an oxygen minimum zone (OMZ) in the freshwater section of the estuary during summer (Bergemann et al., 1996; Schroeder, 1997; Amann et al., 2014).

Phytoplankton, essential microscopic autotrophic organisms, play a central role in aquatic ecosystems. Primarily drifting in the water, the name "phytoplankton" is derived from the Greek words *phyton*, meaning "plant", and *planktos*, meaning "wanderer" or "drifter". They perform photosynthesis, using sunlight to convert carbon dioxide into organic compounds while releasing oxygen. Through this process, they introduce energy into the system and are often considered the base of the food chain and referred to as primary producers. Phytoplankton are

highly sensitive to environmental factors such as light availability, nutrient levels, temperature, and salinity, making them valuable indicators of ecosystem health and productivity (Winder and Sommer, 2012).

Due to high nutrient loads, phytoplankton is proliferating in the Elbe River. Phytoplankton concentrations, indicated by chlorophyll-a, increase from a seasonal mean of $45\,\mu g\,L^{-1}$ (April-October, 1994-2006) at km 375 from the source in Schmilka to $128\,\mu g\,L^{-1}$ at km 846 in Schnackenburg, with peak concentrations exceeding $300\,\mu g\,L^{-1}$. (Pusch and Fischer, 2006; Quiel et al., 2011). These high values are typically observed during the summer months, when high light availability, warm temperatures and low flow velocities favor primary production.

Centric diatoms (e.g. Stephanodiscus) are the dominant phytoplankton group, accounting for about half of the biovolume. Recent results from a metabarcoding study (Martens et al., 2024) suggest that picophytoplankton and flagellates with potential for mixotrophy (e.g., cryptophytes) also play important roles and are currently underrepresented in microscopic datasets. Picophytoplankton and mixotrophic flagellates are particularly ecologically important in the mid to lower estuary, where high turbidity creates unfavorable living conditions and capabilities such as phagotrophy provide fundamental advantages.

Upon reaching the Port of Hamburg phytoplankton concentration drops suddenly. A strong correlation with depth suggests that the collapse may be caused directly or indirectly by the bathymetric jump i.e. the increase in depth from the upstream river to the navigational channel (Schroeder, 1997). Measurements of low oxygen concentrations (<3mg/l) and high ammonium ($15 mmol m^{-3}$) concentrations at the bottom and high disolved inorganic nitrogen downstream of the bathymetric jump suggest a high remineralisation rate of organic matter (Schroeder, 1997; Holzwarth and Wirtz, 2018; Sanders et al., 2018; Spieckermann et al., 2022). This indicates that upstream phytoplankton is not being diluted or vertically dispersed in a way that allows it to elude the monitoring stations, but is actually dyingTheir The collapse of the phytoplankton community in the Elbe estuary has been consistently observed in chlorophyll concentrations since at least the 1980s (Schöl et al., 2014). Looking at this trend over time we see that this effect has increased over recent years and shows to be correlated with the increase in turbidity which has more then tripled since 2010 (Weilbeer et al., 2021)

Most studies suggest that the phytoplankton collapse in the Elbe is due to grazing or light limitation. The *grazing hypothesis* assumes that most of the phytoplankton is consumed by zooplankton. A common explanation (Schöl et al., 2014; Kopmann and für Wasserbau, 2014; Pein et al., 2019) is that marine zooplankton are pushed into the estuary with the tides up to the bathymetric jump. Upstream of the bathymetric jump, the flow velocity is much higher, making it difficult for them to migrate further upstream. This could explain the sudden drop in phytoplankton concentration in this area. Although marine zooplankton species have been observed in this area, (Steidle and Vennell, 2024) showed that retention in this area without a sophisticated mechanism is difficult for planktonic organisms. Hence, an accumulations of marine zooplankton to large enough concentrations that could explain this drop in chlorophyll concentrations might not be possible. This suggest that the grazing hypothesis might instead be dependant on upstream freshwater zooplankton that could still easily survive in the low salinity port area. Alternatively, the grazing pressure could be in part due to benthic grazers. With much lower flow velocities close to the bed and a potential ability to hold on or even burry themselves in the sediments they would have a much easier time to persist in that area. Informal reports of there existance have been made but no systematic study has been performed to date to try and quantize their abundance.

The last zooplankton survey that could be used to examine the effect of zooplankton grazing has been performed in 1992 (Bernat et al., 1994) with a small unpublished survey

mentioned in (Schöl et al., 2014) At that time the bathymetry was significantly different with a narrower navigational channel and a target depth of 13m instead of the current 18m (Hein and Thomsen, 2023). Additionally the upstream biochemistry has changed significantly since the collapse of the German Democratic Republic (GDR) with a drastic increase in water quality and a corresponding increase in in upstream chlorophyll concentrations (Adams et al., 1996; Matthies et al., 2006). This effectively leaves us in the dark about the current impact of grazing on the chlorophyll concentrations.

The *light limitation* hypothesis is based on the sudden increase in turbidity downstream of the bathymetric jump and the sharp decrease in mean downstream velocity and corresponding increase in residence time. This increase in turbidity in turn increased the aphotic to photic volume ratio, effectively reducing light availability for phytoplankton. Note that the turbidity in the navigational channel is so high that water at a depth of bewlow two meters is aphotic (below 1% of surface light). However, a 1D-modelling study by (Schroeder, 1997), and the light limitation induced mortility rates measured by (Walter et al., 2017) suggest that light limitation alone would be too slow to explain the sudden drop in phytoplankton concentrations around the bathymetric jump. Instead, it could be explained with a combination of light limitation, grazing, and the sharp decrease in downstream velocity. While light limitation restricts most of the phytoplankton growth, the decrease of the downstream velocity drastically increases residence times around the bathymetric jump. Combining this with an grazing pressure from upstream zooplankton could cause the sudden drop of the phytoplankton community. Typically chlorophyll concentrations are presented relative to the position along the channel obscuring the shift in residence times between these to regions which might in part explain the perceived suddenes of this effect.

While the collapse of the phytoplankton community in itself can be considered a significant issue, it creates the additional problem of oxygen deficits. Fertilizer run off in the catchment area leads to large phytoplankton blooms in the river section of the estuary causing large phytoplankton blooms in the estuary. Remineralization processes of the dead phytoplankton matter take up large portion of the dissolved oxygen in the water column. The low surface-to-volume ration in the channel does not allow for sufficient oxygen exchange with the atmosphere to compensate for this oxygen deficit resulting in anoxy conditions during summer. (Holzwarth and Wirtz, 2018). Dissolved oxygen is crucial for the survival for most aquatic species. Low dissolved oxygen concentrations can therefore have severe impacts on aquatic life. Most notably, the upstream migration of fish is hindered by low oxygen concentrations, reshaping the fish community in the estuary (Eick and Thiel, 2014; Hein and Thomsen, 2023).

In the past, financial interests - such as those of the Port of Hamburg and other large industrial entities - have often taken precedence over ecological conservation, leading to conflicts among stakeholders with competing interests. This prioritization has not only caused environmental problems, but also contributed to the decline of local industries, such as fishing, that depend on a healthy estuarine ecosystem.

Managing the estuary requires navigating a complex landscape of diverse, often conflicting stakeholder interests. There is an urgent need to improve our understanding of estuarine ecosystem processes in order to develop successful and sustainable management strategies. By delving deeper into these ecological dynamics, the goal is to strike a balance between supporting economic activities and preserving this vital ecological corridor. This approach is essential to address the increasing incidence of phytoplankton community collapse, the resulting anoxia and its impact on estuarine biodiversity and the livelihoods that depend on this ecosystem.

1.3 Elbe ecosystem models

1.3.1 Ecosystem models in the Elbe estuary

The estuarine environment is typically characterized by high-energy hydrodynamic processes driven by tides, water density differences, and river inflow. The complexity and variability of these processes usually require three-dimensional simulations of water movement, which include the transport of salinity and sometimes water temperature (Zhang et al., 2016; Warner et al., 2005; Gross et al., 2009; Sehili et al., 2014).

In recent decades, 3D hydrodynamic simulations have become standard practice. There has been a notable trend toward increasing the complexity of these models, as evidenced by the growing number of computational cells and the reduction of the maximum grid resolution. Common frameworks for high-resolution 3D hydrodynamic models include Delft3D, SCHISM, FVCOM, and UnTRIM (Ganju et al., 2016).

In contrast, modeling ecological processes is complicated by the inherent complexity of biological systems, limited understanding of some processes, and sparse availability of observational data. These challenges lead to over-parameterization, high model uncertainty, and error propagation (Ganju et al., 2016). In addition, the goal of developing models that are as general as possible for easy transferability (Evans et al., 2013) has hindered the establishment of 3D, high-resolution estuarine biogeochemical models in a manner similar to hydrodynamic models.

Currently, there are two major 3D coupled hydrodynamic-biogeochemical models maintained for the Elbe estuary: one developed by the Bundesanstalt für Wasserbau (BAW) and the other by the Helmholtz-Zentrum Hereon (formerly Helmholtz-Zentrum Geesthacht, HZG). The Federal Waterways Engineering and Research Institute (Bundesanstalt für Wasserbau - BAW) is a central technical and scientific higher federal authority supporting the Federal Ministry of Digital Affairs and Transport (Bundesministerium für Digitales und Verkehr - BMDV). As a central service provider, it advises and supports the ministry and the Federal Waterways and Shipping Administration (Wasserstraßen- und Schifffahrtsverwaltung des Bundes - WSV) in their hydraulic engineering tasks. Their model is therefore primarily designed to support the management of the Elbe estuary and can be considered the more conventional of the two.

The model is based on the UnTRIM hydrological model (Casulli, 2009; Casulli and Stelling, 2011) and is coupled with the Deltares water quality model (Postma et al., 2003; Blauw et al., 2009; Smits and van Beek, 2013). It is used to assess the impact of dredging campaigns on the estuary and to predict the effects of future interventions. The model can also use a sediment transport module called “SediMorph” to predict sediment transport and deposition. The unstructured orthogonal computational grid consists of approximately 11,000 horizontal elements with 25 subgrids per edge and a maximum of 31 vertical z-layers, each 1 meter thick. The model domain extends along the 170 km estuarine shipping channel from the tidal boundary to the end of the maintained shipping channel in the Inner German Bight in the North Sea (see Fig. 13a). The domain includes the entire volume between the main dikes and includes the eight largest tributaries of the estuary.

The Helmholtz Center Hereon (formerly HZG) focuses more on academic research without direct connection to the management of the estuary. It is based on the SCHISM model (Zhang et al., 2016) and coupled to the biogeochemical model ECOSMO (Schrum et al., 2006). We use the hydrodynamic data of the latest SCHISM model of the Elbe estuary (Pein et al., 2021) from the weir at Geesthacht to the North Sea, including several side channels and and the port area (see Fig. 2.20). SCHISM solves the Reynolds-averaged Navier-Stokes equations on unstructured meshes, assuming hydrostatic conditions and using a 60 s time step. The

unstructured mesh is three-dimensional and consists of 32,000 horizontal nodes with terrain coordinates based on the LSC2 technique (Zhang et al., 2016) for the vertical grid, with a maximum of a maximum of 20 levels. Regions with depths less than 2 m are resolved using only one vertical level. and have a horizontal resolution of 50 m in the German Bight, 10 m in the Elbe estuary, and 5 m in the Port of Hamburg (Stanev et al., 2019). The boundary include sea surface elevation, horizontal currents, salinity, and temperature (Stanev et al., 2019), and those on the landward side include the discharge and temperature of the Elbe River. Atmospheric forcing includes wind, air temperature, precipitation, and shortwave and longwave shortwave and longwave radiation (Stanev et al., 2019). Model validation is based on tide gauge stations and long-term stationary measurements of salinity, water temperature, and horizontal currents. Biochemical variables, including chlorophyll, are based on long-term measurements at the Seemannshöft and Grauerort stations (Pein et al., 2021). The model provides us with a node-based containing a range of information such as water velocity, salinity, water level, and dispersion. The year represented by this dataset is 2012.

The two previously mentioned BAW and Hereon models are Eulerian models. They describe the dynamics as concentration changes within volumes on a fixed grid, providing the perspective of a stationary observer. An alternative approach is the Lagrangian model, which takes the perspective of a small particle drifting through the water, describing the environment from the particle's point of view. This change of perspective has several advantages.

First, Lagrangian models allow us to represent certain individual-based processes that are difficult to describe from an Eulerian perspective. Typical examples in ecology include life cycle models, a type of individual-based model. In these models, a population is represented by a set of particles, each representing an individual or group of individuals whose behavior changes as a function of personal history. For example, in a study by (Hense and Beckmann, 2015), a population of diatoms is modeled where each individual's shell size decreases with each asexual reproductive cycle until a sexual reproductive cycle resets their size. Using a Lagrangian model allows for a straightforward representation of current size and life history, which would be cumbersome in an Eulerian model.

Second, Lagrangian models can be used to analyze Eulerian models. Large hydrodynamic models are often too complex to be fully understood in their entirety. Post-processing of their results is usually required to make sense of them, such as generating simple time and depth averages to produce 2D maps. Consider, for example, the analysis of the periodicity of a large ocean gyre. The flow field computed by an Eulerian model contains all the information needed to predict how long it will take the gyre to complete a full cycle. However, extracting this information directly from the 4D flow field (three spatial dimensions and one time dimension) is often impractical. Using a Lagrangian model, we can simplify this by releasing particles into the vortex and measuring how long they take to complete a lap around the vortex (Van Sebille et al., 2018).

Another common problem is the connectivity between two bodies of water. From an Eulerian perspective, one could track dye concentrations to see how much water flows from one body to the other. Alternatively, one could release particles and express the connectivity as the fraction of particles that reach the other body. A key advantage of Lagrangian models in such applications is their computational efficiency. Lagrangian models are typically orders of magnitude faster than Eulerian models because they can use pre-calculated flow fields generated by a previous Eulerian model. This computational efficiency allows Lagrangian models to be used for large-scale sensitivity studies or in real-time applications such as oil spill prediction (Van Sebille et al., 2018).

For the following work we will use a Lagrangian model based on the OceanTracker model first published in 2021 (Vennell et al., 2021). To represent the complex topology and resulting

physical features, estuarine models of the Elbe estuary use unstructured grids, also known as meshes. These unstructured meshes make particle tracking significantly more complicated and computationally expensive than structured meshes, primarily because many of the symmetries used to determine the particle's current grid cell are lost.

Of the 11 particle tracking models reviewed in (Van Sebille et al., 2018), only one, called OpenDrift (Dagestad et al., 2018), was able to handle unstructured grids. Counterintuitively, determining the current grid cell using OpenDrift's approach is actually the most computationally expensive step.

OceanTracker (Vennell et al., 2021) proposed a novel method to find the current cell of a particle by using its history, specifically its last location. Using a method described as a "barycentric walk", they were able to reduce the scaling of the computational cost of this step from $\mathcal{O}(\log n)$ to $\mathcal{O}(1)$, meaning that it scales from being logarithmically dependent on the number of grid cells to being independent of grid size. Using this method, they showed that OceanTracker could outperform OpenDrift by up to two orders of magnitude.

For our work, we have continued to develop OceanTracker, adding new functionality both on the physical side, such as dynamic dispersion based on eddy diffusivity, and on the biological side, such as particle splitting to represent phytoplankton growth.

1.3.2 Outline

This work focuses on the development of a new Lagrangian model of the Elbe estuary to study the fate of phytoplankton in this complex and dynamic environment. Our Lagrangian model will be based on the OceanTracker model (Vennell et al., 2021), taking advantage of its efficient particle tracking capabilities, and coupled with the SCHISM model of the Elbe estuary (Pein et al., 2021). which is known for its versatility in handling unstructured grids and detailed hydrodynamic simulations.

In our first study, we further developed OceanTracker, adding new functionalities to better represent both physical and biological processes as just described, which enabled us to study the ecosystem of the Elbe estuary from a Lagrangian point of view.

In our second study, we investigated the collapse of the phytoplankton community at the bathymetric jump - the increase in water depth from the upstream Elbe River to the estuarine shipping channel - which marks the beginning of the Port of Hamburg. Our research focused on how these altered conditions affected phytoplankton mortality, particularly through coagulation processes. We challenged the common explanation that phytoplankton loss at the bathymetric jump was due to grazing pressure from zooplankton and suggested that coagulation processes between phytoplankton and suspended sediment might be an important process to explain the collapse.

Our third study investigated the retention mechanisms of phytoplankton in the Elbe estuary. Using our extended Lagrangian model, we estimated outwash losses and identified critical regions where phytoplankton could persist. For this study, we put special emphasis on bathymetric interactions, especially stranding and resuspension processes of phytoplankton.

By integrating these new approaches, our model aims to provide deeper insights into the interactions between hydrodynamic and biological processes in the Elbe estuary. Understanding these interactions is vital for effective estuarine management strategies, particularly in addressing challenges such as habitat degradation, and the impact of human activities on the estuarine ecosystem. This approach seeks to aid in balance economic with the ecological interests in the Elbe estuary and to offer a new tool in the estuarine ecosystem managment in general.

Chapter 2

Studies

Study I Vennell, R., Steidle, L., Smeaton, M., Chaput, R., and Knight, B.: OceanTracker 0.5: Fast Adaptable Lagrangian Particle Tracking in Structured and Unstructured Grids (manuskript), 2024.

Contribution: Improving model performance, designing and running the performance comparisons with other models. Implementation of new features including biological and physical processes, i.e. particle splitting to represent reproduction. Writing the corresponding section in the manuscript and editing.

Study II Steidle, L., Pein, J., Vennell, R. and Burd, A.: Potential effects of coagulation processes on phytoplankton mortality in the Elbe estuary from a Lagrangian point of view, (manuskript), 2024.

Contribution: Design of the study concept and its implementation, aquired hydrodynamic data, development of the required biological model features, performing the simulations, post-processing, and visualization. Writing the of the manuskript.

Study III Steidle, L. and Vennell, R.: Phytoplankton retention mechanisms in estuaries: a case study of the Elbe estuary, Nonlin. Processes Geophys., 31, 151–164, https://doi.org/10.5194/npg-31-151-2024, 2024.

Contribution: Design of the study concept and its implementation, aquired hydrodynamic data, development of the required biological model features, performing the simulations, post-processing, and visualization. Writing the of the manuskript.

2.1 Study I:

Fast Adaptable Lagrangian Particle Tracking in Structured and Unstructured Grids

2.1.1 Asbtract

Particle tracking code is frequently used to compute where particles move within hydrodynamic ocean models. OceanTracker's code is designed to minimise the user effort required to obtain the statistics required about that movement. Firstly, by being computationally fast. This enables user to scale to large numbers of particles, to obtain better statistics or wider exploration of cases within acceptable run times. It is able to model 1 million particles for one one month in 48 min on a single core of a basic laptop computer. Secondly, OceanTracker can calculate multiple particle statistics during the computational run, eliminating the need to analyse large volumes of recorded particle track output. The adaptability of OceanTracker's modular computational-pipeline enables users to add and modify particle physics, behaviour and statistics. Coders and non-coders have access to the same adaptability with in-built components, as the computational-pipeline is entirely assembled from user given parameters, supplied as text file or Python dictionary. Coders can easily modify existing components through inheritance. OceanTracker currently supports ocean model data from unstructured grids (SCHSIM, FVCOM, DELFT3D-FM) and structured grids (ROMS).

2.1.2 Introduction

Particle tracking is key to answering many scientific and practical questions about bio-physical transport in the ocean (Lynch et al., 2014; Van Sebille et al., 2018). Questions might include, determining the movement of larvae, quantifying residence time (Lucas and Deleersnijder, 2020), the spread of pollution, or quantify connectivity between regions. Using physical drifters to answer these questions is currently limited by budget and logistics. Thus tracking large numbers of virtual particles advected by currents obtained from hydrodynamic ocean models is commonly used to answer many such questions. Some examples of ocean particle trackers are PARTRACK (Knight et al., 2009), LIGHT (Wolfram et al., 2015), OpenDrift (Dagestad et al., 2018) and Parcels (Delandmeter and Van Sebille, 2019). This paper outlines the features and structure of the latest version of the OceanTracker particle tracker (Vennell et al., 2021). OceanTracker is designed to minimise the time required to obtain the results needed by the user, while having a high level adaptability to build a "computational pipeline " customised to their specific needs. Minimising a user's time has two main components 1.) computationally fast code, 2.) minimising the time and effort required to post-process the computational outputs (see Sec. 2.1.3). OceanTracker takes a step towards addressing a major challenge in particle tracking: simulating billions of particles (Van Sebille et al., 2018). Its speed allows users to scale to millions of particles within acceptable run times. This scaling enables better estimates of particle statistics, such as heat-maps or connectivities. For example, large numbers are useful when estimating connectivities between regions, where connectivity is weak but the consequences are significant, such as the spread of invasive species. Scaling also facilitates a much wider exploration of particle behaviours (e.g. light dependent vertical velocities of larvae) and the sensitivity of results to parameters governing those behaviours.

Computational speed makes it possible to scale particle numbers on modest computer hardware. Table 2.1 shows that on the basic Laptop I, OceanTracker can compute one month of particle trajectories for 1 million particles in less than an hour on a single CPU. The comparison in Sec. 2.1.5 indicates that OpenDrift would require 32 hours to accomplish the same task. The times in Table 2.1 for computers with more CPUs and memory are not significantly faster. When more CPUs and RAM are available, OceanTracker enables the easy division of the required runs into separate cases, which can then be run in parallel to significantly reduce run times, see Sec. 2.1.5.

The second component of minimising a user's time and effort is that spent in post-processing. Having the computational speed to scale to millions of particles will produce large files containing the computed particle trajectories. The time needed to analyses these tracks to yield the required particle statistics becomes a major bottleneck for the user, along with the logistical issues of storing and accessing what may be terabytes of output for analysis. OceanTracker resolves both of these issues by recording particle statistics during the computational run, e.g. by counting particles inside grid cells "on-the-fly" to produce a heat-map, or counting particles inside polygons to calculate connectivities between regions, as shown in Fig. 2.1 and Sec. 2.1.4. On-the-fly statistics address the post-processing time and storage issues, as no particle trajectories need to be recorded, and the statistics outputs take up much less space than the particle trajectories from which they are calculated. On-the-fly statistics produce data volumes which are independent of the number of particles released.

A key aspect of OceanTracker is the ability for users to easily adapt how particles behave and the statistics calculated. To achieve this, OceanTracker is built around the concept of a *computational pipeline* , which is a set of components assembled into a sequence that carries out the user's particle tracking, as shown in Fig. 2.3 and Sec. 2.1.4. This pipeline is broken up into a series of configurable *roles*, into which the user adds the components required to implement

their particle tracking model, see Sec. 2.1.4. These roles include the physics of particle movement, dispersion or suspension, modifications to their trajectories due to behaviours (e.g. larvae settling within a polygon) and particle statistics. This approach allows users to add multiple versions of a component into some roles. This can reduce user effort; for example allowing them to have multiple release groups with different locations and release schedules, along with multiple on-the-fly statistics, all done within a single computational run.

A challenge in having an adaptable computational pipeline is to enable both coders and non-coders to access the same level of adaptability. For both, OceanTracker's computational pipeline is entirely constructed from a user-supplied set of *parameters* that define both which components are added to the computational pipeline and their individual settings (see Sec. 2.1.4). Figure 2.4 provides a minimal example of this, showing the same run executed either through coding, or from parameters supplied in one of two standard text file formats. Another advantage of this approach is it allows web-based particle tracking on-demand services to easily access the same level of computational pipeline adaptability, e.g. (Vennell et al., 2019).

A single particle tracking framework that works for both structured and unstructured grids simplifies the particle tracking process for users by having a uniform approach regardless of the hydrodynamic model underpinning their location of interest. Particle trackers for unstructured grid are rare due to the complexity involved in coding the movement and interpolations within the grid. A review of ocean Lagrangian analysis (Van Sebille et al., 2018) lists 11 particle trackers, of which only one is designed for use with unstructured grids. Those compatible with both types of grid are even rarer, e.g. OpenDrift (Dagestad et al., 2018). A secondary goal for OceanTracker is to provide a single framework that auto-detects the type of grid from multiple hydrodynamic model formats and identifies useful optional variables, such as bottom stress used in particle re-suspension. This enables users to focus on the outcomes they need from particle tracking, rather than the details of underlying hydrodynamic model.

Like many other particle trackers OceanTracker saves users' time by performing particle tracking "offline", based on the recorded output from a hydrodynamic model. In contrast, "online" particle tracking performs computations during the hydrodynamic model run. Hydrodynamic model run-times are typically much longer than those of particle tracking. Thus, any new variations in particle tracking requires re-running the slow hydrodynamic model. As a result, offline particle tracking facilitates faster exploration of variations in behaviours and the sensitivity of results to parameters, e.g. fall velocity. Examples of OceanTracker's applications to date are:

- Backtracking to infer likely locations of the parents of settled mussel larvae. Approximately 600 million particles were released over ten years and tracked for their 6-week lifetimes. (Atalah et al., 2022).
- Investigating phytoplankton retention mechanisms in an estuary with populations that grow through particle splitting. One billion particles were released, with up to 1 million active at any one time.(Steidle and Vennell, 2024).
- Inferring the area within which the eDNA of a species can be detected from water samples (Ane et al., in prep.).
- Estimating the risk of invasive species from ballast water discharged from ships transiting coastal shipping routes (Smeaton et al., in prep.).
- Determining pathways for the spread of diseases between aquaculture farms from connectivities between 500 farms based on 150 million particles (Knight et al., in prep.).

- Online ocean plastics public engagement tool, allows users to drop virtual plastic and see where it travels to. Returns 20 particle trajectories in less than 1 sec from an on-demand particle tracker server (Vennell et al., 2019).

This paper outlines the comprehensive list of design objectives in Sec. 2.1.2 and provides an overview of its features in Sec. 2.1.3, including some example outputs in Fig. 2.1. Sec. 2.1.4 details its structure, characterized as a "computational pipeline" composed of components within "roles" Sec. 2.1.4 and describes how to configure the computational pipeline in Sec. 2.1.4. Additionally, Sec. 2.1.4 outlines 'integrated models' which combine roles to achieve a higher level functionality, such as calculating Lagrangian coherent structures. Sec. 2.1.5 explores the features contributing to OceanTracker's speed and compares its performance to OpenDrift.

Design objectives

OceanTracker has been constructed to meet a number of design objectives. The design objectives in order of importance were:

Computational speed: Speed enables the user to release millions of particles.

Minimizing user time and effort: Minimizing the time and effort it takes to go from running the particle tracking to having the required analysis results, e.g. the heat-maps in Fig. 2.1.

Adaptability: Ability to easily modify or extend functionality.

Parameter-built computational pipeline : A single set of parameters or settings, is entirely responsible for enacting user options and building their computational pipeline (see Fig. 2.4). This enables coders and non-coders access to the same level of adaptability when using inbuilt components, exploit distributed compute and to develop particle tracking as an online service, Sec. 2.1.4.

The first two objectives can conflict. For example, consolidating all particle operations in the computational pipeline within a single kernel loop would be faster, i.e. performing all required computations for each particle one at a time. This approach increases efficiency, as the data required for each particle is likely to be in the faster chip memory cache if used more than once, and avoids the need to create, read or write arrays in main memory for intermediate results. However, it is much harder to adapt a single kernel loop when there are many operations with different variants. OceanTracker takes a middle ground, by breaking up the computational pipeline into a series of modular kernel operations on all particles as illustrated in Fig. 2.3. These operations are associated with different roles within the computational pipeline. This modular approach compromises speed, but significantly enhances adaptability, allowing for easier modification of individual operations to meet user needs.

2.1.3 Overview

At a high level particle tracking code, takes the Eulerian water velocity field from a hydrodynamic model, interpolates these velocities to provide Lagrangian velocities at particle locations, and then numerically integrates these to output particle trajectories. OceanTracker decomposes this process into a series of components that fulfill specific roles within the computational pipeline outlined in Fig. 2.2, Fig. 2.3 and Sec. 2.1.4. This section highlights some

	Specifications			Minutes per modelled month		
	CPU	RAM Gb	Freq. MHz	Read	Computation	Total
Laptop I	4	8	1.6-3.9	7	41	48
Laptop II	10	16	1.7-4.7	4	23	27
Desktop I	8	32	3.7-4.4	8	32	40
Desktop II	32	128	3.7-4.5	4	25	30
Work station	36	256	2.7-3.7	8	39	47

Table 2.1: OceanTracker run times for modeling 1 million particles over a period of 1 month. The runs utilised a single core, a time step of 15 minute and Runge-Kutta 4 time integration. The 3D SCHISM hydrodynamic model included 79k nodes and 140k triangles.

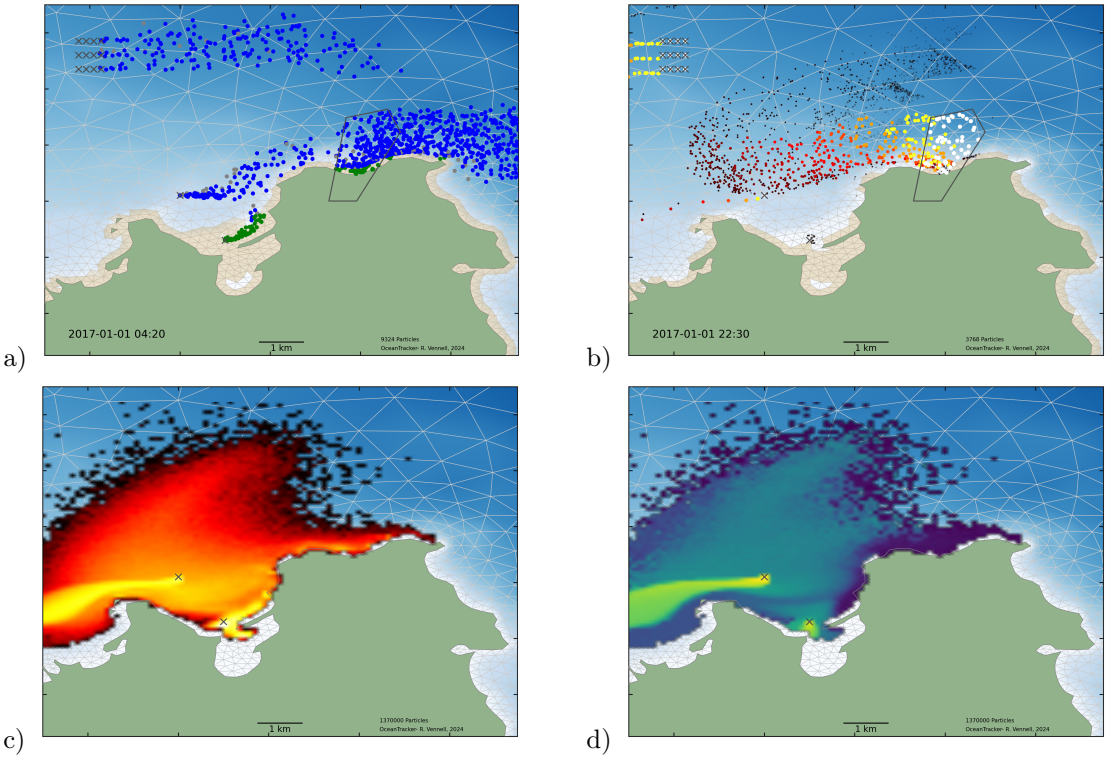

Figure 2.1: Examples of simultaneous point, polygon and grid particle release groups, Sec. 2.1.4. a) A snapshot of the particles: blue indicates particles are moving, grey signifies particles on the bottom that may later resuspend and green represends those stranded by the outgoing tide. Dry cells are shown in brown, with the blue shading indicating water depth. b) Particles sized and coloured according to a decaying particle property Sec. 2.1.4. c) Heat-map of log particle counts from a release of 1.3 million particles from a pair of point sources. d) Heat-map of decaying particle property on a logarithmic scale. The code to run this example is in Appendix 4.1.1.

of OceanTracker features that minimise user effort, its physics and an example use case is presented in Fig. 2.1.

Features reducing user effort

In addition to computational speed, OceanTracker incorporates an number of features that significantly reduce the time and effort required to obtain results from the analysis of particle trajectories. The most significant features are:

Release groups: This feature allows simultaneous release of multiple groups of particles, each with distinct locations and timing. This functionality enables users to obtain more comprehensive results from a single computational run, as shown in Fig. 2.1, Sec. 2.1.4 and Appendix 4.1.1. This eliminates the need for setting up and managing multiple runs to explore different release scenarios. Moreover, separating into release groups enables on-the-fly statistics to separately calculate statistics for each release group, i.e. such as individual heat-maps for each release site.

On-the-fly particle statistics: OceanTracker enables the addition of multiple statistics components to a computational run. This enables the calculation of diverse statistics from the same set of particle trajectories. For instance, it can generate different heat-maps for moving particles and those on the bottom, and calculate connectivities between areas, all within the same computational run.

Multiprocessing: OceanTracker leverages multiple computer cores allows users to run multiple scenarios in parallel. It simplifies multiprocessing by orchestrating all cases within a unified set of user parameters and organises the output in a consistent structure.

Coding productivity New functionality for tailored applications can be added to OceanTracker using the widely used Python language Numpy package. For complex computationally intensive operations Numba can be used (Lam et al., 2015b). A major advantage of Numba is that users do not need to learn new coding syntax, such as C, to speed for intensive operations. More on Numba in Sec. 2.1.5.

Physics

OceanTracker implements the core physical processes using components that users can replace with their own implementations. Users can also enhance particle physics by adding components to the velocity modifiers role (e.g. sinking velocities) or trajectory modifiers role (e.g. particle splitting or larval behaviours) as outlined in Sec. 2.1.4 and Sec. 2.1.4 The core physical processes include:

Dispersion role: A random walk mechanism simulates dispersion due to sub-hydrodynamic grid scale processes (Lynch et al., 2014). By default constant turbulent eddy viscosities are applied. If vertical 3D turbulent viscosity profiles are available in the hydrodynamic model files, these profiles are interpolated profile to calculate the vertical random walk instead, necessitating a vertical velocity correction (Ross and Sharples, 2004). Note that, the random walk is not applied as a step change in position, but as an equivalent additional velocity applied to each RK sub-step in the velocity modifiers loop (see Fig. 2.3 and Sec. 2.1.4).

Re-suspension role: Particles on the bottom may re-suspend if flows are strong enough. Whether and how far re-suspending particles jump above the sea bed depends on the friction velocity (equation 9.28 in (Lynch et al., 2014)). Thus, particles are more likely to re-suspend and jump higher, in stronger flows. The friction velocity is calculated from the near seabed velocity assuming a logarithmic velocity profile, or the bottom-stress field if it can be found in the hydrodynamic model output.

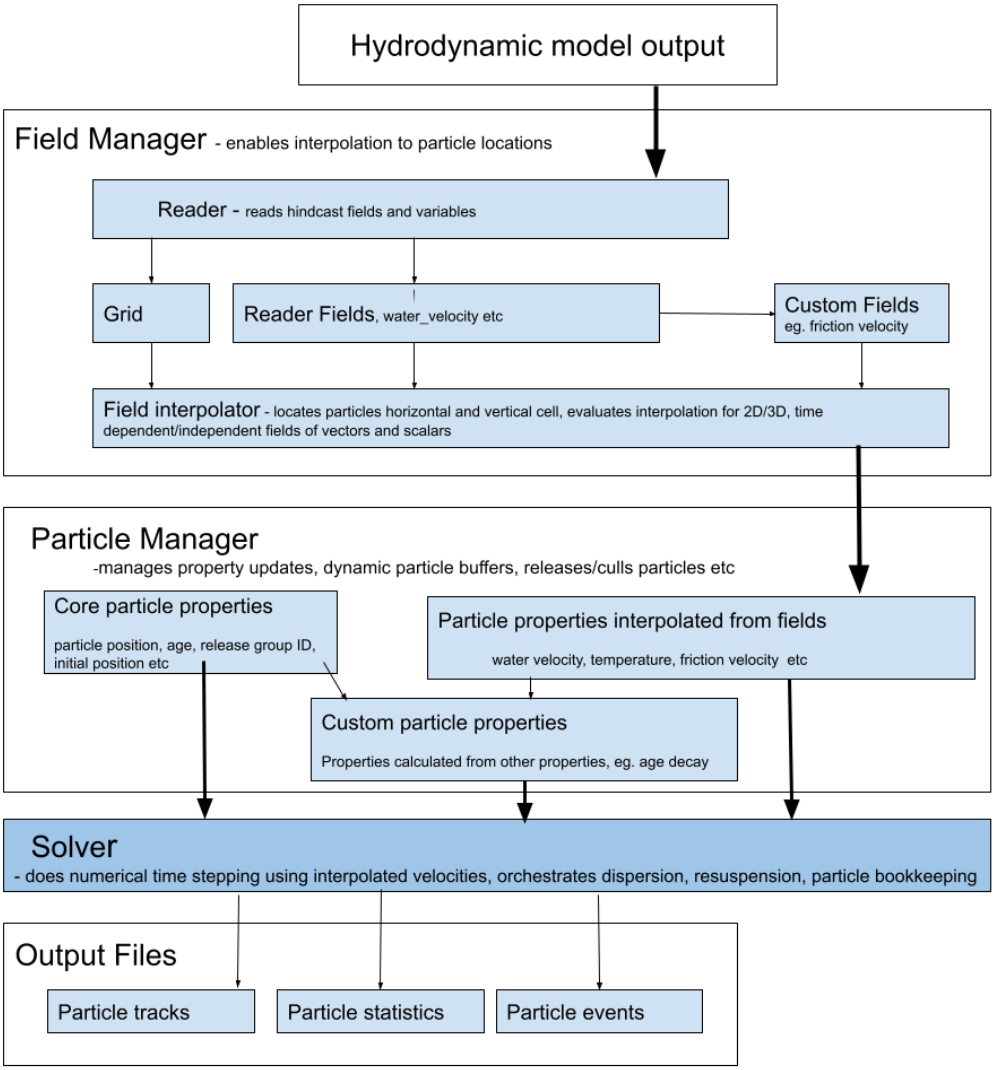

Figure 2.2: Outline of data flow through the two main data structures, fields and particle properties, from hindcast to output. These data structure roles are outlined in Sec. 2.1.4. Each have "managers" to orchestrate operations on the variants of each data structure, to deliver particle properties to the solver.

Tidal stranding role: Particles in dry hydrodynamic model cells remain stationary until the cell becomes wet again. Dry cells flags are set from data in the hydrodynamic model. If this data is not available, then a cell is dry if the total water depth at the cell's center is less than a user given minimum value.

Along with the above core user replaceable physics roles, OceanTracker has other features that affect particle movement. For example:

Nested grids: To enable particle tracking beyond the open boundaries of a single hydrodynamic grid, OceanTracker can nest multiple inner grids within a broader scale outer grid. Particles exiting the open open boundary of an inner grid are transferred to the outer grid, and particles on the outer grid which move inside an inner grid, are transferred to that grid. Each particle is aware of its current grid, allowing field values to be interpolated from the relevant grid. The inner and outer grids may consist of any combination of structured or unstructured grids.

Backtracking: OceanTracker supports reverse time simulations, which can be useful for identifying potential sources of particles arriving at a given location (Thygesen, 2011). Note that dispersion is not time-reversible, and this operates the same in the forward direction time, producing outputs, like heat-maps, that offer a probabilistic view of sources.

Example

Fig. 2.1 presents some basic examples of OceanTracker outputs from a 3D simulation. This example shows point, polygon and regular grid particle releases within the same computational run, add discussed in Sec. 2.1.4. The snapshot in Fig. 2.1a displays particles coloured according to their status, moving (blue), stranded by the tide (green) or on the bottom (grey).

Heat-maps can illustrate the decay and dispersion of a pollutant from its source. To construct heat-maps using particle tracking, sufficient particles must fall within each grid cell to ensure spatially smooth heat-maps. The efficiency of OceanTracker allows for the release of millions of particles, enabling the direct creation of heat-maps without the need for additional radial smoothing of particle counts. In Fig. 2.1c 1.3 million particles were sufficient to produce a detailed the heat-map. This heat-map was generated by counting particles into grid cells on the fly, thereby avoiding the need to record large volumes of particle trajectories. Fig. 2.1d illustrates a heat-map of the average value of a user-added exponentially decaying particle property.

2.1.4 OceanTracker structure

At a high level, Fig. 2.2 illustrates the data flow in OceanTracker from hydrodynamic model files to outputs, via the two main data structures. Fields store data from the hydrodynamic model, such as water velocity, salinity, wind stress, as well as derived fields calculated from other fields, such as friction velocity. Particle-proprieties hold data for each particle, which could include its current location, status or a value interpolated from a field. These data structures enable access to and operation on their data. At a higher level these data stuctures are collectively "managed" as outlined in Sec. 2.1.4.

The high-level flow of data is implemented by the computational pipeline (see Fig. 2.3). This system is constructed from components assigned to specific roles within the pipeline. From a user's perspective, the adaptability of OceanTracker comes from the ability to add components and their settings within each role of their specific configuration. Internally dividing these tasks into roles enhances adaptability, by enabling the computational pipeline

to automate the computations. This is achieved by updating components individually for certain roles, and by looping over components for others.

Computational pipeline

The computational pipeline splits the core computational loop into steps which implement a specific role within the pipeline (see Fig. 2.3). One or more components execute each role. These components are constructed as Python classes, which are dynamically added to the computational pipeline during setup. The computational pipeline proceeds sequentially by simply calling the "update" method of each class within a role. Some roles, such as dispersion and re-suspension, allow only one class to be added. Others allow multiple classes to be added to that role, which then are looped over, updating all before progressing to the next role in the computational pipeline. For example, multiple trajectory modifiers which can combine to give the required particle behaviour, such as initially floating then later settling on the bottom.

Configuring the computational pipeline

The computational pipeline can be fully configured using parameters from a text file or a Python dictionary, eliminating the need to code to run OceanTracker , e.g. Fig. 2.1b,c. However, coders may find it easier to create complex simulations using a 'helper' wrapper for OceanTracker . This allows coders to build their parameter dictionary using keyword arguments, bu using two provided methods "settings" and "add class" (see Fig. 2.1a). Users can also build their own Python parameter dictionary directly in code, which adheres to the same structure as the JSON format shown in Fig. 2.1c.

There are simple configuration settings, such as time step and more complex settings nested by role for each component. The configuration for each selected component typically includes the name of the class that the user is choosing for that role. This name is used to dynamically import the class into the computational pipeline at runtime. The main roles in the computational pipeline are outlined in Fig. 2.3, Sec. 2.1.4, Sec. 2.1.4 and Sec. 2.1.3.

Most component settings have default values defined within the class, while some require user specified values. Settings provided by the user are automatically checked for type and value range appropriateness. Children of a class inherit their parent's default settings and can redefine, remove or add new settings.

Computational steps automation

The updating of each component is automated within the time stepping of the computational pipeline, with updates grouped by role (see Fig. 2.3). The order in which the roles are updated reflects their temporal dependence on the data from other roles. For example, custom particle properties may be calculated from field particle properties and are thgerfore updated after the interpolated field properties. The Solver class implements the time stepping by managing the classes within the computational pipeline and the associated bookkeeping functions. By default, fourth order Runge-Kutta (RK) time integration is used, while first and second order RK are also available.

The first step involves looping over the release groups and releasing a single pulse for any scheduled release at the current time step. Next, the solver checks if field time buffers contain the required time steps: if not, the reader fills the buffers and any custom fields are calculated. After this, each particle's current horizontal and vertical cell is updated and used to interpolate the water velocity field to each particle's location from the cells' nodal values. In addition to the water velocity from the hydrodynamic model, the user may add additional

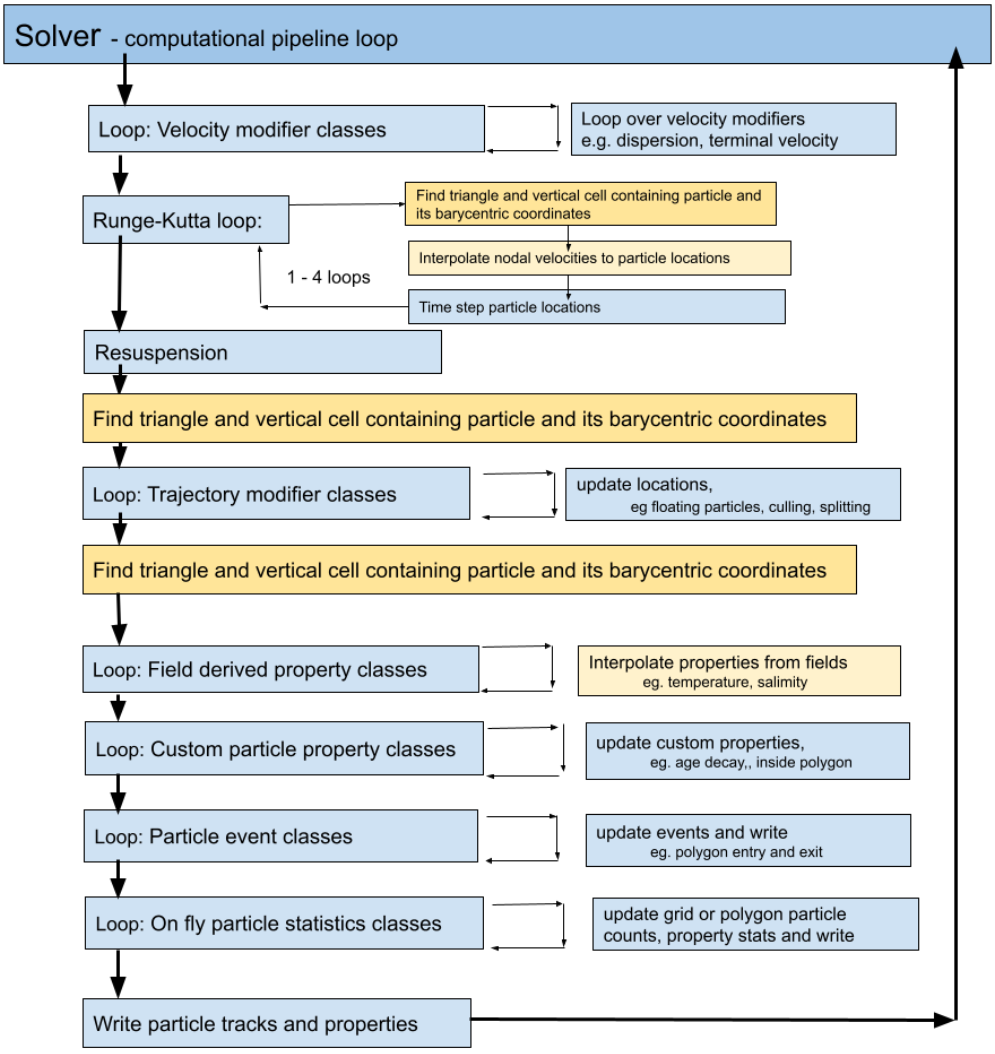

Figure 2.3: Components of the computational pipeline within the time stepping of the Solver role. These operation roles are outlined in Sec. 2.1.4. For large runs, the most computational expensive steps in order are typically, finding the cell containing each particle and evaluating the field interpolation. These steps are coloured yellow.

a) python

```python
from oceantracker.main import OceanTracker
# make instance of oceantracker
ot = OceanTracker()

# add  settings
ot.settings(output_file_base='minimal_example',
            root_output_dir='output',
            time_step= 120.)
# reader for hindcast files, format is auto detected
ot.add_class('reader',
             input_dir= '..\\demos\\demo_hindcast',
             file_mask=  'demoHindcastSchism*.nc')
# add  (x,y,z) locations where particles are released
# note: can add multiple release groups
ot.add_class('release_groups', name ='my_release_points',
             points= [[1595000., 5482600.,-1.],
                      [1599000., 5486200.,-2.]],
             release_interval= 3600, pulse_size= 10)
# start computation
ot.run()

```

b) yaml

```yaml
output_file_base: minimal_example
root_output_dir: output
time_step: 120.0
reader:
  input_dir: "..\\demos\\demo_hindcast"
  file_mask: "demoHindcastSchism*.nc"
release_groups:
  my_release_point:
  points: [[1595000,5482600],
           [1599000,5486200]]
  release_interval: 3600
  pulse_size: 10
```

c) json

```json
{
  "output_file_base": "minimal_example",
  "root_output_dir": "output",
  "time_step": 120.0,
  "reader": {
    "input_dir": "..\\demos\\demo_hindcast"
    ,
    "file_mask": "demoHindcastSchism*.nc"
    },
  "release_groups": {
    "my_release_point": {
      "points": [[1595000,5482600],
                 [1599000,5486200]],
      "release_interval": 3600,
      "pulse_size": 10}
  }
}
```

Figure 2.4: Minimal example of building a computational pipeline by a) Coding, using the "helper" wrapper to build a Python parameter dictionary, or as user supplied parameters within a text file following the b) YAML or c) JSON standard.

particle velocities, such as fall velocity. The total velocity due to all the "velocity modifiers" is then calculated, The next step is the time integration, where the particles are advected by the water velocity plus the total velocity modification.

Next, re-suspension and trajectory modifiers apply any additional movements to the particles. To calculate the properties of the moved particles, their current horizontal and vertical cells and Barycentric coordinates are updated. Then, all field-derived particle proprieties are looped over and updated by interpolation; the status of each particle is changed if it is in a dry cell. The subsequent steps involve updating any custom particle properties, calculating any particle statistics that have been added to the computational pipeline, and then writing out time series of particle trajectories and particle properties if requested.

Mechanisms enabling computational pipeline adaptability

The mechanisms that enable computational pipeline adaptability within OceanTracker are:

Dynamic importing: This feature imports each Python class component into the computational pipeline based on the name provided by the user in their configuration, described in Sec. 2.1.4. Users can add novel variants of any role simply by naming that class in their configuration, just as they would do for in-built classes.

Inheritance: Variants of a components are created by inheriting the base class for its role, or one of its children, and overwriting some of the methods to alter its computation. Commonly, this would involve overwriting the update method to meet specific needs. For example the polygon particle release class inherits most of its operations from its parent point release.

Data roles in the computational pipeline

OceanTracker's two main data structures are fields and particle properties, Fig. 2.2. This section outlines these data roles, while Sec. 2.1.4 describes their management.

Field role

The spatial fields stored within the hydrodynamic model's files are the foundation of offline particle tracking. These are stored and accessed using the "field" data structure (see Fig. 2.2). The water velocity field is a crucial spatial field for particle tracking, but there may be many other relevant fields, such as water depth , tide or wind-stress. These fields can be 2D or 3D, time-dependent or independent or scalar or vector. They also have an associated grid variables, including nodal locations, triangulation and cell adjacency.

Fields are read from files as detailed in Sec. 2.1.4. Additionally, custom fields can also be integrated into to the computational pipeline. These fields are derived on the fly by calculation from existing fields. For example, a friction velocity field can be computed from the 3D velocity field near the sea-bed to determine whether a particle can be re-suspended by the flow. Custom fields are calculated using their update method, which is used to automatically executed after the primary fields have been read from the hydrodynamic model files.

Particle property role

"Particle properties" store the values for each particle and enable high level operations on these values as shown in Fig. 2.2b. These properties have different types, depending of how they are updated each time step and may be scalars or vectors.

Field particle properties These sore field values at each particle location, such as water velocity. Field particle properties. They are updated by interpolating the field data structure with the same internal name.

Custom particle properties store values calculated from other particle properties. These are updated after the field types, via the class's update method. For example, the "inside-polygons" class uses the location particle property to determine which user given polygon contains each particle.

Core particle properties are not updated using their class update method, but are managed by the main code. Examples include particle location and book keeping particle properties, such as particleID and release groupID numbers.

Some examples of currently available custom particle properties are:

Age decay: models an exponentially decaying particle load, such as bacteria, based on the core "age" particle property

Inside polygon: records which of a given set of polygons, a particle is currently inside. This is used calculate polygon connectivity statistics, or to allow larvae to settle when over a reef.

Total water depth: represents the sum of tidal elevation and water depth. This property is useful for particles whose behaviour differs in different water depths, such as larvae that only settle in shallow water, even if a cell is not completely dry.

Manager roles in the computational pipeline

Instances of field and particle properties store, update, and manage access to individual fields or proprieties. Higher level operations on all the individual instances are orchestrated by "managers" which automate key processes. Similarly the reader role manages access to the files of the hydrodynamic model. The primary role of these managers is to deliver fields interpolated to particle locations, as required by the solver (see Fig. 2.2).

Fields group manager role

This orchestrates the setup, reading, updating and interpolation of fields, along with setting up the required grid variables, such as nodal locations, triangulation and the adjacency matrix. It also manages the process of finding each particles current horizontal and vertical cell and updates the status of dry cells. By default, the fields group manager automatically adds a particle property with the same internal name as the field to the computational pipeline, to be interpolated from that field at each time step.

Particle group manager role

This orchestrates the release of particles and the updating all three types of particle properties. It also manages the dynamic memory buffers which hold the individual particle property values, expanding them as needed when particle numbers grow and culling computationally dead particles that are no longer of interest. Additionally, if required, this manager handles the writing time series of particle trajectories and properties.

Reader role

The primary function of the reader to convert hydrodynamic model file variables into standardised internal formats. Initially, it reads file grid variables maps then to standard internal

variable names. It subsequently calculates other necessary grid variables, such as the triangle adjacency matrix.

Secondly it reads fields from hydro-files into buffers, determining their characteristics, such as being time-dependent ot independent, 2D or 3D and vector orscalar. For vector fields, several file variable names can be mapped to a single internal vector variable, allowing vector fields to be treated as a single variable within computations.

To support OceanTracker's current approach to interpolation is for the reader to convert all fields to values at the nodal values on triangles through interpolation, unless they are already nodal values. OceanTracker's modular approach allows development and substitution of a reader and interpolator for a hydrodynamic model's native grid, that do not require to this conversion. To facilitate automation, the reader stores all fields in 4D arrays with dimensions (corresponding to time, node, z-depth and vector components). Some of these array dimensions may be of size one, for instance water depth, a 2D time-independent scalar field, would have unitary dimensions for time, z-depth and vector components.

Currently SCHISM, FVCOM, DEFLT3D-FM and ROMS hydrodynamic model formats are supported (Zhang et al., 2016; Lai et al., 2010; Moore et al., 2011). For SCHISM and DEFLT3D-FM, any quad cells are divided into triangles. The interpolator supports the native grid interpolation of SCHISM's LSC vertical grid, which reduces the number of vertical layers in shallow water, to decrease the computational load. For the structured ROMS grid, fields are interpolated to its ψ grid, before being converted to triangular nodal values.

The reader loads fields into memory buffers as they are needed. For time-dependent variables it reads multiple field time steps into ring buffers if the time steps required by the RK computation are not already in the buffer. By default the ring buffers maintain 24 hindcast time steps for each field. To ensure files are loaded in the correct order, during setup OceanTracker sorts all files in a folder and its sub-folders into time order, based on their internal time variable. The reader also alerts users to any significant time gaps between files.

Operational roles in the computational pipeline

Computational operations access the fields and particle properties as outlined in Sec. 2.1.4. These operations are grouped within roles, as illustrated in Fig. 2.3 and described in this section, while operational roles associated with core physics are detailed in Sec. 2.1.3. Grouping components within each role enables automation within the computational pipeline. Internally components are referred to using standard or user-provided names.

Interpolator role

The interpolator serves as the link between the hydrodynamic model's fields and the corresponding particle properties. After determining each particle's current triangle, horizontal and vertical cell, the interpolator converts field data values to values at each particle's location, which are then stored as particle properties. In the horizontal, OceanTracker currently uses linear interpolation in unstructured triangular grids from nodal values, utilizing a particles' Barycentric coordinates within their current triangle. Linear interpolation is applied within vertical layers and between time steps, except for the water velocity within the seabed layer. Here, vertical interpolation is based on a logarithmic layer, ensuring that particles near the seabed experience more realistic horizontal velocities, which is crucial for newly re-suspended particles. OceanTracker automatically applies an appropriate interpolator to each type of field, depending on whether it is 2D or 3D, scalar or vector, time-dependent or independent.

Particle release groups role

A "particle release group" introduces new particles to the computational pipeline. Each release group generates new particles at specified locations, which are released at designated times, in defined pulses sizes. Multiple release groups can be added, each with its specific locations and release schedule. The current release types inculde:

Point release spawns particle from a set of specified locations and depths. A optional radius setting allows particle releases randomly within a circular area around each point.

Polygon release: Particles are spawned at random locations within a user-defined given 2D polygon.

Grid release: spawns particles from points of a regular grid.

Particles will not be released in any locations outside the domain (see Fig. 2.1a). Also, by default, particles are not released within cells currently dry due to the tide. For all types is possible to restrict releases to be randomly distributed within a given vertical layer, or to locations with water depth in a given range, e.g. for seaweed propagules whose parents only live in the shallow areas within a release polygon.

Velocity modifiers role

Additional bio-physical processes can modify the water velocity experienced by each particle. These are incorporated into the computational pipeline as "Velocity modifiers", where the effects of each are added to the water velocity for use in the time integration (see Fig. 2.3). An example of an in-built modifier is:

Terminal velocity: The modifier adds the the terminal sinking or buoyant velocity to the ambient water velocity, either as a uniform value or a particle specific value drawn from a normal distribution.

Trajectory modifiers role

"Trajectory modifiers" are bio-physical processes that alter the movement patterns at each time step. Examples of in-built modifiers include:

Settlement: Allows larvae to settle on reefs defined by polygons. The trajectory is modified by changing its status to "stationary".

Floating: Sets each particle's vertical position to that of the free-surface height at its current location.

Culling: Flags particles that are no longer of interest as dead, allowing then to be removed from subsequent computations.

Splitting: This splits particles in two to simulate reproduction, at a set rate or probability. This can rapidly generate very large numbers of particles which need to be contained by a culling mechanism (Steidle and Vennell, 2024).

On-the-fly particle statistics roles

Scaling up particle numbers to millions can create large volumes of particle track data. The on-the-fly counting statistics approach produces a data output volume independent of the number of particles released. Currently there are four main types of spatial particle statistics:

Gridded: Used to produce heat-maps. These count particles inside cells of a regular grid at a user-specified time interval.

Polygon: Calculates the physical connectivity matrix between each release group and areas bounded by given polygons.

Both types record particle counts from each release group separately and have two variants.

Time series: Counts particles at specified time intervals, providing time series of heats-maps or connectivities.

Age bins series: Counts particles within each spatial bin into age bins, to produce age-based heat-maps or connectivities. This has applications in tracking the age distribution of particles in specific areas.

It is also possible to limit which particles are counted, for example, only counting particles in a given vertical "z" range or only those lying on the bottom. Users can add multiple on-the-fly statistics components, all calculated from the same particles during the computational run, such as adding a particle statistic counting particles in different depth ranges. In addition to particle statistics, average values of particle properties within the spatial counting bins can also be calculated on-the-fly, such as water temperature or distance travelled.

An additional in-built statistic is **residence time:**, which calculates time series of the average time that particles released within a polygon reside within that polygon (Lucas and Deleersnijder, 2020).

Integrated models

Many use cases require users to combine multiple roles to create higher level functionality. OceanTracker supports this aggregation of roles into a single class for reuse. These integrated models only require the parameters essential for executing their higher level function; the model manages the intricacies of assigning classes to appropriate roles to complete the overall function. Current integrated models include:

On-the-fly sea-bed flux: Released pollutants, such as waste from fish aquaculture farms, may sink to the bottom while being advected by the current flows. This model generates flux heat-maps by calculating the depostional flux of particles into cells of a regular grid around each user-specified release location. It performs these calculations this on-the-fly, by counting particles that have reached the seabed since the last flux estimation. It it does not allow re-suspension and marks counted particles as dead.

On-the-fly Lagrangian Coherent Structures: These structures identify regions of convergence or divergence within a fluid flow over time. In OceanTracker they are implemented as time series of Finite-Time Lyapunov Exponents (FTLE) (Haller, 2015; Harrison and Glatzmaier, 2012). FTLE calculation use the largest Eigenvalue of the strain tensor after specified lag times. This process involves releasing particles on a regular grid and calculating the distances between adjacent released particles. The user only needs to designate one or more grid locations and the required time lags. The integrated model sets up new regular grid releases at regular time intervals and calculates the FTLE on-the-fly for each lag, eliminating the need to record and post process large volumes of particle trajectories.

2.1.5 Computational speed

The primary features contributing to computational speed of OceanTracker are:

Finding cell: In unstructured grids, significant computational time is spent determining the horizontal and vertical cells containing a particle. OceanTracker leverages the particles history to improve the speed of its cell search. Short triangle and vertical walk algorithms improved the search speed by an order of magnitude as outlined in (Vennell et al., 2021).

Calculate once, use many: To avoid repetition in performing key computational tasks, a particle's current triangle, barycentric coordinates, vertical cell and fraction of the vertical cell are recorded at each time step. These values then used repeatedly to interpolate multiple

fields to the particle's location. Adopting this, 'calculate once, use many times' methodology significantly improves the efficiency of interpolations. (Vennell et al., 2021).

Dynamic Particle Buffer: Particle proprieties are stored in memory buffers, which expanded as needed to accommodate newly released particles. System performance and and memory utilisation can be optimised by periodically culling dead particles. For instance, setting a maximum particle age for a release group, beyond which they are no longer relevant, interest, will remove theses older particles from computations. When more than 20% are dead, particle memory buffers are compacted by removing dead particles.

Uniform sigma-grid: For 3D SCHSIM and FVCOM, models the search for the vertical cell is the most time consuming step as their fractional layer thicknesses vary spatially. Thus, the vertical search for each particle's cell is done within different layer thicknesses. Optionally for these models, the vertical cell search can be made 5 times faster by vertically interpolating to spatially uniform sigma-layer fractional thicknesses. With uniform fractional thicknesses, finding the vertical cell is significantly quicker using rounding within a pre-calculated layer map, followed by a correction step. The time spent re-interpolating to this near-native vertical grid, is minimal compared to the time saved by the faster vertical cell search. DEFT3D-FM and ROMS employ uniform S-grids, thus can directly can exploit the faster approach to vertical cell search at no additional cost.

Numba: Particle tracking requires complex operations with nested loops making per-particle decisions. These would be are computationally slow in Python. For example, the triangle walk to find each particle's horizontal cell requires calculating its barycentric coordinates, while being aware of any adjacent dry cells and lateral boundaries. To make complex looping 100s of times faster OceanTracker uses the Python extension Numba (Lam et al., 2015b). Numba understands a large subset of Python and NumPy code, only requiring a decorator to speed code. Numba can outperform NP by eliminating the need to create temporary array memory for intermediate results. Thus, Numba's computational speed is similar to those of C or Cython. Numba complies functions when first called and the complied code is reused on subsequent calls. The compilation of many Numba functions adds 20-30 seconds to OceanTracker's start up processes. Optional caching the complied Numba code to disk between runs can prevent this delay.

Parallelization: Optionally OceanTracker can employ an embarrassingly parallel approach to execute cases simultaneously, as described in (Vennell et al., 2021). This is achieved by providing shared parameters that apply to all cases, along with a list of parameters specific to each case. For instance, while all cases share the same on-the-fly-statistics, but each parallel case might release particles at different locations.

Speed comparisons

The following section compares the computational performance of OceanTracker with its closest alternative, OpenDrift (Dagestad et al., 2018). A similar comparison hass been reported in (Vennell et al., 2021). Since that publication the code base has undergone a significant overhaul. Previously relying on NumPy and SciPy for critical computational steps, it now uses Numba. This transition has facilitated the implementation of far more particle-specific decisions processes that enhances the realism of their movement, as outlined in Sec. 2.1.3.

The performance comparisons uses two 3D hydro-dynamic models. The first is a high resolution unstructured mesh estuarine model described in (Steidle and Vennell, 2024) and built using SCHISM (Zhang et al., 2016). This model features 32,000 horizontal nodes and employs terrain-following coordinates for the vertical grid, with up to 20 levels. Its spatial resolution varies from 5 m and 1400 m. The second model is a regular grid ROMS model

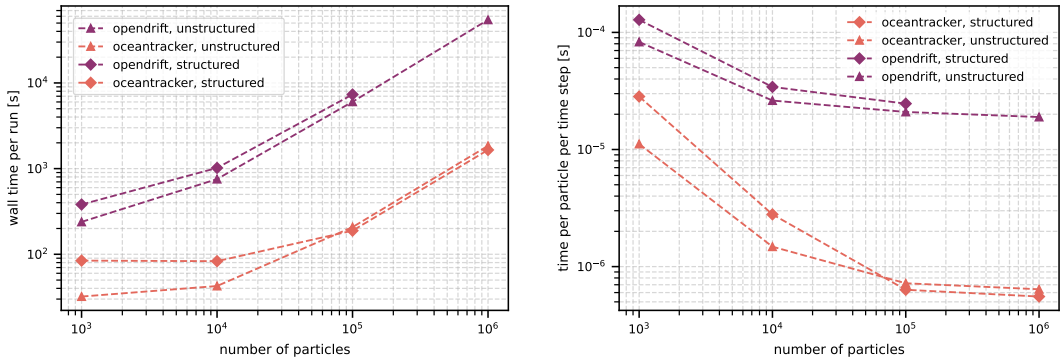

(a) (b)

Figure 2.5: Comparison of the computational speed of OceanTracker and OpenDrift for structured (ROMS) and unstructured (SCHISM) grids. a) Compares the total run time measured as wall time. b) shows the normalized computational time per particle per RK4 time step.

presented in (López et al., 2020), consisting of about 250,000 nodes and 40 vertical levels with a uniform horizontal resolution of 7 km. Both models had a temporal resolution of 1 hours.

The computational experiments were performed on the desktop computer I of table Table 2.1, which is equipped with an Intel(R) Core(TM) i5-10500 CPU @ 3.10GHz and 16 GB RAM. The computations covered 10 model days using 5 minute time steps, resulting in a total of 2880 time steps. Particles were released at 30 locations, with total particle numbers varying from 1000 to one million particles per model run. All computations were done on a single core.

Figure 2.5a displays the total run time across OceanTracker and OpenDrift on both structured and unstructured grids. Figure 2.5b illustrates the scaling of both models in terms of time per particle per RK4 time step. Which indicates that OceanTracker can process nearly a million particles per second on a single desktop core.

Model setup times are the main contributor to OceanTracker's run time for particle counts up to 10000 particles. For these small numbers, OpenDrift's minimum run time was approximately 2 minutes, while OceanTracker's completed these runs in 30 seconds. For particle counts exceeding 10,000 setup times become negligible for both models. In 1 million particle simulations OceanTracker is up to 35 times faster than OpenDrift, resulting in total run times of 15 hours for OpenDrift and half an hour for OceanTracker .

OceanTracker treats structured grids as unstructured grids by triangulating them, whereas OpenDrift uses a native reader for the structured ROMS grids. Surprisingly, the native ROMs reader of OpenDrift does significantly enhance its performance with unstructured grids. Also, OceanTracker does not experience a significant speed penalty for treating structured grids as unstructured.

Multi-processing scaling.

Fig. 2.6 shows that for a small grid, speed scales almost linearly with the number of processors, with 25 processors yielding nearly 25 times the speed. For a large hindcast, the time required to access field data from disk and main memory results in sub-linear scaling, as illustrated in Fig. 2.6b. This data access bottleneck, suggested that restructuring the code to allow processors to share the data would improve how speed scales with the number of processors.

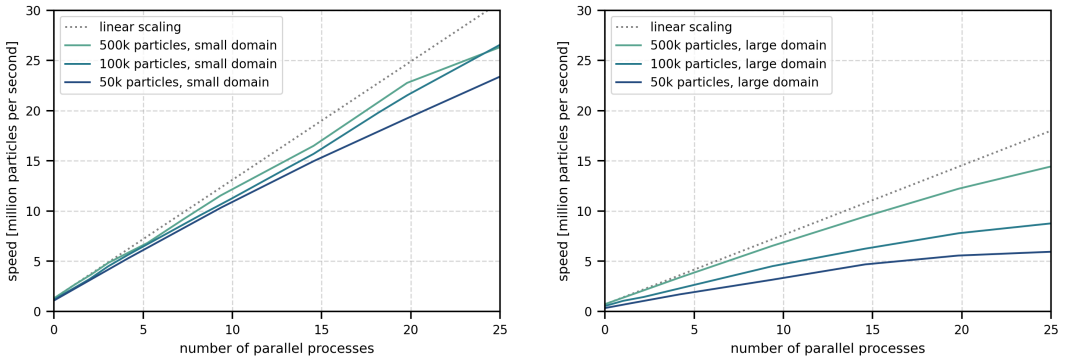

(a) (b)

Figure 2.6: Scaling of computation speed of cases run in parallel mode. Speed is the total number of particles across all processors simulated per second of total run time. Colors show results for 50,000 to 500,000 particles released in single pulse on each processor. As reference, dashed line shows linear scaling of a single 500k pulse. a) Small demo grid, 12 nodes. b) Large grid Cook Strait NZ, 180k nodes (Vennell et al., 2021).

2.1.6 Discussion

(Vennell et al., 2021) found OceanTracker to be significantly faster than OpenDrift for unstructured grids. Fig. 2.5 demonstrated there is a similar speed advantage for OceanTracker over OpenDrift on structured grids. This is surprising, as typically cell finding in structured grids is much faster, as it can be done by simple rounding of coordinates. This suggests that the speed difference is not due to differences in their cell finding algorithm, but to some other aspects of their approaches.

For unstructured grids, the original OceanTracker was over two orders of magnitude faster than OpenDrift (Vennell et al., 2021). The latest version of OceanTracker is an order of magnitude slower than its predecessor. However, the latest version has much improved physics Sec. 2.1.3. This enhancement has required in more costly computations of particle by particle decisions regarding their movement. These decisions result in slower branching code, but yield more realistic physics.

OceanTracker's implementation is a compromise between speed and adaptability, which imposes a limitations. One is illustrated in Fig. 2.3, where core particle properties, such as a water velocity, location, current horizontal and vertical cell are updated at every RK sub-step. However, velocity and trajectory modifiers are updated only once per full RK step. This is a compromise between speed, adaptability and numerical accuracy of trajectories. This approach assumes that modifiers vary slowly enough in space and time, that they can be treated as constant within the full RK time step. This assumption limits the acceptable time step size, requiring users need to choose a small enough computational time step that these modifiers can be treated as constant.

A recommended test for particle trackers is a circular flow of known period (Van Sebille et al., 2018). A 2D synthetic eddy test was performed, with a 1 ms^{-1} peak flow at a 10 km radius and 12 hour period. For 15 minute RK4 time steps the deviation of particles released 10 km from the center was less than 0.3 m from their initial radius after 10 days.

Future improvements to enhance OceanTracker's speed. might include greater use of Single Instruction Multiple Data instructions on conventional CPUs (SMID). Additional optimisation should be possible by adapting expensive computational kernels to take advantage of GPUs. Table 2.1 indicates around 20% of run time is spent in reading the hindcast. An asynchronous

reader sharing it memory with parallel particle computational processes could minimise this impediment.

2.1.7 Summary

OceanTracker provides a comprehensive ocean particle tracking framework compatible with both structured and unstructured grids. Its speed allows users to scale to larger numbers of particles on modest computer hardware within acceptable run times. This capability facilitates enhanced particle statistics and broader exploration of variations in particle behaviours. Integrating the calculation of particle statistics directly within computational runs significantly reduces the time required to derive needed statistics. In addition, on-the-fly-statistics produce more manageable data volumes, as their size does not depend on the number of particles released. The ability to add multiple release groups and statistics also reduces user efforts, by enabling multiple outcomes within the same computational run. Adaptability is enabled by a modular approach to roles within the computational pipeline.

2.2 Study II:

Potential effects of coagulation processes on phytoplankton mortality in the Elbe estuary from a Lagrangian point of view

Abstract

Within the Elbe estuary, a sudden change in depth occurs when the river water reaches the shipping channel in the Port of Hamburg. This change in depth correlates with a sharp decline in phytoplankton concentrations. This decline affects the estuarine food web and shifts the ecosystem from autotrophic to heterotrophic during the summer months. Previous studies have hypothesized that this collapse is primarily driven by zooplankton grazing. We question this narrative and investigate the effect of phytoplankton aggregation with inorganic suspended matter and its impact on light limitation. In this study, we present a novel individual-based Lagrangian model to investigate the influence of aggregation on phytoplankton mortality. By incorporating data from the hydrodynamic model SCHISM and the sediment transport model SediMorph, we simulate the movement and aggregation of phytoplankton in the estuary. Our results show that aggregation with inorganic particles significantly increases sinking rates, leading to increased light limitation-induced mortality, suggesting that aggregation processes may play an important role in explaining the collapse of phytoplankton concentration.

2.2.1 Introduction

On the one hand, estuaries are typcially highly productive ecosystems and contribute disproportionately to the global carbon cycle, in addition to their role as a source of nutrients and breeding or hatching grounds for marine ecosystems (Cloern et al., 2014; Arevalo et al., 2023). On the other hand, they are heavily influenced by anthropogenic stressors such as diking, dredging and fishing, and are of enormous importance for anthropogenic use (Jennerjahn and Mitchell, 2013; Brown et al., 2022; Wilson, 2002). Modern ecosystem management must balance the long-term sustainability of the ecosystem and climate with the economic interests of stakeholders.

The Elbe estuary is a particularly challenging example. Unlike other major European ports, the Port of Hamburg is located well inland, approximatelly 100 km from the coast. In order to provide access to the port for the largest class of container ships, the main channel experiences a sudden jump in bathymetry from about 5 m at the edge of the city to about 20 m in the harbour and downstream (see Fig. 2.7). This bathymetric jump is thought to be the main cause of the phytoplankton collapse (Pein et al., 2021; Schöl et al., 2014; Holzwarth et al., 2019).

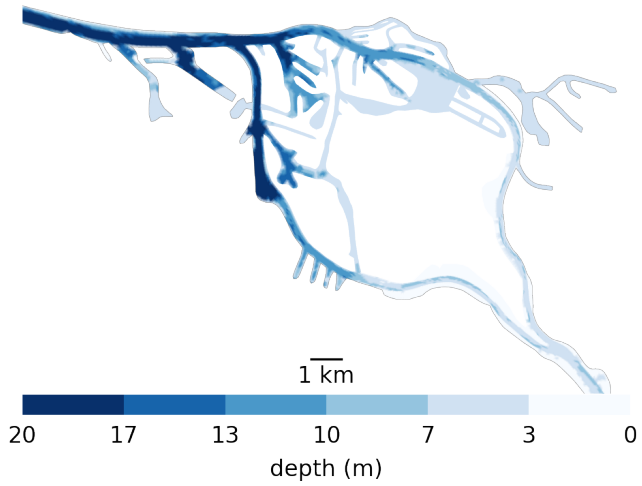

Figure 2.7: Bathymetry used in the Elbe model around Hamburg. Note the bathymetric jumps from 5 m upstream (the right-hand side) to 10 m for a short step in the upper port area to 20 m in the lower port area all the way to the North Sea. Also note that there is only one channel to enter the harbor section of the estuary, which is 20 m deep from shore to shore. So anything that passes through has to travel through deep water.

The Elbe estuary is located in northern Germany and flows into the North Sea. Like most alluvial estuaries, it is relatively shallow near the sea, with an average depth of only a few metres in most parts. Like other European estuaries, it has been subject to strong anthropogenic pressures over the last century. In particular, dykes for land reclamation and flood protection have confined the Elbe to a narrow channel, and dredging to improve access to the port of Hamburg. Since 1900, the navigational channel has been dredged nine times from a depth of 7 m, the most recent of which will deepen it to 18 m in 2020. Ongoing dredging is also carried out to maintain the depth of the navigational channel. The increase in depth and the ongoing dredging are suspected to be the drivers for the increase in measured turbidity (Weilbeer et al., 2021; Kappenberg and Grabemann, 2001). While important aspects of the biochemical dynamics along the channel have been studied, little is known about their

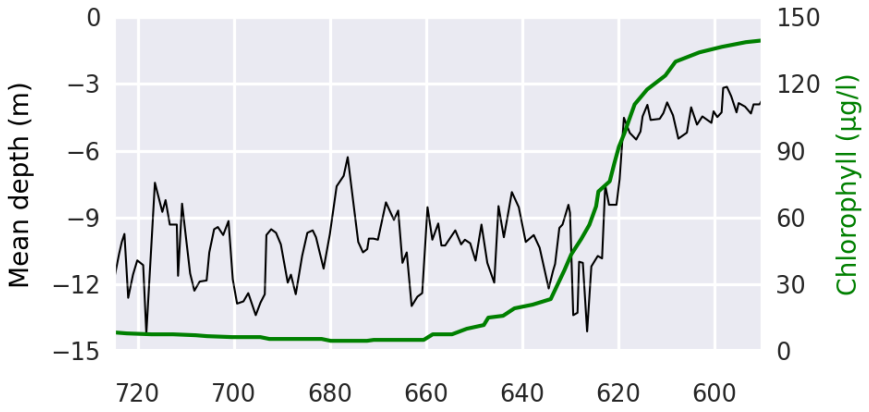

Figure 2.8: Chlorophyll concentrations as a proxy for phytoplankton biomass (green) and mean depth along a downstream transect averaged from shore-to-shore (black), showing the phytoplankton collapse and correlation with the bathymetric jump. Note, that the x-axis is inverted to keep consistancy with the map based plots.

vertical and cross-channel or shore-to-shore dynamics (Goosen et al., 1999; Dähnke et al., 2008; Sanders et al., 2018).

Like most ecosystems, estuarine ecosystem dynamics are strongly controlled by primary producers, particularly phytoplankton, which form the basis of the estuarine food web (Chen et al., 2023). Apart from benthic biofilm-forming phytoplankton or microphytopbenthos (Cheah and Chan, 2022), the vast majority of phytoplankton organisms drift passively in currents.

Phytoplankton concentration drops suddenly in the harbour area of the estuary (see Fig. 2.8). The correlation with depth suggests that the collapse may be caused directly or indirectly by the bathymetric jump (Schroeder, 1997). Measurements of low oxygen concentrations (<3mg/l) and high ammonium ($15 mmol m^{-3}$) concentrations at the bottom and high disolved inorganic nitrogen downstream of the bathymetric jump suggest a high remineralisation rate of organic matter (Schroeder, 1997; Holzwarth and Wirtz, 2018; Sanders et al., 2018; Spieckermann et al., 2022). This indicates that upstream phytoplankton is not being diluted or vertically dispersed in a way that allows it to elude the monitoring stations, but is actually dying. The collapse of the phytoplankton community also turns the estuary from a net autotrophic to a net heterotrophic system during the summer months (Schöl et al., 2014). Although this effect is well observed, the mechanisms behind this collapse are not well understood.

The collapse of the phytoplankton community in the Elbe estuary has been consistently observed in chlorophyll concentrations since the 1980s (Schöl et al., 2014). Looking at this trend over time we see that this effect has increased over recent years and shows to be correlated with the increase in turbidity which has more then tripled since 2010 (Weilbeer et al., 2021) (see Fig. 2.9).

Most studies suggest that the phytoplankton collapse in the Elbe is due to grazing or light limitation. The *grazing hypothesis* assumes that most of the phytoplankton is consumed by zooplankton. A common explanation (Schöl et al., 2014; Kopmann and für Wasserbau, 2014; Pein et al., 2019) is that marine zooplankton are pushed into the estuary with the tides up to the bathymetric jump. Upstream of the bathymetric jump, the flow velocity is much higher, making it difficult for them to migrate further upstream. This could explain the sudden drop

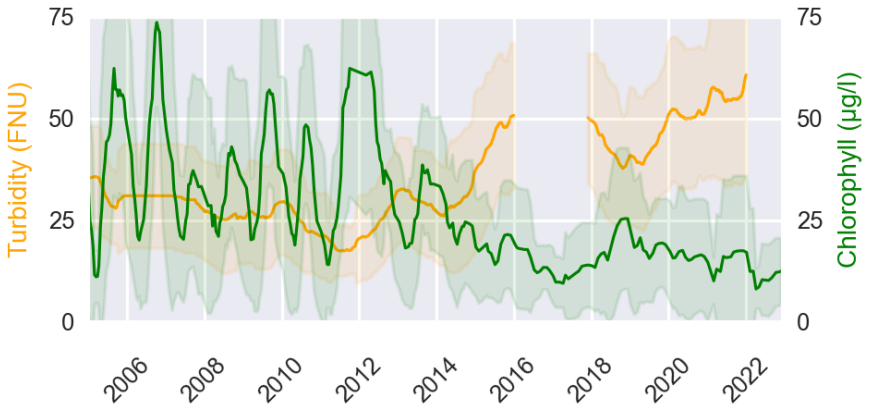

Figure 2.9: Chlorophyll concentraions as a proxy for phytoplankton biomass and turbidity. Measured from 2005 until 2023 at the station "Seemannshöft (Strom-km 628,9)" based on data open data available at FGG-Elbe https://www.fgg-elbe.de/elbe-datenportal.html (last access: 3 March 2024).

in phytoplankton concentration in this area. Although marine zooplankton species have been observed in this area, (Steidle and Vennell, 2024) showed that retention in this area without a sophisticated mechanism is difficult for planktonic organisms. Hence, an accumulations of marine zooplankton to large enough concentrations that could explain this drop in chlorophyll concentrations might not be possible. This suggest that the grazing hypothesis might instead be dependant on upstream freshwater zooplankton that could still easily survive in the low salinity port area. Alternatively, the grazing pressure could be in part due to benthic grazers. With much lower flow velocities close to the bed and a potential ability to hold on or even burry themselves in the sediments they would have a much easier time to persist in that area. Informal reports of there existance have been made but no systematic study has been performed to date to try and quantize their abundance.

The last zooplankton survey that could be used to examine the effect of zooplankton grazing has been performed in 1992 (Bernat et al., 1994) with a small unpublished survey mentioned in (Schöl et al., 2014). At that time the bathymetry was significantly different with a narrower navigational channel and a target depth of 13m instead of the current 18m (Hein and Thomsen, 2023). Additionally the upstream biochemistry has changed significantly since the collapse of the German Democratic Republic (GDR) with a drastic increase in water quality and a corresponding increase in in upstream chlorophyll concentrations (Adams et al., 1996; Matthies et al., 2006). This effectively leaves us in the dark about the current impact of grazing on the chlorophyll concentrations.

The *light limitation* hypothesis is based on the sudden increase in turbidity downstream of the bathymetric jump and the sharp decrease in mean downstream velocity and corresponding increase in residence time. This increase in turbidity in turn increased the aphotic to photic volume ratio, effectively reducing light availability for phytoplankton. Note that the turbidity in the navigational channel is so high that water at a depth of bewlow two meters is aphotic (below 1% of surface light). However, a 1D-modelling study by (Schroeder, 1997), and the light limitation induced mortility rates measured by (Walter et al., 2017) suggest that light limitation alone would be too slow to explain the sudden drop in phytoplankton concentrations around the bathymetric jump. Instead, it could be explained with a combination of light limitation, grazing, and the sharp decrease in downstream velocity. While light limi-

tation restricts most of the phytoplankton growth, the decrease of the downstream velocity drastically increases residence times around the bathymetric jump. Combining this with an grazing pressure from upstream zooplankton could cause the sudden drop of the phytoplankton community. Typically chlorophyll concentrations are presented relative to the position along the channel obscuring the shift in residence times between these to regions which might in part explain the perceived suddenes of this effect. Another process considered in some models is referred to as *sedimentation* (Hagy et al., 2005; Iversonl et al., 2000). This is based on the assumption that individuals in the phytoplankton community have, on average, negative buoyancy. Therefore, they slowly sink, where some of them are assumed to be buried in the sediment. This process is also implemented in two Elbe models presented in (Schöl et al., 2014; Pein et al., 2021). However, this process lacks calibration and validation data in both models and with their choice of sinking losses are considered negligible compared to grazing losses.

We suggest another explanation that has not yet been explored. Phytoplankton are typically thought to be sticky due to their excreted polysaccharides or transparent exopolymer particles (TEP) (Passow et al., 1994; Logan et al., 1995). If the suspended inorganic matter causing the high turbidity were to aggregate with the upstream phytoplankton, it would increase their sinking velocity. An increase in sinking velocity would shift their vertical distribution to deeper and henceforth darker waters. This in turn would increase light limitation effects and amplify the losses due to light limitation described above. A deeper average in the vertical column also reduce the downstream velocity as velocities towards the bottom are much lower and may even flow upstream (Pein et al., 2021) further skewing the speed of the collapse after the batymetric jump when measured relative to the along channel position rather then residence time. The phytoplankton aggregates would also be more likely to settle to the bottom, further increasing their residence time, while creating an additional loss term due to potential benthic grazing. We therefore suspect that this *turbidity induced sinking* may be an important factor in the recent increase in the collapse of the phytoplankton community in the Elbe estuary.

Similar *aggregation and settling* processes, sometimes also referred to as flocculation and percipitation, have already demonstrated in lab studies (Deng et al., 2019) and observed in the North sea on the border between Wadden Sea and North Sea (Schartau et al., 2019; Neumann et al., 2019) The North Sea typically shows high organic aggregates concentrations while the Wadden Sea aggregates shows to be high in inorganic content. At their boundary hisometimes also referred to as flocculation and percipitation, gh precipitation can be observed, which is thought to be due to the aggregation of organic and inorganic particulates, which increases their sinking rate.

Particle aggregation in marine environments is a complex topic with many open questions. It is best researched in the context of open oceans where marine snow is a major pathway in the global carbon cycle and part of global climate forecasting models (Burd and Jackson, 2009; Jackson and Burd, 2015). First advances have been made studying phytoplankton coagulation in coastal environments (Chen and Skoog, 2017; Horemans et al., 2021) while most studies focus on inorganic sediments compared to the organic focus of open ocean models (Weilbeer et al., 2021; Cox et al., 2019). Aggregates in different environments differ drastically in their size distribution and composistion which in turns strongly effects their characteristics like shape, density, stickiness, and settling velocities making it hard to genererallize aggregation processes (Kriest, 2002; Cael et al., 2021; Laurenceau-Cornec et al., 2020).

The most common modelling approaches are from an Eulerian perspective where aggregates are modeled as concentration field for a set of aggregate size classes. Changes between these size classes are estimated using so called coagulation kernels (Stemmann et al., 2004; Burd,

2013). This in turn allows for the estimation of a particle size distribution and vertical fluxes. These Eularian aggegation models have the same advantages and disadvantages as other Eularian models - most notably that trajectories or life histories of individual particles and individual based processes are not represented.

Recently, several studies have studied aggregation processes from a (semi-)Lagration perspective (Jokulsdottir and Archer, 2016). So far, no study has examined the aggregation processes in coastal or estuarine environments from a Lagrangian perspective. Until the development of the OceanTracker model (Vennell et al., 2021) this was computationally expensive and difficult to implement. While there has not been a Lagrangian model examining aggregation in the Elbe estuary there have been severel Eulerian models.

All current Elbe estuary models represtend phytoplankton mortality as a combination of a non-linear grazing loss function and a linear "natural mortality" or respiration loss function. Light limitation mortality is indirectly represtented as a limitation function in the growth rate. Aggregation processes are note represented in any of the existing models. Furthermore, while several models include Zooplankton grazing (Pein et al., 2021; Schöl et al., 2014; Holzwarth et al., 2019) they also use zooplankton grazing a tuning parameter such that the modeled concentrations fit the observed trends. Hence, a inference on the grazing induced mortality is not possible by these models, even though it is claimed in several publication (Schöl et al., 2014; Kopmann and für Wasserbau, 2014; Pein et al., 2019).

We will present a novel model study that attempts to draw attention to this issue. With this model we will investigate the effect phytoplankton aggregation processes from a Lagrangian perspective to examine the impact of "turbidity induced sinking" and the resulting light limitation induced mortality on the phytoplankton population. Although we have the same limitation of validation data as the previous studies, we try to provide first estimates of the relative importance of these processes that can serve as a basis for future research.

2.2.2 Methods

Model description

We have further developed the individual-based Lagrangian model OceanTracker (Vennell et al., 2021) and applied it to the Elbe estuary, similar to (Steidle and Vennell, 2024). Particle tracking on unstructured grids was relatively computationally expensive until recently, when (Vennell et al., 2021) improved the performance by two orders of magnitude to the current state of the art. Looking at the problem from a Lagrangian perspective offers several advantages. First, it allows us to reuse computationally expensive hydrodynamic models to model tracer-like objects. This is overall much faster by several orders of magnitude than recalculating the advection-diffusion equation for tracers in an Eulerian model. Second, because we simulate particles individually, we are able to observe their tracks. This makes the interpretation of our results not only intuitive, but also allows us to include individual-based properties and processes that cannot be represented, or only indirectly, in Eulerian models.

We use the hydrodynamic data from the latest SCHISM model of the Elbe (Pein et al., 2021). This model uses a three-dimensional unstructured grid to represent the entire Elbe estuary from the weir at Geesthacht to the North Sea, including several side channels and the port area (see Fig. 2.10). The model provides us with a node-based mesh containing a range of information such as water velocity, salinity, water level and dispersion. The year represented in this dataset is 2012 with a temporal resolution of 1 hour and a dynamically varying spatial resolution with node spacing ranging from 5 to 1400 m with a median spacing of about 75 m.

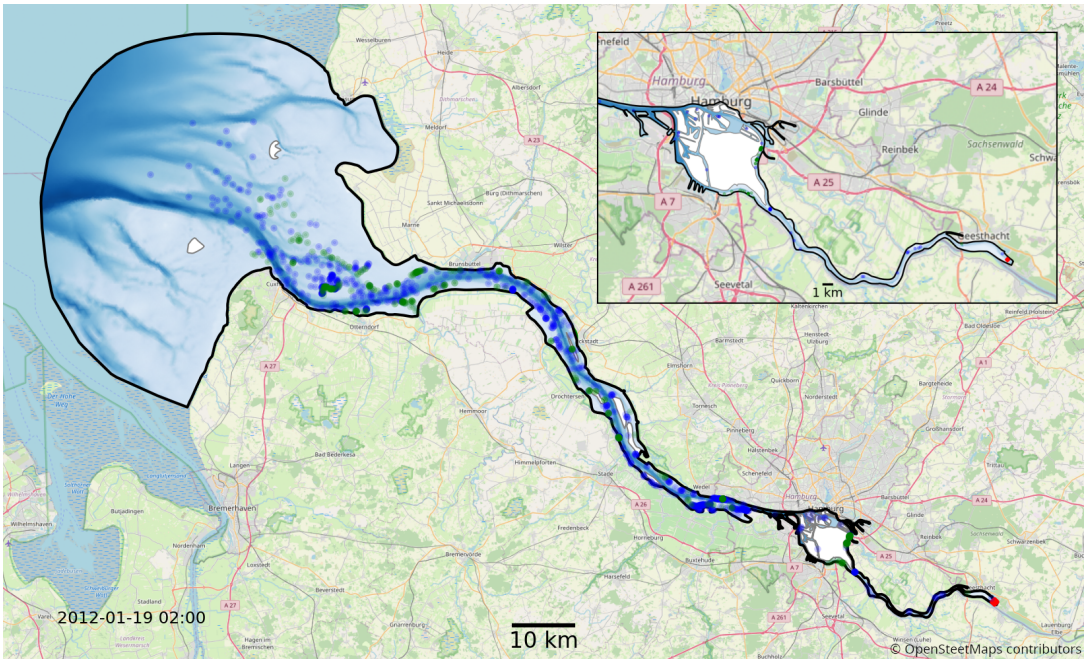

Figure 2.10: Map of the full model domain, with Geesthacht being the upstream boarder on the right and the North-sea being the downstream border on the left. The black outline marks the edge of the model domain. Blue and green dots show an example snapshot of a fraction of the phytoplankton in the model. The location of the initial release is shown in red. Blue represents floating, green particles stranded by the receding tide. The red area is the initial release location. The background map has been provided by © OpenStreetMap contributors 2023. Distributed under the Open Data Commons Open Database License (ODbL) v1.0.

Suspended particulate matter data has been provided by the SediMorph model (Malcherek et al., 2005) developed by the German Federal Waterways Engineering and Research Institute (Bundesanstalt für Wasserbau, BAW). SediMorph is coupled to the hydrodynamic model UnTRIM and provides data on the concentration of suspended particulates for five different size classes (see table 2.2).

Sediment	$-log_2$[mm]	d [μm]
Fine sand	> 3	128 - 256
Very fine sand	> 4	64 - 128
Coarse silt	> 5	32 - 64
Medium silt	> 6	16 - 16
Fine silt	> 7	8 - 16
Very fine silt	> 8	4 - 8

Table 2.2: SediMorph size classes and their corresponding size ranges.

The data was provided based on simulations for the year 2016 as a monthly average with a horizontal resolution ranging from 10 to 1000 m. The data was interpolated to the SCHISM grid as depth averaged values using a barycentric interpolation for the horizontal layer.

In this study we continuously release phytoplankton aggregates representing a subset of the incoming upstream phytoplankton population at the weir in Geesthacht. We then examine how the population distributes throughout the estuary by following their trajectory and, most importantly, their cause of death. As we are primarily interested in their cause of death and the mechanism behind hit we will be ignoring many other biological processes like cell growth and division.

Mortality is induced by one of the following three processes: high salinity, light-limitation or "dry-out" when phytoplankton aggregates are stranded on the shore for to long.

When particles are exposed to *high salinity* water above 20PSU, a mortality probability of 0.5% per minute is imposed. This threshold is chosen based on a range of the salinity tolerances of estuarine phytoplankton species presented in (von Alvensleben et al., 2016). This is only an approximation and salinity tolerances many estuarine phytoplankton species deviate from this. However, the main motivation for this choice is that most of the particles that die through this process have passed the isohaline for more than 12 hours, one tidal cycle, and are assumed not to return again through this isohaline. Anything outside the 20 PSU isohaline is not considered part of the estuary for the purposes of this study. Therefore, we are not tailoring our salinity tolerance to a specific species, but rather testing whether they can retain themselves within this isohaline. This salinity induced mortality also allows us to reach a steady state population size, required to compare upstream and downstream populations easily.

We consider phytoplankton cells that were *stranded* out of the water by the receding tide and have lain dry for more than 7 consecutive days to be dead. Note that these dry cells are not typically devoid of water, but they are considered "dry" if the majority of their area has a water level below 0.1 m. Additionally, in nature, these areas typically contain small sub-resolution structures such as tidal ripples or small puddles and vegetation that allows these areas to remain wet for periods longer than one tidal cycle.

Light limitation is modelled based on observations presented in (Walter et al., 2017). They showed that phytoplankton can survive for several days with little or no light before the population starts to decline. To represent this, we model phytoplankton cells with a light budget. This light budget is represented as a moving average of their past illumination. Illumination is calculated once a minute at their current water depth. (Walter et al., 2017)

showed that cell number growth rates during illumination and cell number death rates during darkness differ by about an order of magnitude. To compensate for this, we calculate the light budget using the maximum of two moving averages. The moving average ($\overline{I}$) of the local irradiance I_a at step $t+1$ is calculated by

$$\overline{I}(I,T)_{t+1} = \overline{I}(T-dt)_t + \frac{I_a(t)}{T} \tag{2.1}$$

which allows them to recover from light limitation faster than they are starved of light. T is the averaging time and dt is the time step between averages. The light budget is then calculated as

$$LB = max(\overline{I}(I,T_g), \overline{I}(I,T_d)) \tag{2.2}$$

where T_d is set to 12 days and T_g is set to 1/10 of T_d.

When the light budget falls below a threshold of $30\,\mathrm{W\,m^{-2}}$, the cells are considered light-limited and die with a probability of approximately $3.5 \times 10^{-5}\,\mathrm{min^{-1}}$ (Walter et al., 2017). The sensetivity of this threshold is examined in a sensetivity analysis presented in Sec. 4.2.2.

The surface light intensity or irradiance is modelled using the pvlib library (Anderson et al., 2023). We use pvlib to calculate the irradiance field based on the position of the sun relative to the location and time of year, assuming a clear sky.

The surface irradiance is then attenuated by the turbidity of the water column using the Beer-Lambert law.

$$I(z) = (1-\alpha_a) I_0 e^{-\epsilon c z} \tag{2.3}$$

where $I(z)$ is the irradiance at depth z, I_0 is the surface irradiance, α_a is the surface albedo, ϵ is the attenuation coefficient, c is the turbidity based on the SPM concentration and z is the depth. The surface albedo is set to 0.1 and the chosen attenuation coefficient is 0.15 m^{-1}.

We represent turbidity induced buoyancy by estimating particle collision and coagulation rates between the phythoplankton cells and the suspended particulate matter.

Typically three processes are considered when representing aggregation processes between organic and inorganic particles in marine environments: differential sedimentation, turbulent shear, and Brownian motion. Brownian motion can be neglected in our case because its effect is several orders of magnitude smaller for the size classes that we are considering. Differential sedimentation represents the potential for particles to aggregate based on different settling velocities causing relative motion between the particles, causing them to potantially collide. Turbulent shear represents the potential of particles to aggregate based on relative motion due to shear or small scale turbulences. We refer to these coagulation processes as different coagulation kernels These kernels can be represented in a rectilinear or curviliniear way. The later accounts for particles avoiding each other due the changes in the local flow field that the particles themselves cause while the first does not. The curviliniear kernels for turbulent shear β^C_{sh} and differential sedimentation β^C_{ds} are defined by

$$\beta^C_{sh} = (\frac{8\pi\epsilon}{15\nu})(1 - \frac{1+5p+2.5p^2}{(1+p)^5})(r_i + r_j)^3 \tag{2.4}$$

$$\beta^C_{ds} = \frac{1}{2}\pi r_i^2 |v_i - v_j| \tag{2.5}$$

where ϵ is the turbulent kinetic energy dissipation rate, ν is the kinematic viscosity of the fluid, p is the particle size ratio r_i/r_j, r_i and r_j are the radii of the particles, v_i and v_j are the sinking velocities of the particles. Turbulent kinetic energy dissipation rate and kinematic viscosities are calculated and provided by the SCHISM model.

Estimating particle sinking velocities for aggregated particles is difficult as particle shape, size, and density can vary significantly between different aggregates. The classical approach using the Stokes law, which assumes that aggregates are spherical and homogeneously dense been show to be inadequate for complex marine aggregates as it drastically overestimates the sinking velocities (Kriest, 2002; Cael et al., 2021; Laurenceau-Cornec et al., 2020). Data availability for aggregates composition and size distritbution is typcially limititing in coastal environments that makes it difficult to apply tailord models. For our case we chose to use an empirical model presented by Kriest (Kriest, 2002). Here sinking velocities are calculated based on a power law and the fractal radius. Whilst there are many other potential models to represent the sinking velocities of aggregates, we found this to be the most suitable as it has been successfully applied in a modeling study already (Kriest, 2002) and because it is tuned to best represtend dense phytoplankton-based aggregates.

Sinking velocities are calculated using

$$v_i(d) = Bd^{\nu} \tag{2.6}$$

d is the diameter of the aggregate, B and ν are fitting constants. Based on the "dense Phytoplankton aggregation model" (dPAM) presented in Kriest they are set to $942d^{1.17}$ m d^{-1}.

We assume that aggregates are sticky due to their exudates. This makes their stickiness proportional to the organic content. We therefore model the stickiness using the ratio of organic to inorganic content presented in (Jokulsdottir and Archer, 2016). The total particle coagulation rate is then calculated by

$$\beta = \alpha_s \frac{V_o}{V_i}(\beta_{sh}^C + \beta_{ds}^C) \tag{2.7}$$

where α_s is the maximum sticking probability of particles upon collision for a completely organic aggregate, V_o and V_i are the volumes of organic and inorganic content in each aggregate, and β_{sh}^C and β_{ds}^C are the curvilinear coagulation kernels for turbulent shear and differential sedimentation. The amount of individual coagulations for each time step is then calculated based on the coagulation probabilities using a Poisson distribution.

Aggregate radius after collision is calculated assuming volume conservation

$$r_a^{t+1} = (r_a^3 + nr_{SPM}^3)^{1/3} \tag{2.8}$$

where r_a is the radius of the aggregate, r_{SPM} is the radius of the SPM particle, and n is the number of SPM particles that collided with the aggregate.

We include a settling and resuspension model to represent tidal stranding and particles settling on the bed of the estuary. Particles become stranded when the current grid cell becomes dry. They are not allowed to move from wet cells to dry cells, by the random walk dispersion applied to all particles. A grid cell is considered dry based on the flag given in the SCHISM hydrodynamic model output. Once this cell is rewetted all stranded particles resuspend and are able to move again. Particles settle on the bed once they attempt to move below the bottom model boundary and are resuspended based on a critical sheer velocity of 0.009 ms^{-1} (see appendix for details). The velocity profile in the bottom layer, or log layer, is calculated by

$$U(z) = \frac{u_*}{\kappa} ln \frac{z}{z_0}, \tag{2.9}$$

where U is the friction velocity representing the drag at height z above the seabed, κ is the van Karman constant, z_0 is a length scale reflecting the bottom roughness, and u^* is the critical

friction velocity. If the friction velocity is above the critical friction velocity the particle is resuspended. Particles that are stranded or settled on the bed are allowed to reproduce.

Particles are not only advected but also dispersed based on eddy diffusivity. This allows us implement a dynamic dispersion that is crucial to represent tidal-pumping processes. Dispersion was modeled using a random walk using a random number generator with a normal distribution. Horizontally the standard distribution of the random walk was set to 0.1 ms^{-1}. The displacement by vertical dispersion ∂z of particle i is calculated by

$$\partial z_i = K_v^{'}(z_i(n))\partial t + N(0, 2K_v(z_i)) \tag{2.10}$$

based on (Yamazaki et al., 2014) where z_i is the vertical position of the particle, $K_v^{'}$ is the vertical eddy diffusivity gradient, K_v is the vertical eddy diffusivity and N is the normal distribution. The term based $K_v^{'}$ is needed to avoid particle accumulation on the top and bottom of the water column from the hydrodynamic model output.

For each particle we log their distance traveled, age, water depth, and status (whether they are drifting or settled on the river bank or bottom). These observables are recorded every 12 hours starting at midnight.

Model simulations and visualizations were performed in Python making heavy use of Numba, a LLVM-based Python JIT compiler (Lam et al., 2015a) to significantly speed up the simulations (Vennell et al., 2021). Trajectories were calculated using a second order Runge-Kutta scheme with a fixed time step of 60 seconds. Flow velocities, like any other hydrodynamic data, were interpolated linearly in time and space using barycentric coordinates, with the exception of water velocity in the bottom model cell, where logarithmic vertical interpolation is used.

Experimental configurations

Conceptually, we run two kind of experimental setups, one with aggregation and one without. These experiments are accompanied by a series of sensitivity analyses to compensate for the lack of calibration data.

We model our population for a period of 1 year. The choice of 1 year is considered reasonable because it covers the full seasonal cycle and is also much longer than the average exit or flushing time of the estuary (see Fig. 2.19). We release 10 individuals per minute for one year at the weir in Geesthacht, resulting in approximately 5 million individuals per case, with approximately 50,000 individuals simultaneously alive. This corresponds to an approximate 1:1 ratio of simulated phytoplankton cells to mesh nodes in the hydrodynamic model at each time step. The released individuals are homogeneously distributed in a volume covering the entire water column at the Geesthacht weir (bottom right in Fig. 2.10).

We also perform a number of sensitivity analyses to account for a lack of validation data. Most importantly, we test a range of different coagulation rates by tuning the sticking probability between 0 and 1 in steps of 0.1. We also test a range of light limitation induced mortality rates by tuning both the required average illumination threshold between 10W and 100W and a mortality rate between 0.03% and 0.0003% per minute when below this threshold.

We will compare the model using two metrics. As we are using a Lagrangian model, we can track the fate of each individual particle, in particular its cause of death. To compare the relative importance of the different mortaility causes, we compare the relative amount of aggregates dying to each of them for different model configurations, e.g. with and without aggregation.

The second metric use is the horizontal distribution of locations at which the death orccured. To visualize these we divide the model domain into equally sized hexagons. The

color of each hexagon indicates the amount of phytoplankton aggregates that have died off in that particular bin. We use these to compare the along-stream alignment of the location of death to the observed oxygen minimum zone which is generally considered to be cause by the degradation and remineralization of the dead upstream phytoplankton.

Computations were performed on the supercomputer Mistral at the German Climate Computing Center (DKRZ) in Hamburg, Germany. The simulations were performed on a compute node with two Intel Xeon E5-2680 v3 12-core processor (Haswell) and 128 GB of RAM with a total run time of approximately 4 hours.

2.2.3 Results

Figure 2.11 and 2.12 shows the relative cause of death for a range of sticking probabilities. A a sticking probability α_s of zero represents the case without aggregation. In the following we will present the results observed throughout the summer months (April-September) while assuming initial aggregate diameters of 10,50 and 100 µm while focusing on the 50 µm case as the default. In the appendix Sec. 4.2.1 and 4.2.2 we are examining the sensetivity regarding the light limitation parameterisation.

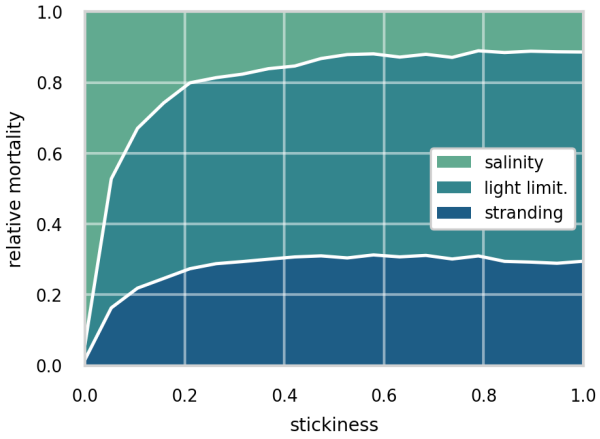

Figure 2.11: Relative cause of death for a range of stickiness parameterisations for an initial aggregate size of 50 µm.

For the 50 µm non-aggregation case (see Fig. 2.11), i.e. stickiness of zero, the main cause of death is salinity with losses due to light limitation around 4% while losses due to stranding are around 1%. Implying that most particles are advected out of the estuaries 20PSU isohaline. With an increase in sticking probability, we see a shift in the cause of death towards light limitation. For a sticking probability of 0.2, light limitation increases to around 53% and finds it maximum around 60% when the sticking probability is set to 1. With an increase in sticking probability, we also see an increase in the relative importance of stranding. Starting at around 1% for the non-aggregating case, it increases to around 28% for a sticking probability of 0.2 and remains that that level for a sticking probability of 1.

Comparing the 50 µm case to the 10 µm and 100 µm cases (see Fig. 2.12), we see a large sensetivity to the initial aggregate size. The importance of light limitation increases quickly with inital aggregate size. For the 10 µm case, light limitation induced mortality is below 20% for all sticking probabilities with salinity induced mortality causing 80% of deaths. Also, note

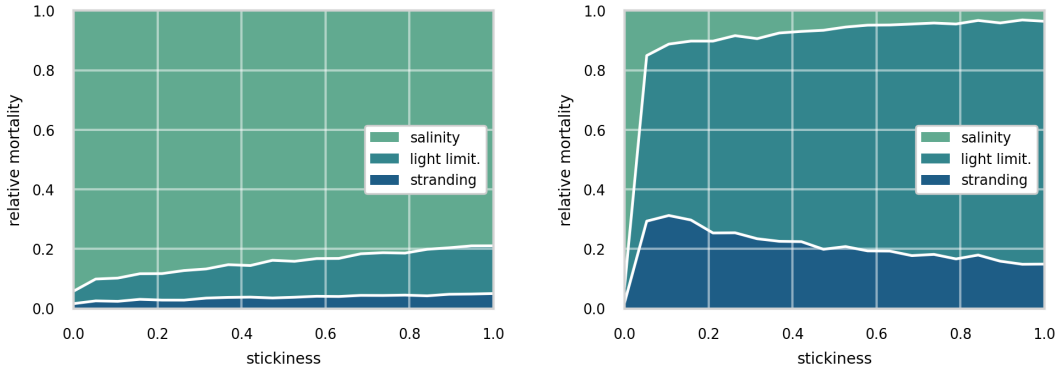

(a) 10 µm (b) 100 µm

Figure 2.12: Relative cause of death for a range of stickiness parameterisations for an initial aggregate size of a) 10 µm and b) 100 µm.

the slow increase in light-induced mortality with increasing sticking probability, compared to the 50 µm or 100 µm cases, rising from approximately 4% at a sticking rate of 0 to just over 17% at a sticking rate of 1.

For the 100 µm case, light limitation induced mortality rapidly increases with sticking probability, reaching over 80% of the total mortality at a sticking probability of 1. For sticking probabilities over 0.1 we also see a decline in relative mortalities for stranding, something we do not see in the other cases, reaching its maximum at 0.1 sticking probabiliy with 30% of the total mortality and declining to 17% at a sticking probability of 1.

We now analyze the horizontal distribution of aggregate deaths with a hexagonal heatmap. Figure 2.13 shows the location of death for the non-aggregating and aggregating for the sommer months (April-September) for non-aggregating case (top) and for the aggregating case (bottom). Both presented cases assume an initial aggregate size of 50 µm. The brightness of the collor in each hexagon indicates the relative amount of phytoplankton aggregates dying at that location. Note, the difference in scale between the two figures with the non-aggregation case ranging up to 1% and the aggregating case up to 12%. Hexagons where no aggregate died within the summer months are not colored.

Comparing the two, we see a clear shift in the location of death. For the non-aggregating case the main area of high mortality are located close to the mouth of the estuary with its peak close to Brunsbüttel. Note that this area coincides not only with a sharp increase in salinity but also in turbidity and ist often refered to as the maximum turbidity zone. A second but significantly less pronounced area of high mortality is located shortly after the bathymetric jump in both the Norder and Süderelbe.

For the aggregating case we see a shift in the location of death away from the maximum turbidity zone towards the bathymetric jump where where the majority - approximatelly 25% - of all aggregates die. A second area of high mortality is located close to the city Stade where two harbor bays seem to act as a sediment trap in our model. The previously observed area of high mortality around the turbidity maximum zone is now less pronounced. While it accounted for over 90% of the mortality in the non-aggregating case, it now accounts for less than 20% of the mortality in the aggregating case.

Taking a look at the outer end of the estuary, we also see a difference in the locations where no particles died. Notably, the tidal flats are largely empty of dead aggregates in the

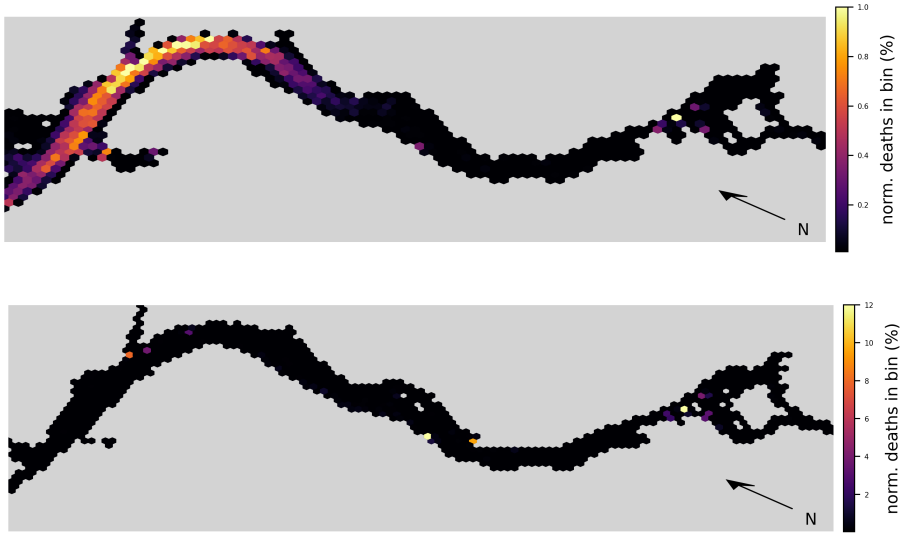

Figure 2.13: Hex-bin heatmap of the location of death for the summer months (April-September). The Hamburgs port area is located on the right with the North Sea to the left. Colors indicate the relative amount of phytoplankton aggregates dying at that location. The top figure represtens the non-aggregating case with yellowish colors indicating a loss greater than 1% of the community at that location, while the bottom figure represents the aggregating case with yellowish colors indicating a loss greater than 12% of the community at that location. Both caseses assume an initial aggregate size of 50 µm.

aggregating case, with almost all deaths occurring within the deeper sections of the estuary.

Interpretation and contextualization of the results

In this study, we examined the effect of aggregation processes on phytoplankton mortality in the Elbe estuary. Primarily, we focused on buoyancy changes due to aggregation with inorganic suspended particulate matter, which are suspected to increase mortality rates due to light limitation. We found that aggregation processes can significantly increase light limitation-induced mortality by over an order of magnitude (as shown in Fig. 2.11). These results were consistent with observed changes in the location of death. The main location of death for phytoplankton aggregates, when accounting for buoyancy changes due to aggregation with suspended inorganic matter, was found to be shortly after the bathymetric jump. This finding is consistent with other studies examining the phytoplankton community from an Eulerian point of view (Pein et al., 2021; Schöl et al., 2014; Schroeder, 1997).

These results are also consistent with a recent taxonomic study by Martens et al. (2024). They showed that the large centric diatoms, which make up the majority of the upstream phytoplankton biomass, exhibit a negative correlation with the downstream position in the estuary. After the bathymetric jump, the composition shifts towards flagellates with the potential for mixotrophy and picophytoplankton (phytoplankton <3 µm in size), both of which have historically been underrepresented in microscopic studies. In the context of our study, the centric diatoms are typically in a size class represented by Fig. 2.12b, while the small picophytoplankton are in a size class represented by Fig. 2.12a. Hence, we suggest that the observed shift in the phytoplankton community composition might partly be explained by the increased light limitation-induced mortality of larger diatoms, the ability of mixotrophic flagellates to actively migrate within the water column, and their capacity to withstand darkness

for longer periods due to their mixotrophic potential.

In our study we tested a range of sticking probabilities ranging from zero to one, i.e. from non-agreggating to always aggregating upon collision. Models representing aggregation that do not distinquish the content of aggregates typically work with sticking probabilities between 0.1 and 0.5 (Burd, 2013; Karakaş et al., 2009; Kriest, 2002), while the models that distinguishes between organic and inorganic content use a sticking probability of 1 (Jokulsdottir and Archer, 2016). Hence, we argue that for our case the sticking probability of 1 is the most realistic as well.

With the increase in depth, the volume for a cross-section segment increases significantly, which could lead one to conclude that the decrease in concentration is due to dilution. However, dilution requires mixing. In this case, it would require mixing the upstream high-chlorophyll freshwater with other low-chlorophyll waters. Because there are no significant tributaries that could dilute the upstream water with other freshwater, the only water that could mix with the upstream water is from the North Sea. While the North Sea water shows a lower chlorophyll concentration than the riverine water, it is also highly saline, with a salinity of above 30 PSU. Hence, any mixing is expected to be visible in the salinity concentrations. Because the collapse happens in a freshwater section of the estuary, with salinities of below 0.1 PSU, we do not expect dilution with seawater to account for the observed decrease in chlorophyll. However, our model design is currently not able to confirm this hypothesis.

Initially, we were surprised to observe how little light limitation contributed to mortality in the non-aggregating case. By examining the vertical velocities and locations of the aggregates, we found that they were traveling up and down the water column quickly, regularly reaching the surface where they could recover from light limitation. This is consistent with the general understanding of the Elbe estuary as a mostly "well-mixed" system. While the time spent at the surface is typically short and does not allow for much primary production, it seems to be sufficient to prevent light limitation-induced mortality in our model.

Model limitations & future perspectives

A major limitation of our study is the lack of grazing representation in our model. We would have liked to include a grazing model to directly compare the suggested light-limitation losses to grazing losses. This was not possible due to technical reasons within the time constraints of this study. Representing grazing losses would require an ecosystem model that tracks the zooplankton community and accounts for changes in, for example, the nutrient concentration field. This would necessitate an online particle tracking model that is directly coupled to the hydrodynamic model, which was too expensive both in terms of development time and computational resources. We hope that this study can motivate further work that includes an aggregation model into the existing Eulerian models to directly compare light limitation losses to grazing losses.

The lack of grazing in our model also limits us to making a weaker statement regarding the relative importance of light limitation losses compared to grazing losses. We are therefore not able to discuss the claim of (Schöl et al., 2014; Kopmann and für Wasserbau, 2014; Pein et al., 2019) that grazing is the main cause of phytoplankton losses in the Elbe estuary. We can only suggest that light limitation losses due to aggregation-enhanced sinking could be a significant cause of mortality.

Another limitation of our study is the uncertainty in the sinking velocities of the phytoplankton aggregates. As we highlighted in the methods section, the sinking velocities are based on a model by Kriest (Kriest, 2002). However, there are many other potential models to represent the sinking velocities of aggregates, as presented in (Cael et al., 2021; Laurenceau-

Cornec et al., 2020). These different models can vary by an order of magnitude in their sinking velocities, making this a major source of uncertainty in our model. Additionally, these models are generally based on marine aggregates formed in significantly different environments than the Elbe estuary, most notably with much lower concentrations of suspended inorganic matter. We therefore assume that our sinking model is, in general, underestimating the sinking velocities of the phytoplankton aggregates, as the aggregates in the Elbe estuary are expected to be much denser than those in the open ocean. Thus, our estimates of the aggregation-induced light limitation losses are likely conservative.

The choice of coagulation kernel, whether to use a rectilinear or curvilinear kernel, also has a large effect on the effective coagulation rates. (Burd, 2013) compared the effects of these kernels on coagulation rates and showed that they can differ by several orders of magnitude, with the difference becoming more pronounced for larger aggregate size differences. See Sec. 4.2.3 for a comparison of coagulation rates between these two kernels. Both kernels are analytically derived; however, a systematic comparison of these kernels in a real-world environment is missing. We chose to use the curvilinear kernels as they are generally assumed to be more accurate and also represent a more conservative estimate of the coagulation rates. Hence, our results of aggregation-induced light limitation losses are also a conservative estimate in that regard as well.

Another process that we neglect is the deaggregation of the phytoplankton aggregates. Shear and turbulence can cause the breakup of aggregates into smaller particles, which limits their size since they are more likely to deaggregate the larger they become. This would be an interesting process to examine in our model, especially because we represent sinking speeds based on aggregate size. However, deaggregation is even less understood than aggregation, with next to no applicable data available. While some marine snow aggregation models include deaggregation processes, they represent them as fixed deaggregation rates or fixed upper size limits in a zeroth-order approximation (Burd, 2013; Karakaş et al., 2009; Jokulsdottir and Archer, 2016). Without data available to tune these rates, we decided to ignore this process in our model. We believe this to be reasonable as our aggregates are quickly growth-limited by Equation 2.7 and rarely exceed 1 mm in size.

We limit our aggregation model to inorganic particles exclusively. Hence, organic phytoplankton aggregates only aggregate with inorganic suspended matter. While this is a simplification, we believe it is justified by the difference in concentration between organic and inorganic particles. Particle concentration differences between organic and inorganic particles in the starting harbor, where most of the coagulation occurs, are around 1:1000. Assuming that they are of similar size, this also corresponds to a ratio in expected collisions of 1:1000, allowing us to ignore this process. Organic matter concentrations in the sediments of the channel are similarly low, with concentrations of less than 5% (Spieckermann et al., 2022). Aggregation processes can become strongly limited by the ratio of organic content in the larger aggregates, drastically reducing the sticking probability of aggregates with inorganic particulates, which could compensate for the difference in particle concentrations. Representing organic-to-organic aggregation would either require an online particle tracker that keeps track of the organic particle concentration or drastically increase the number of particles represented in the model (typical phytoplankton aggregate concentrations in nature can exceed million aggregates per cubic meter). Both options were infeasible, so we decided to ignore this process in our model.

We use hydrodynamic and SPM data representing the year 2012 and 2016 respectively. It would have been ideal to use data from the same year, but the two distingued models did not offer any overlapping years. While this represents an obvious inaccuracy we assume that this is justifiable as the bathymetriy did not change significantly between these years. To mask

the natural variability between these datasets we used the SPM concentraions as monthly averages.

Outlook

We would like this study to be read as a proof of principle. We showed that aggregation processes can significantly increase light limitation-induced mortality in the Elbe estuary. Yet, we were not able to include grazing processes, which are currently assumed to be the major driver for phytoplankton community collapse. To achieve a better understanding of the relative importance of these processes, they would need to be integrated into a single model. This could be accomplished by either developing an interface between OceanTracker and SCHISM to enable online particle tracking or by implementing aggregation processes and size- and density-dependent buoyancy into existing Eulerian models. While the first approach would enable many interesting studies, it would also be more difficult to implement. The latter approach seems to be the simpler and more feasible way forward.

Another completely different approach to tackling this problem would be to gather zooplankton data. This would enable us to directly estimate filtration volumes and therefore grazing losses in the estuary, allowing us to evaluate the validity of the grazing hypothesis without a complex modeling study.

2.3 Study III:

Phytoplankton retention mechanisms in estuaries: a case study of the Elbe estuary

2.3.1 Abstract

Due to their role as primary producers, phytoplankton are essential to the productivity of estuarine ecosystems. However, it is important to understand how these nearly passive organisms are able to persist within estuaries when river inflow results in a net outflow to the ocean. Estuaries also represent challenging habitats due to a strong salinity gradient. Little is known about how phytoplankton are able to be retained within estuaries. We present a new individual-based Lagrangian model of the Elbe estuary which examines possible retention mechanisms for phytoplankton. Specifically, we investigated how reproduction, sinking and rising, and diel vertical migration may allow populations to persist within the estuary. We find that vertical migration, especially rising, favors retention, while fast sinking does not. We further provide first estimates of outwashing losses. Our simulations illustrate that riverbanks and tidal flats are essential for the long-term survival of phytoplankton populations, as they provide refuges from strong downstream currents. These results contribute to the understanding needed to advance the ecosystem-based management of estuaries.

2.3.2 Introduction

Estuaries are highly productive ecosystems. Their relatively small area disproportionally contributes to the global carbon cycle, along with their roles as a source of nutrients and hatching grounds for marine ecosystems (Cloern et al., 2014; Arevalo et al., 2023). Estuaries are of great importance for anthropogenic use, which also exposes them to many stressors such as diking, dredging and fishing (Jennerjahn and Mitchell, 2013; Brown et al., 2022; Wilson, 2002). Estuaries present challenging dynamics to their smallest residents due to their strong salinity gradient and net transport to the ocean. Here, we explore how phytoplankton, drifting small primary producers that form the basis of estuarine food webs, can persist within such dynamic environments.

Like most ecosystems, estuarine ecosystem dynamics are strongly controlled by primary producers, in particular phytoplankton (Chen et al., 2023). Apart from biofilm-forming phytoplankton, which are attached to their substrate (Cheah and Chan, 2022), the vast majority of phytoplankton organisms drift passively in currents, though they may be able to influence their vertical movement. With the estuary having a net outwards flow, we would expect phytoplankton to move downstream over time and to be washed out from limnic waters into marine waters via brackish waters. Hence, the question of how phytoplankton, the drifting base of estuarine food webs, are able to maintain their population size without declining due to the net transport into the open ocean arises. If we assume that the population is not exclusively maintained by a self-maintaining source population upstream that is washed into the estuary, then there must be some sort of retention mechanism that enables the phytoplankton population to persist within the estuary.

There are different theories about how estuarine phytoplankton populations are able to maintain their position. Previous observational studies suggested several possible mechanisms that could enable the retention of phytoplankton populations within estuarine systems: vertical migration – in the form of sinking, rising, or diel migration – and stickiness.

Diel vertical migration is a process where organisms move up and down in the water column in response to the sun. This movement may favor retention by allowing plankton to reduce the time they spend in the faster downstream currents at the water surface. A study by (Anderson and Stolzenbach, 1985) showed that diel-migrating dinoflagellates were able to outcompete other non-motile phytoplankton in an embayment environment and even compensate for outwashing losses through reproduction, increasing their abundance. However, this also implies that the growing part of the population is somehow retaining their position. If the regrowing population is also continuously drifting downstream it will not be able to sustain itself in that area and will ultimately die out due to unfavorable salinity conditions in marine waters (Admiraal, 1976; von Alvensleben et al., 2016; Jiang et al., 2020). The presence of diel migration has mostly been demonstrated for motile phytoplankton such as dinoflagellates (Hall et al., 2015; Crawford and Purdie, 1991; Hall and Paerl, 2011) and zooplankton species (Kimmerer et al., 2002). While the motivation for diel migration differs for autotrophs, mixotrophs, and heterotrophs, the consequence remains the same: an upward movement during the day and a downward movement during the night.

Estuaries are complex and strongly dynamic systems, such that it is still difficult to predict their ecosystem dynamics or the effects of anthropogenic impacts due to their complex bathymetry (MacWilliams et al., 2016; Fringer et al., 2019). Nevertheless, there are sophisticated estuarine models that are able to reproduce the complex dynamics of estuaries reasonably well. This includes currents and water levels on the physical side but also chlorophyll concentrations and other biologically driven properties (Pein et al., 2021; Schöl et al., 2014). However, these are Eulerian models. This means that they are based on a fixed grid and

calculate the concentration of a tracer, such as phytoplankton, at each grid cell. This makes it difficult to study concepts such as retention times, as they lack temporal consistency, meaning that the life history and trajectory of a phytoplankton cell cannot be tracked. Previous modeling studies have attempted to overcome this problem using a Lagrangian approach. A Lagrangian model does not try to track, e.g., concentrations at fixed positions but rather follows the motion of individual particles that can be used to represent, e.g., water parcels or organisms. Their ability to resolve the interactions of individual phytoplankton cells or aggregates with the bathymetry (e.g., through settling or stranding) while maintaining temporal consistency is essential for investigating retention mechanisms.

(Simons et al., 2006) and (Kimmerer et al., 2014) used a Lagrangian model to study zooplankton retention. (Simons et al., 2006) examined the dispersal and flushing times of mussel larvae in the St. Lawrence estuary, while (Kimmerer et al., 2014) examined zooplankton movement in the San Francisco estuary. They were able to show that sinking and diel vertical migration slow the outwashing process and might be a beneficial retention strategy. However, they did so by ignoring key processes like reproduction, mortality, stranding, and sedimentation processes. Moreover, both studies were based on low-resolution structured grid models, which, we suspect, under-represent the complex bathymetry of estuarine systems (Ye et al., 2018).

Diatoms or benthic microalgae in particular have been observed to be strongly negatively buoyant and hence sink to the riverbed, remaining there for a long time (Passow, 1991; Thomas Anderson, 1998). Studies also found that phytoplankton aggregates have sticky compounds that are suspected to allow them stick to suspended particles, enabling them to sink to the riverbed or stick to their surroundings, aiding retention (Kiørboe and Hansen, 1993; van der Lee, 2000).

In summary, different retention mechanisms have been observed or examined in modeling studies. However, the observational studies were performed in isolation and major simplifications were used in the modeling studies. There is currently a lack of theoretical studies that allow for a more comprehensive overview of the interplay of vertical migration and reproduction in combination with settling and stranding as retention mechanisms.

Here, we explore possible retention mechanisms of phytoplankton, using the Elbe estuary as a case study. This is located in the north of Germany and flows into the North Sea. Like most alluvial estuaries, it is relatively shallow, with most of it averaging only a few meters in average depth. Similar to other European estuaries, it has experienced strong anthropogenic pressure over the last few centuries, most notably diking (to restrain it to a narrow channel) and dredging (to improve access to Hamburg harbor). Unlike other major European ports, the port of Hamburg is located far (roughly 100 km) from the coast. To create port access, the main channel is dredged and presents a sudden jump in bathymetry from approximately 5 m at the border of the city to up to 20 m in the port and downstream (see Fig. 2.14). This bathymetric jump is suspected to be the cause of a collapse in the phytoplankton population in the area, as the jump results in an increase in oxygen depletion and high ammonium remineralization downstream of the bathymetric jump (Schroeder, 1997; Holzwarth and Wirtz, 2018; Sanders et al., 2018). Ongoing dredging is carried out to maintain the depth of the navigational channel, causing high turbidity (Kappenberg and Grabemann, 2001). While important aspects of the along-channel biochemical dynamics have been studied, little is known about the shore-to-shore dynamics (Goosen et al., 1999; Dähnke et al., 2008; Sanders et al., 2018).

For this purpose, we further developed the individual-based Lagrangian model OceanTracker (Vennell et al., 2021) and applied it to the Elbe estuary using the hydrodynamics calculated by a recent model, SCHISM (Pein et al., 2021). While the Lagrangian model sim-

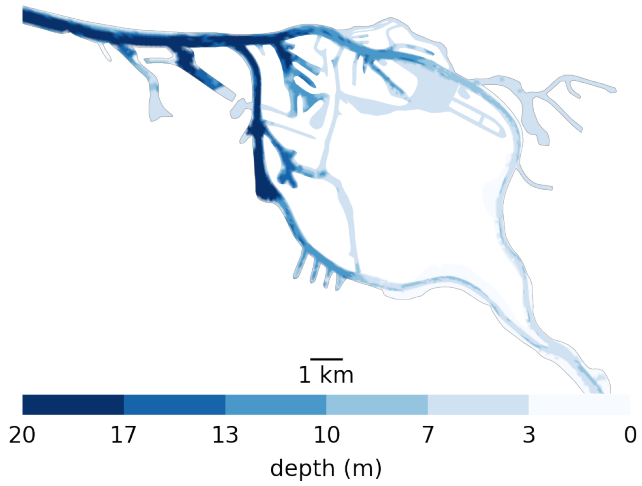

Figure 2.14: Bathymetry used in the Elbe model around Hamburg. Note the bathymetric jumps from 5 m upstream (the right-hand side) to 10 m for a short step in the upper port area to 20 m in the lower port area all the way to the North Sea. Also note that there is only one channel to enter the harbor section of the estuary, which is 20 m deep from shore to shore. So anything that passes through has to travel through deep water.

ulated the movement of the inanimate organisms, we included key phytoplankton features such as reproduction and mortality, sinking and rising, and diel vertical migration. Using this model, we investigate the conditions under which phytoplankton retention can be reproduced.

2.3.3 Methods

Model description

In our study we use a Lagrangian approach with the particle tracking model OceanTracker (Vennell et al., 2021). While off-line particle tracking on unstructured grids has been relatively computationally expensive until recently (Vennell et al., 2021), it offers several advantages. Firstly, it allows us to reuse computationally expensive hydrodynamic models to model tracer-like objects. This is much faster overall than recalculating the advection–diffusion equation in an Eularian model. Secondly, because we are simulating individually particles, we are able to observe their tracks. In our model, we use these particles to represent phytoplankton cells. Alternatively, these particles could also be interpreted as aggregates colonized by phytoplankton. The temporal consistency of a Lagrangian model – the fact that we know the history of each particle – makes the interpretation of our results more intuitive and allows us to include individual-based properties and processes that cannot be represented in Eulerian models, e.g., retention times.

We use the hydrodynamic data generated by the latest SCHISM model of the Elbe estuary (Pein et al., 2021) from the weir at Geesthacht to the North Sea, including several side channels and the port area (see Fig. 2.10). SCHISM solves the Reynolds-averaged Navier–Stokes equations on unstructured meshes, assuming hydrostatic conditions and using a time step of 60 seconds. The unstructured mesh is three-dimensional and consists of 32 000 horizontal nodes that use terrain-following coordinates based on the LSC2 technique (Zhang et al., 2016) for the vertical grid, allowing a maximum of 20 levels. Regions with depths of less than 2 m are resolved using only one vertical level. Bathymetric data were provided by the German Federal Maritime and Hydrographic Agency (Bundesamt für Seeschifffahrt und Hydrographie,

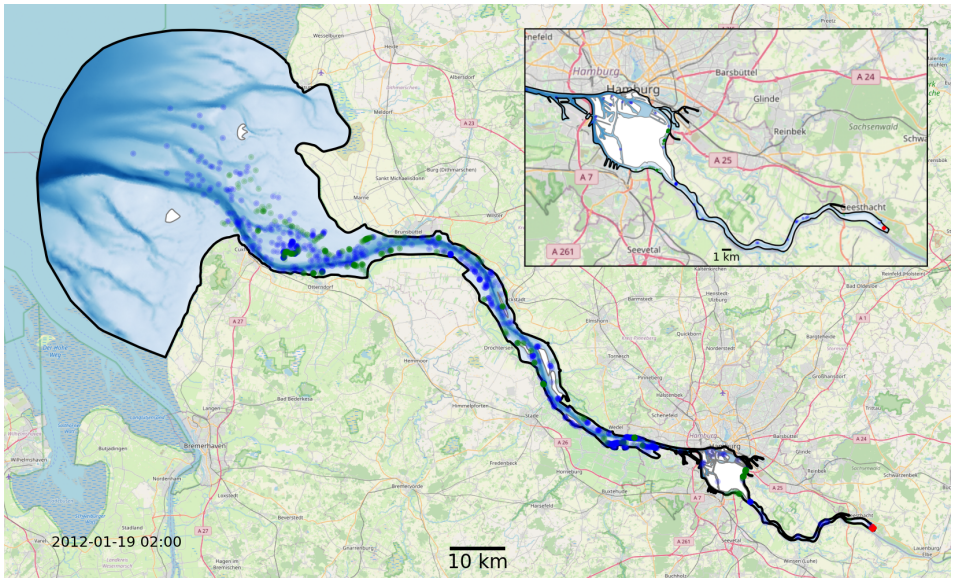

Figure 2.15: Map of the full model domain, with Geesthacht representing the upstream border on the right and the North Sea representing the downstream border on the left. The black outline marks the edge of the model domain. Blue and green dots indicate snapshots of the status of a fraction of the phytoplankton in the model. The location of the initial release is shown in red. Blue represents floating phytoplankton; green represents phytoplankton stranded by the receding tide. The background map was provided © OpenStreetMap contributors 2023. Distributed under the Open Data Commons Open Database License (ODbL) v1.0.

BSH) and the German Waterways Agency (Wasserstraßen- und Schifffahrtsamt, WSA) and have a horizontal resolution of 50 m in the German Bight, 10 m in the Elbe estuary, and 5 m in Hamburg port (Stanev et al., 2019). The boundary conditions on the seaward side include the sea surface elevation, horizontal currents, salinity, and temperature (Stanev et al., 2019), and those on the landward side include the discharge and temperature of the Elbe River. Atmospheric forcing includes wind, air temperature, precipitation, and shortwave and longwave radiation (Stanev et al., 2019). Model validation is based on tide gauge stations and long-term stationary measurements of salinity, water temperature, and horizontal currents. Biochemical variables, including chlorophyll, are based on long-term measurements at the Seemannshöft and Grauerort stations (Pein et al., 2021). The model provides us with a node-based mesh containing a range of information such as water velocity, salinity, water level, and dispersion. The year represented by that dataset is 2012. The temporal resolution of the dataset is 1 hours, and it has dynamically varying spatial resolution, with the distance between nodes ranging from 5 to 1400 m (the median distance is approximately 75 m).

We give a set of biological features to the otherwise inanimate organisms. These features include reproduction and mortality, vertical movement in the form of sinking, rising, or diel vertical migration, stranding, and settling on the riverbed.

Reproduction is represented as a fission process where each phytoplankton cell has a probability of splitting, effectively producing a copy. This is a novel feature applied in OceanTracker that has not been included in any previous Lagrangian model of this type. OceanTracker's recent advances in computational efficiency (Vennell et al., 2021) and buffer handling make it possible to simulate a large number of particles over a long period of time on unstructured grids for the first time. We perform multiple simulations for a range of reproduction rates, implemented as fission probabilities evaluated every minute, that are constant over the life-

time of the cell. While a fixed reproduction rate is a simplification that does not allow for more realistic simulation of the population dynamics of a particular species, it does allow us to investigate the general mechanisms that enable plankton retention.

Mortality is induced by one of three processes: high salinity, drying out while stranded, or long-term light limitation. When particle cells are exposed to high-salinity water (above 20 PSU), a mortality probability of $0.5\,\%\,\mathrm{min}^{-1}$ is applied, with dead phytoplankton cells removed from the simulation (see the salinity map in Fig. 4.8). This threshold was chosen based on the range of salinity tolerances of the estuarine phytoplankton species presented in (von Alvensleben et al., 2016). This is only an approximation, and the salinity tolerances of many estuarine phytoplankton species deviate from this. However, the main motivation for this choice is that most of the phytoplankton cells that die through this process have been beyond the isohaline for more than 12 hours (one tidal cycle), after which it is assumed that they will not return through this isohaline. Anything outside the 20 PSU isohaline is not considered part of the estuary for the purposes of this study. Therefore, we are not tailoring our salinity tolerance to a specific species but rather testing whether they can persist within this isohaline. We consider phytoplankton cells that were stranded out of the water by the receding tide and have lain dry for more than 7 consecutive days to be dead and remove them. Note that these dry cells are not typically devoid of water, but they are considered "dry" if the majority of their area has a water level below 0.1 m. Additionally, in nature, these areas typically contain small sub-resolution structures such as tidal ripples or small puddles and vegetation that allows these areas to remain wet for periods longer than one tidal cycle. There are currently no studies investigating the time range for the survival of phytoplankton stranded on tidal flats or marshes in estuaries. Therefore, we performed a sensitivity analysis to determine the effect of this parameter on the retention success of the phytoplankton population (see Appendix 4.3.1). Phytoplankton cells will also die if they are light limited for 14 days. This value is based on measurements presented in (Walter et al., 2017) which imply that the majority of the phytoplankton are dead after 14 days of light limitation. A sensitivity analysis for this parameter is presented in Appendix 4.3.2. They are considered light limited below a depth of 1 m, as estimated with the Beer–Lambert law using SPM data presented in (Stanev et al., 2019). The initial batch of phytoplankton cells start their life with a full light budget of 14 days, and each minute below 1 m reduces this budget by 1 min, while the opposite applies if the cells are above 1 m. When a cell splits, both inherit the same remaining light budget.

We investigate the effects of different patterns of vertical motion. The first is monodirectional upward or downward vertical motion, representing either positively or negatively buoyant phytoplankton. This buoyancy can be interpreted as either being due to the active choice of buoyancy by the organism through adaptation or being governed by the suspended matter aggregate on which it lives. For monodirectional vertical motion, we assign each phytoplankton cell a vertical velocity which remains constant throughout its lifetime. The second mode of vertical motion is diel vertical migration. Here, phytoplankton cells change their direction of motion based on the current phase of the sun, creating a motion pattern where they rise during the day and sink during the night. This behavior is often assumed to be performed to maximize light capture while avoiding predation – or, as we suspect, to increase retention.

We include a settling and resuspension model to represent tidal stranding and phytoplankton cells settling on the bed of the estuary. Stranded phytoplankton and microphytobenthos have been shown on several occasions to be a major driver of estuarine primary production (Carlson et al., 1984; De Jonge and Van Beuselom, 1992; Kromkamp et al., 1995; Savelli et al., 2019). Phytoplankton cells become stranded when the current grid cell becomes dry, and they

stay in place until they are resuspended or dry out. They are not allowed to move from wet cells to dry cells by the random walk diffusion applied to all phytoplankton cells. A grid cell is considered "dry" based on the flag it is given in the SCHISM hydrodynamic model output. Once this grid cell is flooded again, all the stranded phytoplankton cells are resuspended and able to move again. Phytoplankton cells settle on the bed once they attempt to move below the model's bottom boundary, and they are resuspended based on a critical sheer velocity of $0.009\,\mathrm{m\,s^{-1}}$. The velocity profile in the bottom layer, or log layer, is calculated by

$$U(z) = \frac{u_*}{\kappa} \ln \frac{z}{z_0}, \tag{2.11}$$

where U is the friction velocity (representing the drag at height z above the seabed), κ is the von Kármán constant, z_0 is a length scale reflecting the bottom roughness, and u^* is the critical friction velocity. If the friction velocity is above the critical friction velocity, the phytoplankton cell is resuspended. Phytoplankton cells that are stranded or have settled on the bed are allowed to reproduce. Phytoplankton cells are not only advected but also diffused based on eddy diffusivity, which is crucial to represent tidal-pumping processes. Diffusion is modeled using a random walk obtained using a random number generator with a normal distribution. Horizontally, the standard distribution of the random walk is set to $0.1\,\mathrm{m\,s^{-1}}$. The vertical displacement of a phytoplankton cell ∂z_i is calculated by

$$\partial z_i = K'_\mathrm{v}(z_i(n))\partial t + N(0, 2K_\mathrm{v}(z_i)), \tag{2.12}$$

based on (Yamazaki et al., 2014), where z_i is the vertical position of the phytoplankton cell, K'_v is the vertical eddy diffusivity gradient, K_v is the vertical eddy diffusivity, and N is the normal distribution. The term K'_v is needed to avoid phytoplankton accumulation at the top and bottom of the water column in the hydrodynamic model output.

For each phytoplankton cell, we log their distance traveled, age, water depth, and status (whether they are drifting or have settled on the river bank or bottom). This allows us to, for example, compare a successfully retained phytoplankton cell (older than 3 months) with an unsuccessfully retained phytoplankton cell (dead after less than 3 months). These observables are recorded every 12 hours starting at midnight.

Model simulations and visualizations are performed in Python, making heavy use of Numba, a LLVM-based Python JIT compiler (Lam et al., 2015a), to significantly speed up the simulations (Vennell et al., 2021). Trajectories are calculated using a second-order Runge–Kutta scheme with a fixed time step of 60 seconds. Flow velocities, like all other hydrodynamic data, are interpolated linearly in time and linearly in space on the vertical axis and on the horizontal axis using barycentric coordinates, with the exception of water velocity in the bottom cell, where logarithmic vertical interpolation is used to represent drag forces more accurately.

Experimental configurations

We perform two sets of experiments to test the influences of different vertical movements on the retention success of phytoplankton in the Elbe estuary.

In the first experiment, we examine a range of different monodirectional upward or downward particle velocities from -10 to $+10\,\mathrm{mm\,s^{-1}}$ in $2\,\mathrm{mm\,s^{-1}}$ steps, which represent sinking or rising phytoplankton organisms (Fennessy and Dyer, 1996). Each vertical velocity is examined for a range of different reproduction rates expressed as population doubling times ranging from 40 to 404 days with logarithmic scaling. In the following, we use "reproduction rate" to refer to the prescribed population growth rate under idealized conditions and "growth rate" whenever we describe the population growth in nature. The prescribed population growth rate can be

interpreted as the potential average net doubling time in the presence of predation, mortality, and nutrient availability when testing the effect of outwashing. In the second set of model experiments, we study the influences of possible diel vertical migration patterns for the same vertical velocities and reproduction rates. Hence, a total of 187 different scenarios are tested.

In both sets of experiments, we release 10 000 individuals representing a subset of the the studied phytoplankton population at the beginning of the year. This results in over 1 billion individual particles being simulated for each case, with approximately 1 million simultaneously active particles counted over all cases for a total of 500 000 time steps. This corresponds to an approximately 1:1 ratio of simulated phytoplankton cells to mesh nodes in the hydrodynamic model at each time step. The initial population is homogeneously distributed in a volume covering the full water column at the weir in Geesthacht (see Fig. 2.15), and we examine how the population distributes itself over the estuary and whether it is able to maintain its population size over time. Conceptually, we consider a population to be successfully retained if it is able to sustain itself over the long term or even shows growth. Practically, this is evaluated by comparing the population size at the end of the year to the size after release. The choice of 1 year is considered reasonable because it covers the full seasonal cycle and is also much longer than the average exit or flushing time of the estuary (see Fig. 2.19). The first 3 months of the simulations are considered an initial model spin-up time during which the initial population is dispersed downstream throughout the estuary. Population size changes are measured at the end of the year relative to the population size after this initial spin-up time.

Computations were performed on the supercomputer Mistral at the German Climate Computing Center (DKRZ) in Hamburg, Germany. The simulations were performed on a compute node with two Intel Xeon E5-2680 v3 12-core processors (Haswell) and 128 GB of RAM for a total run time of approximately 4.5 hours.

2.3.4 Results

Retention success in different scenarios

The results of the retention experiments are visualized as heatmaps in Fig. 2.16. Figure 2.16a shows the results for the monodirectional vertical migration scenarios, i.e., constant sinking or rising. Figure 2.16b shows the results for the diel vertical migration scenarios. Each pixel in the heatmap represents a simulation with a specific combination of vertical velocity and reproduction rate expressed as a population doubling time. The color indicates the relative population change after 1 year. White pixels and the boundary between green and brown pixels represent net-zero growth rate simulations. In this case, the losses are equal to the growth. Therefore, we can use the reproduction rate as an estimate for the total relative losses due to downstream transport, drying out while being stranded, and light starvation.

Our simulations show that the population is able to successfully persist under certain conditions. Passively drifting phytoplankton are able to sustain themselves in the estuary if they have a reproduction rate that doubles their population size within approximately 3 months (see Fig. 2.16). Note that the growth rates realized in nature may vary from this value due to, e.g., nutrient or temperature limitations. The reproduction thresholds should be interpreted as an upper bound rather than an accurate estimate of the growth rate.

For the case of monodirectional movement, we see that a higher positive velocity (representing buoyancy) and higher reproduction rates are more beneficial for retention success than a downward-oriented velocity (sinking) and lower reproduction rates. As expected, simulations in which the reproduction is set to zero do not show any retention success. While it is easy to understand that high reproduction rates aid retention, we were surprised that

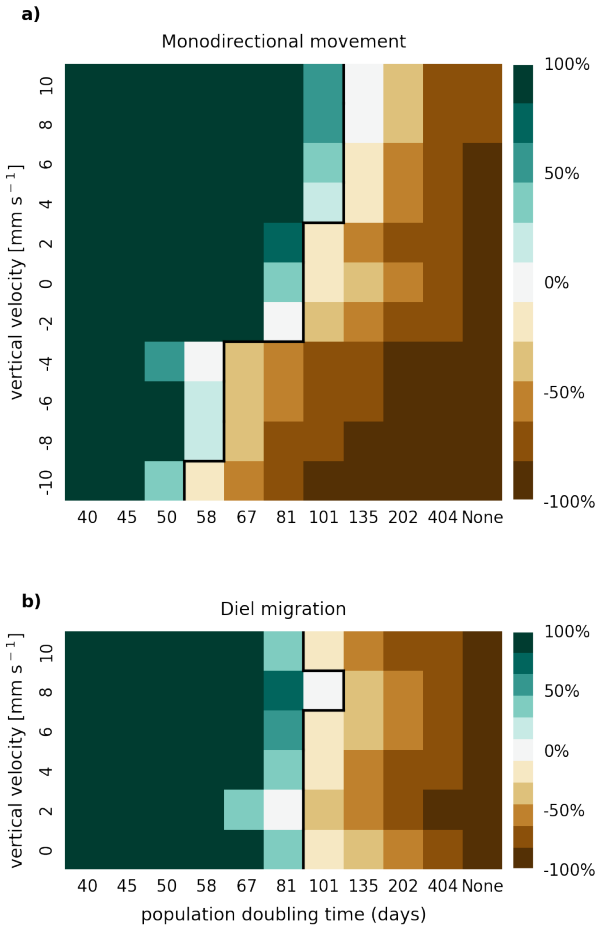

Figure 2.16: Relative population changes for the monodirectional movement **(a)** and diel migration **(b)** scenarios. Positive vertical velocities indicate an upwards drift. Positive population changes represent a retention success (green), while negative population changes represent an eventual total loss of the population (brown). The vertical black lines indicate the boundary between the successfully and unsuccessfully retained scenarios.

buoyant phytoplankton cells are more successful at maintaining their growth in an estuary than sinking ones.

For the case of diel vertical migration in the velocity range of 4 to 10 $\mathrm{mm\,s^{-1}}$, we see equal or higher retention success compared to the case with no vertical migration. A diel velocity of 2 $\mathrm{mm\,s^{-1}}$ is less successful than no migration. Most importantly, none of the diel migration scenarios improve the retention success when compared to passively drifting organisms.

Spatial factors

We now take a closer look at spatial factors that allow phytoplankton cells to maintain net growth in the estuary. For this analysis, we used data from both sets of experiments, i.e., from all cases. Figure 2.17 compares two box plots of the average water depth at the location of each phytoplankton cell: the first box plot is for those cells that remained alive for less than 3 months (short living) and the second is for those cells that remained alive for more than

3 months (long living). Depth is measured relative to the current water surface. Therefore, a value greater than zero indicates that the phytoplankton cell is stranded on the shore during an ebb tide. For reference, the water level varies on average by about 5 m due to the tides (Stanev et al., 2019; Schöl et al., 2014). These analyses show that long-living phytoplankton predominantly live close to the river banks in shallower waters or on tidal flats.

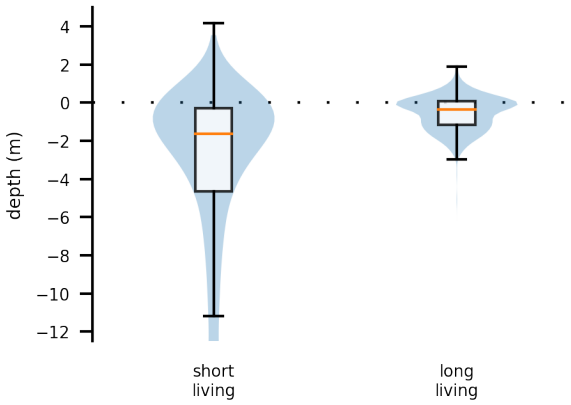

Figure 2.17: Box and violin plots showing vertical distributions of phytoplankton that are passively drifting. The plot labeled "short living" is for the phytoplankton younger than 3 months, and the plot labeled "long living" is for all those older than that. Depth is measured relative to the current water surface, with positive numbers indicating phytoplankton above the water surface, i.e., stranded on the shore.

Moreover, we analyze the horizontal spatial distribution of long- and short-living phytoplankton in Fig. 2.18. To do this, we divide the model domain into equally sized hexagons. The color of each hexagon indicates the average age of the phytoplankton cells within it, calculated across all cases. Note that the spatial age structure is similar for all cases. Hexagons with a yellow color indicate an average age of over 3 months. These yellow areas are mainly found along the river banks in shallow waters or tidal flats.

For comparison, the average exit time for water parcels to reach the 20 PSU isohaline per hexagon is shown in Fig. 2.19. This calculation is based on a separate simulation where we released approximately 1.8 million particles that were homogeneously distributed over

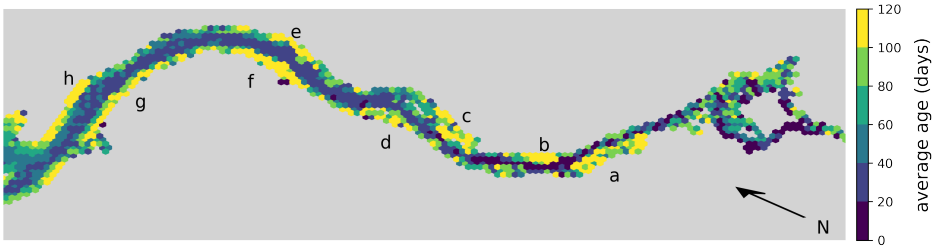

Figure 2.18: Hex-bin heatmap of the average age of phytoplankton cells in the Elbe estuary across all cases. Hamburg's port area is located on the right, with the North Sea to the left. Colors indicate the age of the phytoplankton, with yellowish colors indicating an average age of over 3 months. Yellow areas are mainly found along the river banks in shallow waters or tidal flats. The important areas are Mühlenberger Loch **(a)**, Wedeler Marsch **(b)**, Haseldorfer Binnenelbe **(c)**, Asseler- and Schwarztonnensand **(d)**, at the mouths of the Stör **(e)** and Wischhafener Süderelbe **(f)**, and at Nordkedding **(g)** and Neufelder Marsch **(h)**.

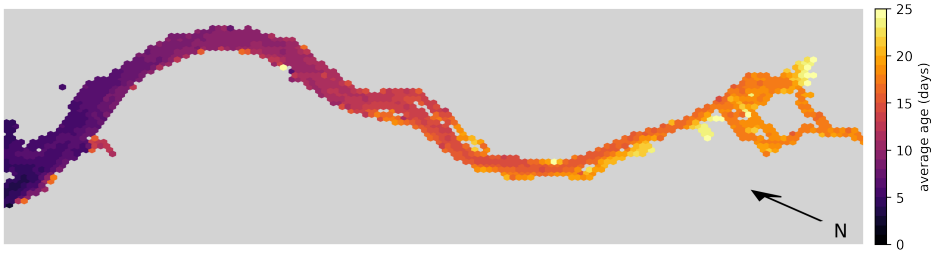

Figure 2.19: Hex-bin heatmap showing the average exit times from the Elbe estuary (Hamburg's port area, as shown in Fig. 2.14, is on the right) without any reproduction, light limitation, stranding, or settling on the riverbed. The color indicates the time taken for a water parcel to reach the 20 PSU isohaline from the hexagon in which it originated.

the estuary. We released one batch in winter during high-discharge conditions on 1 January and another batch in summer during low-discharge conditions on 1 July. Note that for this simulation, reproduction, light limitation, stranding, and settling on the riverbed were disabled to isolate the effect of advection and dispersion.

To further investigate the reasons for the positive effect of buoyancy and the importance of shallow waters and tidal flats, we repeated the first set of simulations and disabled the reproduction of settled and stranded phytoplankton. Under these conditions, populations were unable to persist within the estuary, regardless of their vertical velocity and reproduction rate, indicating that tidal flats are essential for the survival of the population.

Interpretation and contextualization of the results

In this study, we investigated different strategies to explain how phytoplankton populations are able to maintain their population sizes in estuaries while constantly being at risk of being transported into the open ocean.

The limit on the population doubling time that we found necessary for the survival of passively drifting plankton is about 4 months (see Fig. 2.16). Doubling times typically realized in nature are of the order of a few days, which is 2 orders of magnitude smaller than those that we found necessary in our model (Koch et al., 2004; Wirtz, 2011). The low reproduction rates required for successful retention demonstrate that our model is also meaningful under more realistic environmental conditions, for example, if maximum growth rates cannot be reached due to nutrient or temperature limitations.

Our results suggest that shallow areas are very important for maintaining the estuary phytoplankton population. Plankton that consistently find themselves in areas that fall dry due to the tides will regularly become stranded and therefore do not move for much of the tidal cycle. We further see that positively buoyant plankton are more successful at maintaining themselves. This is probably because they are more likely to be transported high up on the river bank, where the water is less likely to reach them. This effect is emphasized in flatter regions, as the distance between the wash margin and constantly flooded areas is larger, increasing the chance of settlement or of them becoming stranded again.

Initially, we expected sinking phytoplankton to have a higher retention success than buoyant ones. However, we found that faster sinking phytoplankton are less successful at persisting. Sinking velocities of less than $2\,\mathrm{mm\,s^{-1}}$ are common for diatoms (Passow, 1991), while larger velocities have been observed for aggregates in the Elbe estuary (Fennessy and Dyer, 1996). Sinking phytoplankton have a reduced downstream velocity because they either settle on the

riverbed, where they do not move at all, or they become close to the bed, where the average downstream velocity is lower. In addition, due to temperature-induced density stratification, the deeper water layers of the Elbe either have, on average, a lower downstream velocity than the upper water column or they move upstream (Pein et al., 2021). Nevertheless, buoyant phytoplankton showed more successful retention in our simulations. The low chance of survival in the estuary for sinking phytoplankton might be explained by light limitation in deeper waters. We expected phytoplankton to die if they are exposed to dark conditions for more than 2 weeks. Thus, sinking phytoplankton have a disadvantage compared to buoyant phytoplankton, since they are more likely to become light limited and eventually die. This suggests that dredging has a negative impact on sinking plankton because it increases both depth and turbidity (de Jonge et al., 2014), which increases the aphotic depth and therefore the volume of dark water relative to the volume of illuminated water.

We suspect that the reason for the increased retention success of diel-migrating organisms is similar to the monodirectional case. When the upwards diel migration coincides with a high tide, phytoplankton are more likely to be stranded far out on the shore, reducing their risk of being washed out quickly. The higher the upward velocities, the greater the chance of being at the waterline during high tide. However, because they are sinking for half of the day, they also tend to be light limited more frequently than positively buoyant phytoplankton. It appears that these favorable and unfavorable processes balance each other out, resulting in a similar retention success to that in the monodirectional case.

Model limitations and future perspectives

In this study, we aimed to thoroughly investigate different possible retention mechanisms in a complex Lagrangian model system with a highly resolved bathymetry. Due to this computational and spatial complexity, the biological particle properties needed to remain simple to keep computational costs manageable and interpretability high and due to a lack of high-resolution validation data.

Our model design does not resolve more complex ecosystem dynamics such as nutrient limitation and grazing by higher trophic levels. The Lagrangian model is performed offline, meaning it is not coupled to the Eulerian model that calculates the hydrodynamics and is performed after the fact. Therefore, modeling the advection and dispersal of changes in concentration fields, e.g., those of nutrients (due to growth or remineralization), was not easily possible. Future modeling efforts could couple the Lagrangian model to an Eulerian model that disperses changes in concentration fields caused by biotic activity throughout the model domain. However, this would have drastically increased both the development and computational times to a point where the study would have become infeasible in our time frame and also would have required validation data that do not exist. The key drawback of this is that growth rates could only be modeled as being constant in the current model description, similar to ad libitum experiments. This can lead to systematic errors in estimating population growth. In nature, phytoplankton growth is often limited by nutrient availability, so nutrient limitation, which slows down the growth of the population, can occur, especially in the most light-saturated areas near the shore. For this reason, we may overestimate the role of shallow areas in our model.

To be consistent with the complexity of the representation of biotic mechanisms, we use a simplistic light limitation. Phytoplankton are expected to be light limited below a water depth of 1 m and not to be light limited above this threshold. We have not included a more complex light-limitation model that takes into account current light availability and attenuation. A more realistic formulation of light limitation could particularly favor phytoplankton

that exhibit diel vertical migration.

A process we mostly ignore in our study is dormancy. Our organisms can survive for 14 days in light-limited waters. However, phytoplankton species have life stages in which they can remain dormant for a long period of time and germinate again when they find themselves in more favorable waters (Thomas Anderson, 1998). In the process of choosing the light-limitation threshold, we conducted sensitivity studies testing the effect of higher light budgets. We found that light budgets of over 3 months begin to significantly increase the survivability of sinking organisms when we crudely assume that they could still reproduce under these conditions. Whether dormancy plays a significant role in an environment where the river bed is continuously dredged is unknown.

Another limitation in our modeling efforts is the lack of sub-grid-resolution structure on the shores. In our representation, we assume perfectly flat surfaces with a median distance between nodes of approximately 60 m. This "polished" model representation can lead to an underestimation of the retention success, since the surface area on which phytoplankton organisms can settle is underestimated. In nature, vegetation, rocks, or other surface irregularities provide a larger surface area on which the phytoplankton organisms can settle in moist conditions.

Our hydrodynamic dataset was limited to the year 2012. Therefore, we were not able to study different release times with the same methodology. While we do not expect the general dynamics to change, future research could examine the effect of varying the discharge throughout the seasons on retention and could address the very-long-term success (>1 year) of the population, as it is affected by inter-annual variability and climate change.

While our model does have settling and resuspension mechanics based on critical sheer velocities, we still assume a static bathymetry in which sediments are not able to move or bury phytoplankton. This masks potential losses due to phytoplankton being buried but also decreases resuspension times.

Our results clearly suggest the importance of tidal flats and shallow areas along the river banks for the persistence of primary production in the Elbe estuary. However, their effect cannot currently be quantified due to the lack of validation data. Chlorophyll data with a sufficient temporal and spatial resolution is only gathered in the center of the river. Future monitoring efforts should therefore also include data along the river shores on tidal flats or from shore to shore to quantify the effect of potential future changes caused by dredging, diking, or restoration attempts.

Frequently stranded plankton have been shown to be essential to the survival of populations in our model. However, data on their ability to survive under these conditions are scarce. Our results suggest that these conditions may be as important as their ability to quickly regrow under more favorable conditions, and we suggest that further research on plankton survivability when they are stranded is needed.

For several decades, the annual average chlorophyll concentration in the Elbe estuary has been decreasing (data available at https://www.fgg-elbe.de/elbe-datenportal.html (last access: 3 March 2024) or see (Hardenbicker et al., 2014; Schöl et al., 2014)), while upstream concentrations do not show this effect. The reasons for this are not fully understood, but one possible reason is the increase in dredging activity. This increases the average turbidity and thus the aphotic depth, reducing the volume of water in which phytoplankton can grow. A large fraction of the phytoplankton measured upstream of Hamburg port consists of diatoms (Muylaert and Sabbe, 1999), which typically have negative buoyancy (Passow, 1991), making them particularly susceptible to sinking in light-limited waters. Our finding that sinking phytoplankton have a harder time surviving in the estuary supports this theory.

Another mechanism that might, in part, explain the drop in phytoplankton concentration

at the bathymetric jump, which has not yet been explored in our model, is the phytoplankton stickiness. Phytoplankton, especially blooming phytoplankton, have been shown to be sticky due to exudates (Kiørboe and Hansen, 1993; van der Lee, 2000; Dutz et al., 2005). Some phytoplankton also produce transparent exopolymer particles, which increase their stickiness to other particles (Windler et al., 2015; De Brouwer et al., 2005). We suspect that this, in combination with the higher turbidity induced by dredging, results in losses due to plankton aggregates sticking to negatively buoyant suspended matter and subsequently sinking to the ground, where they are starved of light. A future model study could obtain estimates of the phytoplankton losses caused by this effect.

2.3.5 Conclusions

In this study, we investigated the roles of different retention strategies for phytoplankton organisms to persist in an estuarine environment. We showed that stranding in shallow nearshore areas is essential for phytoplankton retention, and that phytoplankton that are not stranded are rapidly washed away. Our model simulations suggest that growth rates much lower than those observed in nature may be sufficient to prevent population decline due to outwashing, implying that stranding may be sufficient to maintain the population. Moreover, buoyancy and strong diel vertical migration enhance retention within the estuary. These results highlight the importance of shallow nearshore areas in maintaining the productivity of estuarine ecosystems. Our results suggest that current state-of-the-art models of estuarine ecosystems may overlook an important process, and they emphasize the need for informed ecosystem-based management to avoid the degradation of estuarine ecosystems by dredging and diking activities.

2.3.6 Code and data availability

Input data can be requested from Johannes Pein (johannes.pein@hereon.de). The source code, model configuration and output are available in the Zenodo repository https://doi.org/10.25592/uhhfdm.13235. The current version of OceanTracker is available at https://github.com/oceantracker/oceantracker (last access: 3 March 2024).

Chapter 3

Synthesis

The aim of this thesis was to explore the fate of phytoplankton in the Elbe estuary - a fate which is of particular interest, as most of the upstream phytoplankton community quickly dies off after reaching the Port of Hamburg. Although this phenomenon has been observed for decades, the precise mechanisms driving this collapse remain unclear. Our investigation approached this issue from a novel perspective through Lagrangian particle tracking.

Lagrangian models represent a relatively novel approach, particularly in coastal and estuarine settings. In these environments, high spatial resolutions are essential for accurately predicting the trajectories and behavior of phytoplankton. To capture the intricate bathymetry of these environments, a unstructured, terrain-following grid is required. Historically, particle tracking using such grids has been computationally expensive, rendering more sophisticated or complex studies impractical.

The development of the ocean tracker modeling framework has enabled us to address these questions in a more effective manner. From our perspective, the primary design objective was speed. Its computational efficiency enables the scaling of larger numbers of particles on modest computer hardware within acceptable run times—something previously unattainable. Another important objective was its composability and flexibility, allowing for the easy production of ensemble studies. This is particularly vital for testing this new approach in environments largely limited by validation data.

Another noval and crucial feature was the focus on bathymetric interactions. Most Lagrangian models focused on open oceans or deeper coastal environments where collisions with the bathymetry like the sea bed or stranding are rare and implemented as an afterthought. In an estuary like the Elbe, with many shallow regions with average water levels of less then 2m, and many narrow channels these interactions are crucial to accurately represent the phytoplankton community. Considereable effort has therefore been put into the development of stranding and resuspension mechanics, which e.g. resulted in a log-layer representation of the bottom layer velocity profile to more accurately represent the critical sheer velocity for resuspension.

We developed this model, in part, with a particular application in mind. However, we designed it in such a way that it can be easily applied to a wide range of new coastal or estuarine questions, hopefully enabling many new studies.

In our second study, we employed OceanTracker to investigate the collapse of the phytoplankton community in the estuary upon reaching the port of Hamburg. We questioned the prevailing narrative that the collapse is primarily due to phytoplankton grazing. Instead, we proposed that the collapse might be partly due to the aggregation of phytoplankton with

inorganic suspended particulate matter and the subsequent sinking of these aggregates to light-limiting depths caused by the high turbidity in the navigational channel. This process is not currently represented in any existing models. To explore this hypothesis, we implemented an aggregation model into OceanTracker and assessed the relative importance of different mortality mechanisms. Our results indicate that this process might play a significant role in the phytoplankton community collapse, particularly for larger aggregates (>100 µm), suggesting that light limitation-induced mortality might be significantly higher than previously assumed. Consequently, managing turbidity in the navigational channel might be crucial in maintaining the phytoplankton community in the Elbe estuary.

In our third study, we examined the mechanisms of phytoplankton retention. We were motivated by the simple question of how phytoplankton can persist in an environment where they should be quickly washed out. The existence of phytoplankton species adapted to estuarine environments implies that there must be mechanisms allowing their persistence. To investigate the of various retention strategies for phytoplankton in an estuarine environment, we implemented several new features into OceanTracker, including the ability for particles to split to represent reproduction and improved mechanisms to simulate interactions with the bathymetry, such as settling, stranding, and resuspension. We found that shallow marshes and tidal flats play a pivotal role in the survival of the phytoplankton community in the Elbe estuary. These regions allowed phytoplankton to remain stranded for most of the tidal cycle. Phytoplankton communities that were not allowed to reproduce while being stranded could not survive in the long run and were ultimately washed out of the estuary. This suggests that careful management of these regions is essential for the stability and resilience of the phytoplankton community in the Elbe estuary.

A key limitation of our approach is the inability to effectively represent concentration changes resulting from advection and dispersion. This prevents our model from functioning as a comprehensive ecosystem model, as it cannot account for changes in factors like nutrient concentrations. Consequently, many questions we aim to address, such as the relative importance of grazing versus light limitation losses, remain out of reach and will need to be further explored using Eulerian models.

Although we were able to increase the number of represented particles by one or two orders of magnitude compared to existing models, we are still far from being able to represent realistic aggregate concentrations. Consequently, we are limited to examining subsets of these communities. Typical phytoplankton aggregate concentrations are estimated to be of the order of millions (10^6) aggregates per cubic meter. While our model is able to represent billions (10^9) of particles in the estuary over a the time span of a year, this puts us still six orders of magnitude away from representing the full community.

We hope that our study bring new impulses, both in the field of Lagrangian modeling in coastal and estuarine environments and in ecosystem management of the Elbe estuary. The lagrangian approach offers a inexpensive way of examining new hypothesis and offers a new perspective on many processes that are easily overlooked from an Eularian point of view.

Chapter 4

Appendix

4.1 Appendix A: For Study I - OceanTracker 0.5: Fast Adaptable Lagrangian Particle Tracking in Structured and Unstructured Grids

4.1.1 Code for Fig. 2.1

```
# code to run particle tracking for Fig 1

from oceantracker.main import OceanTracker # load
ot= OceanTracker() # create an instance to build parameter dictionary= ot.params

# add settings
ot.settings(output_file_base='OTpaper_exmaple_A',  root_output_dir='output', time_step= 600.)

 # add reader to acces the hyrdo-model
ot.add_class('reader',  input_dir=r'oceantracker\demos\demo_hindcast',
                file_mask=  'demoHindcastSchism*.nc')  # file mask to search for
# add a point release
ot.add_class('release_groups',name = 'my_point_release', class_name='PointRelease',
        points= [[1595000, 5482600, -2], [1594000, 5484200, -2]], # (x,y,z) of release points
        release_interval= 600, pulse_size= 5000)
# add polygon release at random depths between two z values
ot.add_class('release_groups',  name = 'my_polygon_release',  class_name='PolygonRelease',
        points=[[1597682., 5486972], [1598604, 5487275], [1598886, 5486464],
                [1597917., 5484000], [1597300, 5484000], [1597682, 5486972]],
        release_interval= 600,  pulse_size= 50, z_min= -2., z_max = 0.5)
# add grid releasing at random depths between two z values
ot.add_class('release_groups',  name = 'my_grid_release', class_name='GridRelease',
        grid_center=[1592000, 5489200], grid_span=[500, 1000], grid_size=[3, 4],
        release_interval= 1800,  pulse_size= 2, z_min= -2, z_max = -0.5)
# add a decaying particle property,# with exponential decay based on age
ot.add_class('particle_properties', name ='a_pollutant', class_name='AgeDecay',
            initial_value= 1000, decay_time_scale = 7200.) # exponential decay time scale 2hours
# add a gridded particle statistic to use as heat map
ot.add_class('particle_statistics', name = 'my_heatmap', class_name= 'GriddedStats2D_timeBased',
        grid_size=[120, 121],  release_group_centered_grids = True, update_interval = 600,
        particle_property_list = ['a_pollutant'],  status_min ='moving', z_min =-10.)
ot.add_class('resuspension', critical_friction_velocity=0.01) #set value for particle
     resupension

# run OT and return file name useful in plotting
case_info_file= ot.run()
```

4.2 Appendix B: For Study II - Effects of coagulation processes on phytoplankton mortality

4.2.1 Sensitivity analysis on the light limitation culling threshold

Figure 4.1 presents a sensitivity analysis for the light limitation culling threshold. This threshold determines the average light input required over the past 12 days to prevent phytoplankton aggregates from dying due to light limitation (see Sec. 2.3.3). We tested thresholds ranging from 10 to 100 $\mathrm{W\,m^{-2}}$ in increments of 5 $\mathrm{W\,m^{-2}}$.

Note that the threshold used in the main part of the study was 30 $\mathrm{W\,m^{-2}}$. The results indicate that this parameter is relatively insensitive compared to the initial aggregate size. However, doubling or halving the default light limitation culling threshold would cause the importance of light limitation as a cause of death to increase by about 20%, from 59% to 77%, or decrease by about 15%, from 59% to 44%, respectively.

We also observed that the relative changes in mortality causes diminish for larger thresholds, suggesting that this parameter becomes less sensitive at higher values.

The default threshold of 30 $\mathrm{W\,m^{-2}}$ is based on an assumed light compensation point of 10 $\mathrm{\mu mol\,m^{-2}\,s^{-1}}$, within a range of photosynthetically active radiation from 400 nm to 700 nm and a white light spectrum (Behrenfeld and Falkowski, 1997).

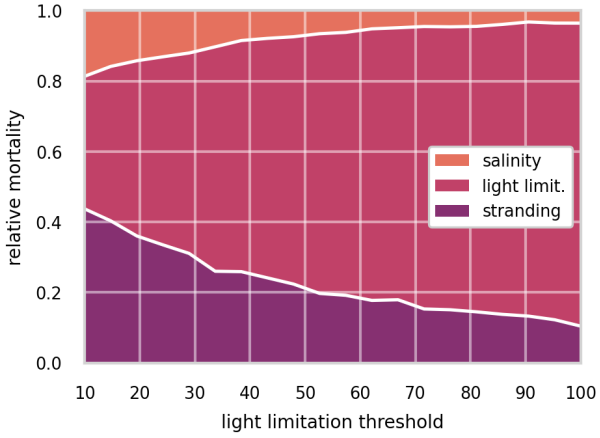

Figure 4.1: Relative cause of death for a range of light limitation thresholdes before inducing a mortality rate for an initial aggreage size of 50 µm.

4.2.2 Sensitivity analysis on the light limitation mortality rate

Figure 4.2 presents a sensitivity analysis for the light limitation mortality rate. This rate is applied to phytoplankton aggregates that have received, on average, less than 30 $\mathrm{W\,m^{-2}}$ of light in the past 12 days and is applied every 60 s (see Sec. 2.3.3). We tested values ranging from one-tenth to ten times the default rate, i.e., from $3.56 \times 10^{-6}\,\mathrm{s^{-1}}$ to $3.56 \times 10^{-4}\,\mathrm{s^{-1}}$, in 20 steps of $7.19 \times 10^{-6}\,\mathrm{s^{-1}}$. The tested initial aggregate size is 50 µm with a stickiness factor of one. Note that while we are examining a range spanning two orders of magnitude, the data is presented with linear scaling to maintain consistency with previous plots.

Our default value of $3.56 \times 10^{-5}\,\mathrm{s}^{-1}$ lies near a point of changing sensitivity. At this rate, the light limitation mortality ratio is approximately 60%. Reducing the light limitation mortality rate by a factor of 10 decreases this value to about 20%, while increasing it by a factor of 10 raises it to 80%. Halving the default value would reduce the light limitation mortality ratio to approximately 40%, while doubling it would increase the ratio to about 65%.

The chosen light limitation mortality rate is estimated based on an assumed exponential decay, as shown in the measurements presented by (Walter et al., 2017), where an average decline of 3% in cell numbers was reported after 12 days.

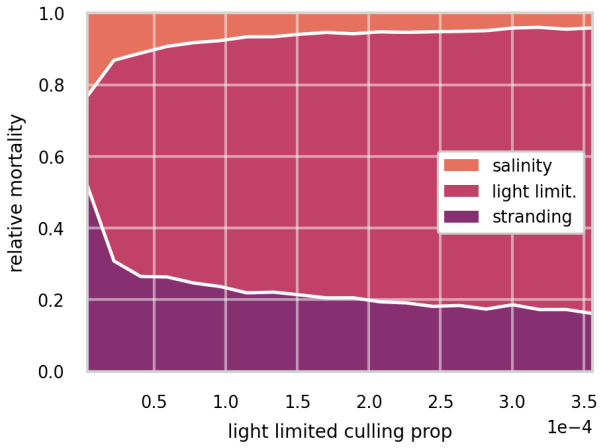

Figure 4.2: Relative cause of death for a range of light limitation mortality rates after falling below the light limitation threshold for an initial aggreage size of 50 µm

4.2.3 Sensitivity analysis on the coagulation kernel

Figure 4.3 compares the curvilinear coagulation kernel used in the study to a the simpler rectilinear kernel (see Sec. 2.3.3 for details on the coagulation kernels). We show the curvilinear kernel normalized to the rectilinear kernel for a range of partilce sizes from $1 \times 10^{-5}\,\mathrm{m}$ to $1 \times 10^{-3}\,\mathrm{m}$. Note, that the color scale is logarithmic, ranging from a ratio of 1/1000 to 1/10. As the curvilinear kernel accounts for particles avoiding each other due to the particle itself changing the flow in its proximity, effectively making particles avoid each other. Hence, the curvilinear kernels estimate smaller coagulation rates then rectilinear ones. For particles of equal size this effect reduces coagulation rates by approximatelly a factor of ten. For larger particle size differences this effects becomes more pronounced. Particles with a different in size of one order of magnitude have coagulation rates reduced by close two three orders of magnitude, while particles with a difference in size of two orders of magnitude have coagulation rates reduced by four to four orders of magnitude.

Hence, the choice between rectilinear and curvilinear kernels has an profound effect on the coagulation rates and consequently the relative importance of light limitation as a cause of death. While the curvilinear kernel are considered to me more accurate, the precise estimation of coagulations rates in a generalized form remains a challange (Burd, 2013). Nevertheless, as curvilinear kernels are strictly smaller then there rectilinear counterpart, they offer a conservative estimate on the importance of coagulation as a cause of death.

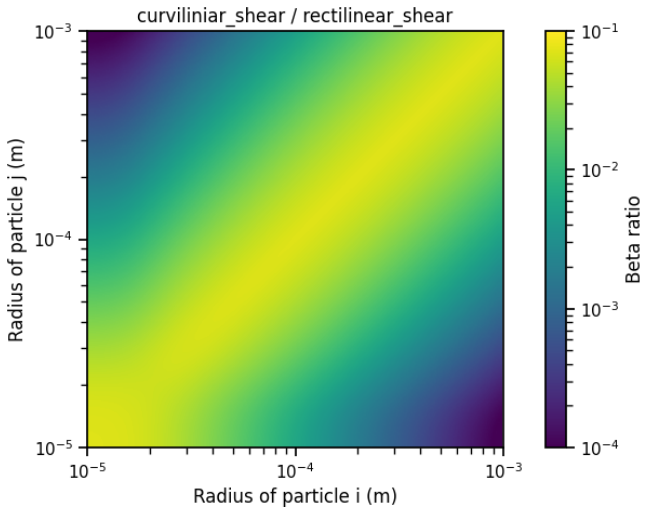

Figure 4.3: Comparison of the curvilinear coagulation kernel to the rectilinear kernel for a range of particle sizes. Note the logarithmic color scale.

4.3 Appendix C: For Study III - Phytoplankton retention mechanisms

4.3.1 Sensitivity analysis of drying out

In Fig. 4.4 and 4.5, we present the results of a sensitivity analysis of stranding mortality (i.e., due to drying out) thresholds of 1 and 14 days compared to the results for 7 days shown in Fig. 2.16. Varying this parameter changes the breakeven point of growth and loss slightly, as expected. However, no regime shift occurs, and the observed trends remain the same.

4.3.2 Sensitivity analysis of light limitation

In Fig. 4.6 and 4.7, we present the results of a sensitivity analysis of mortality thresholds due to light limitation of 7 and 28 days compared to the 14 days shown in Fig. 2.16. Similar to the stranding mortality threshold, perturbations in this parameter change the breakeven point of growth and loss as expected. Reducing the tolerated light deficit to half that observed in laboratory studies (Walter et al., 2017) has a particularly pronounced effect on sinking phytoplankton cells, which are more frequently light limited. This is most clearly visible in the -10 mm case, which shows that the breakeven point is reached at a doubling time of below 40 days. Nevertheless, the trends discussed, e.g., breakeven points at doubling times that are much larger then those observed in nature, the favoring of buoyant cells over sinking cells, and the importance of shallow areas, remain the same.

4.3.3 Salinity

Figure 4.8 shows a map of average salinity of the Elbe estuary. Salinity is averaged across depths and over the whole year.

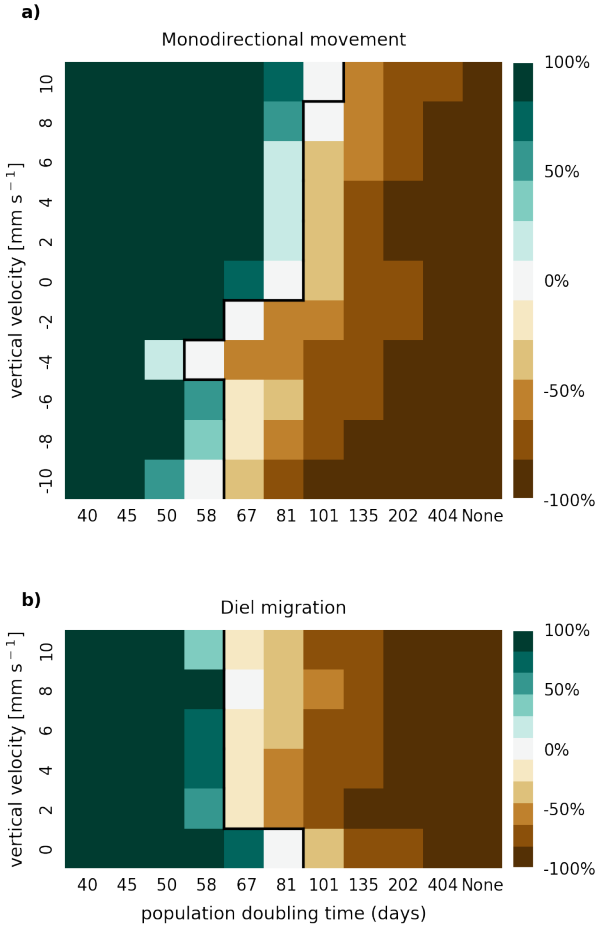

Figure 4.4: Sensitivity analysis of mortality due to stranding (i.e., drying out) showing that the retention success obtained with a threshold of 1 d without resuspension is similar to that obtained with a threshold of 7 d before phytoplankton are culled (as shown in Fig. 2.16).

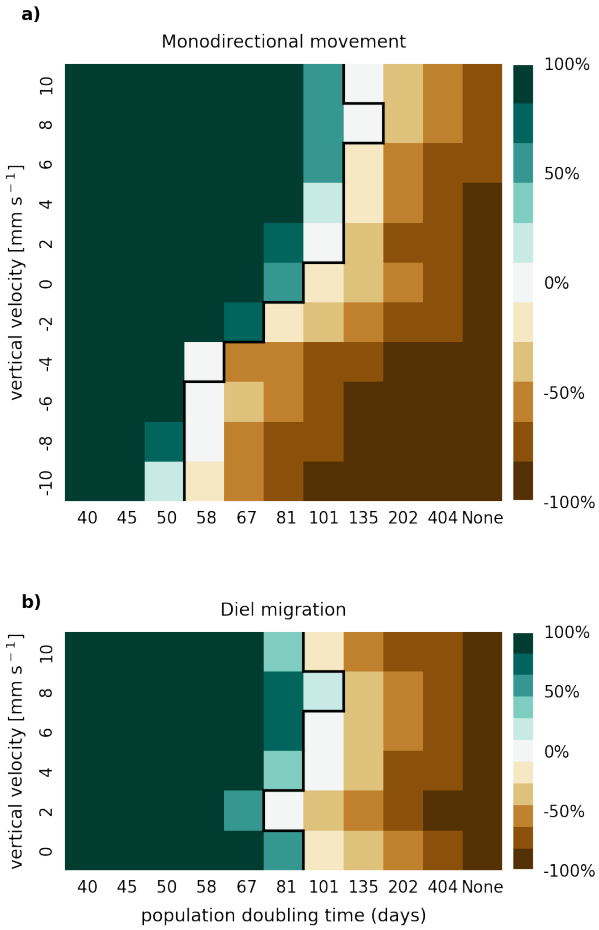

Figure 4.5: Sensitivity analysis of mortality due to stranding (i.e., drying out) showing that the retention success obtained with a threshold of 14 d without resuspension is similar to that obtained with a threshold of 7 d before phytoplankton are culled (as shown in Fig. 2.16).

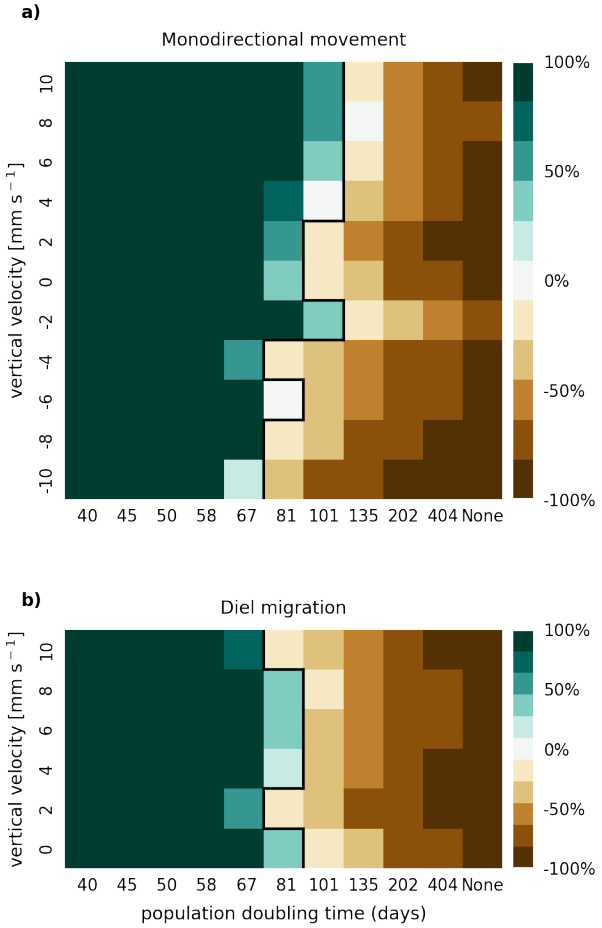

Figure 4.6: Sensitivity analysis of mortality due to light limitation showing that the retention success obtained with a light deficit threshold of 7 d is similar to that obtained with a threshold of 14 d before phytoplankton are culled (as shown in Fig. 2.16).

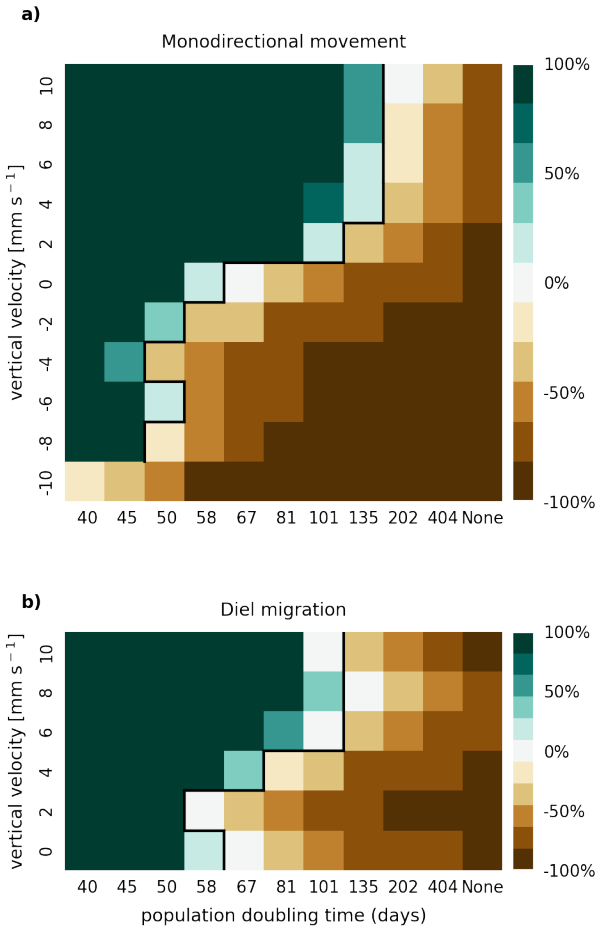

Figure 4.7: Sensitivity analysis of mortality due to light limitation showing that the retention success obtained with a light deficit threshold of 28 d is similar to that obtained with a threshold of 14 d before phytoplankton are culled (as shown in Fig. 2.16).

Figure 4.8: Salinity map of the Elbe estuary, with Hamburg's port area (as shown in Fig. 2.14) at the bottom right. Salinity is averaged across depths and over the whole year. The 20 PSU isohaline is marked with a black line. Note that this plotted area has been extended downstream compared to Fig. 2.18. Also note that the color map has been capped at 25 PSU for better visibility in low-salinity areas.

List of Figures

List of Tables

Bibliography

Surface air temperature for January 2024, URL https://climate.copernicus.eu/surface-air-temperature-january-2024, last access: 1 June 2024.

Adams, M. S., Kausch, H., Gaumert, T., and Krüger, K.-E.: The effect of the reunification of Germany on the water chemistry and ecology of selected rivers, Environmental Conservation, 23, 35–43, https://doi.org/10.1017/S0376892900038236, 1996.

Admiraal, W.: Salinity tolerance of benthic estuarine diatoms as tested with a rapid polarographic measurement of photosynthesis, Marine Biology, 39, 11–18, https://doi.org/10.1007/BF00395587, 1976.

Amann, T., Weiss, A., and Hartmann, J.: Inorganic Carbon Fluxes in the Inner Elbe Estuary, Germany, Estuaries and Coasts, 38, 192–210, https://doi.org/10.1007/s12237-014-9785-6, 2014.

Anderson, D. and Stolzenbach, K.: Selective retention of two dinoflagellates in a well-mixed estuarine embayment: the importance of diel vertical migration and surface avoidance, Marine Ecology Progress Series, 25, 39–50, https://doi.org/10.3354/meps025039, 1985.

Anderson, K. S., Hansen, C. W., Holmgren, W. F., Jensen, A. R., Mikofski, M. A., and Driesse, A.: pvlib python: 2023 project update, Journal of Open Source Software, 8, 5994, https://doi.org/10.21105/joss.05994, 2023.

Arevalo, E., Cabral, H. N., Villeneuve, B., Possémé, C., and Lepage, M.: Fish larvae dynamics in temperate estuaries: A review on processes, patterns and factors that determine recruitment, Fish and Fisheries, 24, 466–487, https://doi.org/10.1111/faf.12740, 2023.

Atalah, J., South, P. M., Briscoe, D. K., and Vennell, R.: Inferring parental areas of juvenile mussels using hydrodynamic modelling, Aquaculture, 555, 738 227, 2022.

Behrenfeld, M. J. and Falkowski, P. G.: A consumer's guide to phytoplankton primary productivity models, Limnology and Oceanography, 42, 1479–1491, https://doi.org/10.4319/lo.1997.42.7.1479, 1997.

Beller, E. E., McClenachan, L., Zavaleta, E. S., and Larsen, L. G.: Past forward: Recommendations from historical ecology for ecosystem management, Global Ecology and Conservation, 21, https://doi.org/10.1016/j.gecco.2019.e00836, 2020.

Bergemann, M. ., Blöcker, G. ., Harms, H. ., Kerner, M. ., Meyer-Nehls, R. ., Petersen, W. ., and Schroeder: Der Sauerstoffhaushalt der Tideelbe, Tech. rep., Kuratorium für Forschung im Küsteningenieurwesen (KFKI), URL https://hdl.handle.net/20.500.11970/101392, 1996.

Bernat, N., Kopcke, B., Yasseri, S., Thiel, R., and Wolfstein3, K.: TIDAL VARIATION IN BACTERIA, PHYTOPLANKTON, ZOOPLANKTON, MYSIDS, FISH AND SUSPENDED PARTICULATE MATTER IN THE TURBIDITY ZONE OF THE ELBE ESTUARY; INTERRELATIONSHIPS AND CAUSES, 1994.

Birkhofer, K., Diehl, E., Andersson, J., Ekroos, J., Früh-Müller, A., Machnikowski, F., Mader, V. L., Nilsson, L., Sasaki, K., Rundlöf, M., Wolters, V., and Smith, H. G.: Ecosystem services-current challenges and opportunities for ecological research, https://doi.org/10.3389/fevo.2014.00087, 2015.

Blauw, A. N., Los, H. F., Bokhorst, M., and Erftemeijer, P. L.: GEM: A generic ecological model for estuaries and coastal waters, Hydrobiologia, 618, 175–198, https://doi.org/10.1007/s10750-008-9575-x, 2009.

Boehlich, M. J. and Trotmann, T.: Kuratorium für Forschung im Küsteningenieurwesen (Hg.) Die Küste, 74 ICCE, Tech. rep., Kuratorium für Forschung im Küsteningenieurwesen (KFKI), URL https://hdl.handle.net/20.500.11970/101589, 2008.

Brown, A. M., Bass, A. M., and Pickard, A. E.: Anthropogenic-estuarine interactions cause disproportionate greenhouse gas production: A review of the evidence base, Marine Pollution Bulletin, 174, 113 240, https://doi.org/10.1016/j.marpolbul.2021.113240, 2022.

Burd, A. B.: Modeling particle aggregation using size class and size spectrum approaches, Journal of Geophysical Research: Oceans, 118, 3431–3443, https://doi.org/10.1002/jgrc.20255, 2013.

Burd, A. B. and Jackson, G. A.: Particle aggregation, Annual Review of Marine Science, 1, 65–90, https://doi.org/10.1146/annurev.marine.010908.163904, 2009.

Cael, B. B., Cavan, E. L., and Britten, G. L.: Reconciling the Size-Dependence of Marine Particle Sinking Speed, https://doi.org/10.1029/2020GL091771, 2021.

Carlson, D. J., Townsend, D. W., Hilyard, A. L., and Eaton, J. F.: Effect of an intertidal mudflat on plankton of the overlying water column., Canadian Journal of Fisheries and Aquatic Sciences, 41, 1523–1528, https://doi.org/10.1139/f84-188, 1984.

Casulli, V.: A high-resolution wetting and drying algorithm for free-surface hydrodynamics, International Journal for Numerical Methods in Fluids, 60, 391–408, https://doi.org/10.1002/fld.1896, 2009.

Casulli, V. and Stelling, G. S.: Semi-implicit subgrid modelling of three-dimensional free-surface flows, International Journal for Numerical Methods in Fluids, 67, 441–449, https://doi.org/10.1002/fld.2361, 2011.

Cheah, Y. T. and Chan, D. J. C.: A methodological review on the characterization of microalgal biofilm and its extracellular polymeric substances, Journal of Applied Microbiology, 132, 3490–3514, https://doi.org/10.1111/jam.15455, 2022.

Chen, T. Y. and Skoog, A.: Aggregation of organic matter in coastal waters: A dilemma of using a Couette flocculator, Continental Shelf Research, 139, 62–70, https://doi.org/10.1016/j.csr.2017.02.008, 2017.

Chen, W., Guo, F., Huang, W., Wang, J., Zhang, M., and Wu, Q.: Advances in phytoplankton population ecology in the Pearl river estuary, Frontiers in Environmental Science, 11, 1–8, https://doi.org/10.3389/fenvs.2023.1084888, 2023.

Cloern, J. E., Foster, S. Q., and Kleckner, A. E.: Phytoplankton primary production in the world's estuarine-coastal ecosystems, Biogeosciences, 11, 2477–2501, https://doi.org/10.5194/bg-11-2477-2014, 2014.

Cox, T. J., Maris, T., Engeland, T. V., Soetaert, K., and Meire, P.: Critical transitions in suspended sediment dynamics in a temperate meso-tidal estuary, Scientific Reports, 9, 1–10, https://doi.org/10.1038/s41598-019-48978-5, 2019.

Crawford, D. and Purdie, D.: Evidence for avoidance of flushing from an estuary by a planktonic, phototrophic ciliate, Marine Ecology Progress Series, 79, 259–265, https://doi.org/10.3354/meps079259, 1991.

Cullen, J. J. and Boyd, P. W.: Predicting and verifying the intended and unintended consequences of large-scale ocean iron fertilization, https://doi.org/10.3354/meps07551, 2008.

Dagestad, K.-F., Röhrs, J., Breivik, Ø., and Ådlandsvik, B.: OpenDrift v1. 0: a generic framework for trajectory modelling, Geoscience Model Development, 2018.

Dähnke, K., Bahlmann, E., and Emeis, K.: A nitrate sink in estuaries? An assessment by means of stable nitrate isotopes in the Elbe estuary, Limnology and Oceanography, 53, 1504–1511, https://doi.org/10.4319/lo.2008.53.4.1504, 2008.

De Brouwer, J. F., Wolfstein, K., Ruddy, G. K., Jones, T. E., and Stal, L. J.: Biogenic stabilization of intertidal sediments: The importance of extracellular polymeric substances produced by benthic diatoms, Microbial Ecology, 49, 501–512, https://doi.org/10.1007/s00248-004-0020-z, 2005.

De Jonge, V. and Van Beuselom, J.: Contribution of resuspended microphytobenthos to total phytoplankton in the EMS estuary and its possible role for grazers, Netherlands Journal of Sea Research, 30, 91–105, https://doi.org/10.1016/0077-7579(92)90049-K, 1992.

de Jonge, V. N., Schuttelaars, H. M., van Beusekom, J. E., Talke, S. A., and de Swart, H. E.: The influence of channel deepening on estuarine turbidity levels and dynamics, as exemplified by the Ems estuary, Estuarine, Coastal and Shelf Science, 139, 46–59, https://doi.org/10.1016/j.ecss.2013.12.030, 2014.

Delandmeter, P. and Van Sebille, E.: The Parcels v2. 0 Lagrangian framework: new field interpolation schemes, Geoscientific Model Development, 12, 3571–3584, 2019.

Deng, Z., He, Q., Safar, Z., and Chassagne, C.: The role of algae in fine sediment flocculation: In-situ and laboratory measurements, Marine Geology, 413, 71–84, https://doi.org/10.1016/j.margeo.2019.02.003, 2019.

Dutz, J., Klein Breteler, W., and Kramer, G.: Inhibition of copepod feeding by exudates and transparent exopolymer particles (TEP) derived from a Phaeocystis globosa dominated phytoplankton community, Harmful Algae, 4, 929–940, https://doi.org/10.1016/j.hal.2004.12.003, 2005.

Eick, D. and Thiel, R.: Fish assemblage patterns in the Elbe estuary: guild composition, spatial and temporal structure, and influence of environmental factors, Marine Biodiversity, 44, 559–580, https://doi.org/10.1007/s12526-014-0225-4, 2014.

Evans, M. R., Grimm, V., Johst, K., Knuuttila, T., de Langhe, R., Lessells, C. M., Merz, M., O'Malley, M. A., Orzack, S. H., Weisberg, M., Wilkinson, D. J., Wolkenhauer, O., and Benton, T. G.: Do simple models lead to generality in ecology?, https://doi.org/10.1016/j.tree.2013.05.022, 2013.

Fennessy, M. J. and Dyer, K. R.: Floc population characteristics measured with INSSEV during the Elbe estuary intercalibration experiment, Journal of Sea Research, 36, 55–62, https://doi.org/10.1016/s1385-1101(96)90771-6, 1996.

Friedlingstein, P., O'sullivan, M., Jones, M. W., Andrew, R. M., Gregor, L., Hauck, J., Quéré, C. L., Luijkx, I. T., Olsen, A., Peters, G. P., Peters, W., Pongratz, J., Schwingshackl, C., Sitch, S., Canadell, J. G., Ciais, P., Jackson, R. B., Alin, S. R., Alkama, R., Arneth, A., Arora, V. K., Bates, N. R., Becker, M., Bellouin, N., Bittig, H. C., Bopp, L., Chevallier, F., Chini, L. P., Cronin, M., Evans, W., Falk, S., Feely, R. A., Gasser, T., Gehlen, M., Gkritzalis, T., Gloege, L., Grassi, G., Gruber, N., Özgür Gürses, Harris, I., Hefner, M., Houghton, R. A., Hurtt, G. C., Iida, Y., Ilyina, T., Jain, A. K., Jersild, A., Kadono, K., Kato, E., Kennedy, D., Goldewijk, K. K., Knauer, J., Korsbakken, J. I., Landschützer, P., Lefèvre, N., Lindsay, K., Liu, J., Liu, Z., Marland, G., Mayot, N., Mcgrath, M. J., Metzl, N., Monacci, N. M., Munro, D. R., Nakaoka, S. I., Niwa, Y., O'brien, K., Ono, T., Palmer, P. I., Pan, N., Pierrot, D., Pocock, K., Poulter, B., Resplandy, L., Robertson, E., Rödenbeck, C., Rodriguez, C., Rosan, T. M., Schwinger, J., Séférian, R., Shutler, J. D., Skjelvan, I., Steinhoff, T., Sun, Q., Sutton, A. J., Sweeney, C., Takao, S., Tanhua, T., Tans, P. P., Tian, X., Tian, H., Tilbrook, B., Tsujino, H., Tubiello, F., Werf, G. R. V. D., Walker, A. P., Wanninkhof, R., Whitehead, C., Wranne, A. W., Wright, R., Yuan, W., Yue, C., Yue, X., Zaehle, S., Zeng, J., and Zheng, B.: Global Carbon Budget 2022, Earth System Science Data, 14, 4811–4900, https://doi.org/10.5194/essd-14-4811-2022, 2022.

Frieler, K., Meinshausen, M., Golly, A., Mengel, M., Lebek, K., Donner, S. D., and Hoegh-Guldberg, O.: Limiting global warming to 2C is unlikely to save most coral reefs, Nature Climate Change, 3, 165–170, https://doi.org/10.1038/nclimate1674, 2013.

Fringer, O. B., Dawson, C. N., He, R., Ralston, D. K., and Zhang, Y. J.: The future of coastal and estuarine modeling: Findings from a workshop, Ocean Modelling, 143, 101 458, https://doi.org/10.1016/j.ocemod.2019.101458, 2019.

Ganju, N. K., Brush, M. J., Rashleigh, B., Aretxabaleta, A. L., del Barrio, P., Grear, J. S., Harris, L. A., Lake, S. J., McCardell, G., O'Donnell, J., Ralston, D. K., Signell, R. P., Testa, J. M., and Vaudrey, J. M.: Progress and Challenges in Coupled Hydrodynamic-Ecological Estuarine Modeling, https://doi.org/10.1007/s12237-015-0011-y, 2016.

Goosen, N. K., Kromkamp, J., Peene, J., Van Rijswijk, P., and Van Breugel, P.: Bacterial and phytoplankton production in the maximum turbidity zone of three European estuaries: The Elbe, Westerschelde and Gironde, Journal of Marine Systems, 22, 151–171, https://doi.org/10.1016/S0924-7963(99)00038-X, 1999.

Gray, R.: Current Developments and Trends in Social and Environmental Auditing, Reporting and Attestation: A Review and Comment, International Journal of Auditing Int. J. Audit, 4, 247–268, 2000.

Gross, E., MacWilliams, M., and Kimmerer, W.: Three-Dimensional Modeling of Tidal Hydrodynamics in the San Francisco Estuary, San Francisco Estuary and Watershed Science, 7, https://doi.org/10.15447/sfews.2009v7iss2art2, 2009.

Hagy, J. D., Boynton, W. R., and Jasinski, D. A.: Modelling phytoplankton deposition to Chesapeake Bay sediments during winter-spring: Interannual variability in relation to river flow, Estuarine, Coastal and Shelf Science, 62, 25–40, https://doi.org/10.1016/j.ecss.2004.08.004, 2005.

Hall, N. S. and Paerl, H. W.: Vertical migration patterns of phytoflagellates in relation to light and nutrient availability in a shallow microtidal estuary, Marine Ecology Progress Series, 425, 1–19, https://doi.org/10.3354/meps09031, 2011.

Hall, N. S., Whipple, A. C., and Paerl, H. W.: Vertical spatio-temporal patterns of phytoplankton due to migration behaviors in two shallow, microtidal estuaries: Influence on phytoplankton function and structure, Estuarine, Coastal and Shelf Science, 162, 7–21, https://doi.org/10.1016/j.ecss.2015.03.032, 2015.

Haller, G.: Lagrangian coherent structures, Annual review of fluid mechanics, 47, 137–162, 2015.

Hardenbicker, P., Rolinski, S., Weitere, M., and Fischer, H.: Contrasting long-term trends and shifts in phytoplankton dynamics in two large rivers, International Review of Hydrobiology, 99, 287–299, https://doi.org/10.1002/iroh.201301680, 2014.

Harrison, C. S. and Glatzmaier, G. A.: Lagrangian coherent structures in the California Current System–sensitivities and limitations, Geophysical & Astrophysical Fluid Dynamics, 106, 22–44, 2012.

Hein, J. and Thomsen, J.: Contested estuary ontologies: The conflict over the fairway adaptation of the Elbe River, Germany, Environment and Planning E: Nature and Space, 6, 153–177, https://doi.org/10.1177/25148486221098825, 2023.

Hense, I. and Beckmann, A.: A theoretical investigation of the diatom cell size reduction-restitution cycle, Ecological Modelling, 317, 66–82, https://doi.org/10.1016/j.ecolmodel.2015.09.003, 2015.

Holzwarth, I. and Wirtz, K.: Anthropogenic impacts on estuarine oxygen dynamics: A model based evaluation, Estuarine, Coastal and Shelf Science, 211, 45–61, https://doi.org/10.1016/j.ecss.2018.01.020, 2018.

Holzwarth, I., Weilbeer, H., and Wirtz, K. W.: The effect of bathymetric modification on water age in the Elbe Estuary, 2019.

Hooper, D. U., Adair, E. C., Cardinale, B. J., Byrnes, J. E. K., Hungate, B. A., Matulich, K. L., Gonzalez, A., Duffy, J. E., Gamfeldt, L., and O'Connor, M. I.: A global synthesis reveals biodiversity loss as a major driver of ecosystem change, Nature, 486, 105–108, https://doi.org/10.1038/nature11118, 2012.

Horemans, D. M., Dijkstra, Y. M., Schuttelaars, H. M., Sabbe, K., Vyverman, W., Meire, P., and Cox, T. J.: Seasonal Variations in Flocculation and Erosion Affecting the Large-Scale Suspended Sediment Distribution in the Scheldt Estuary: The Importance of Biotic Effects, Journal of Geophysical Research: Oceans, 126, 1–20, https://doi.org/10.1029/2020JC016805, 2021.

HPA: Deutsches Gewässerkundliches Jahrbuch Elbegebiet, Teil III Herausgeber Freie und Hansestadt Hamburg HPA Hamburg Port Authority Hamburg, Tech. rep., 2014.

Iversonl, R. L., Landing, W. M., and Lewis, F. G.: Control of phytoplankton production and biomass in a river-dominated estuary: Apalachicola Bay, Florida, USA, 2000.

Jackson, G. A. and Burd, A. B.: Simulating aggregate dynamics in ocean biogeochemical models, Progress in Oceanography, 133, 55–65, https://doi.org/10.1016/j.pocean.2014.08.014, 2015.

Jennerjahn, T. C. and Mitchell, S. B.: Pressures, stresses, shocks and trends in estuarine ecosystems - An introduction and synthesis, Estuarine, Coastal and Shelf Science, 130, 1–8, https://doi.org/10.1016/j.ecss.2013.07.008, 2013.

Jiang, L., Gerkema, T., C. Kromkamp, J., Van Der Wal, D., Manuel Carrasco De La Cruz, P., and Soetaert, K.: Drivers of the spatial phytoplankton gradient in estuarine-coastal systems: Generic implications of a case study in a Dutch tidal bay, Biogeosciences, 17, 4135–4152, https://doi.org/10.5194/bg-17-4135-2020, 2020.

Jokulsdottir, T. and Archer, D.: A stochastic, Lagrangian model of sinking biogenic aggregates in the ocean (SLAMS 1.0): Model formulation, validation and sensitivity, Geoscientific Model Development, 9, 1455–1476, https://doi.org/10.5194/gmd-9-1455-2016, 2016.

Kappenberg, J. and Grabemann, I.: Variability of the mixing zones and estuarine turbidity maxima in the Elbe and Weser estuaries, Estuaries, 24, 699–706, https://doi.org/10.2307/1352878, 2001.

Karakaş, G., Nowald, N., Schäfer-Neth, C., Iversen, M., Barkmann, W., Fischer, G., Marchesiello, P., and Schlitzer, R.: Impact of particle aggregation on vertical fluxes of organic matter, Progress in Oceanography, 83, 331–341, https://doi.org/10.1016/j.pocean.2009.07.047, 2009.

Karr, J. R.: Defining and measuring river health, Freshwater Biology, 41, 221–234, https://doi.org/10.1046/j.1365-2427.1999.00427.x, 1999.

Kimmerer, W. J., Burau, J. R., and Bennett, W. A.: Persistence of tidally-oriented vertical migration by zooplankton in a temperate estuary, Estuaries, 25, 359–371, https://doi.org/10.1007/BF02695979, 2002.

Kimmerer, W. J., Gross, E. S., and MacWilliams, M. L.: Tidal migration and retention of estuarine zooplankton investigated using a particle-tracking model, Limnology and Oceanography, 59, 901–916, https://doi.org/10.4319/lo.2014.59.3.0901, 2014.

Kiørboe, T. and Hansen, J. L.: Phytoplankton aggregate formation: Observations of patterns and mechanisms of cell sticking and the significance of exopolymeric material, Journal of Plankton Research, 15, 993–1018, https://doi.org/10.1093/plankt/15.9.993, 1993.

Knight, B. R., Zyngfogel, R., Forrest, B., et al.: PartTracker-a fate analysis tool for marine particles, Coasts and Ports 2009: In a Dynamic Environment, p. 186, 2009.

Koch, R. W., Guelda, D. L., and Bukaveckas, P. A.: Phytoplankton growth in the Ohio, Cumberland and Tennessee Rivers, USA: Inter-site differences in light and nutrient limitation, Aquatic Ecology, 38, 17–26, https://doi.org/10.1023/B:AECO.0000021082.42784.03, 2004.

Kooten, G. C. V. and Sohngen, B.: Economics of Forest Ecosystem Carbon Sinks: A Review, 2007.

Kopmann and für Wasserbau, B.: ICHE 2014, 2014.

Krieger, M.: Geschichte Hamburgs, C.H. Beck, 1 edn., 2006.

Kriest, I.: Different parameterizations of marine snow in a 1D-model and their influence on representation of marine snow, nitrogen budget and sedimentation, 2002.

Kromkamp, J., Peene, J., van Rijswijk, P., Sandee, A., and Goosen, N.: Nutrients, light and primary production by phytoplankton and microphytobenthos in the eutrophic, turbid Westerschelde estuary (The Netherlands), Hydrobiologia, 311, 9–19, https://doi.org/10.1007/BF00008567, 1995.

Lai, Z., Chen, C., Cowles, G. W., and Beardsley, R. C.: A nonhydrostatic version of FVCOM: 1. Validation experiments, Journal of Geophysical Research: Oceans, 115, 2010.

Lam, S. K., Pitrou, A., and Seibert, S.: Numba : A LLVM-based Python JIT Compiler, https://doi.org/10.1145/2833157.2833162, 2015a.

Lam, S. K., Pitrou, A., and Seibert, S.: Numba: A llvm-based python jit compiler, in: Proceedings of the Second Workshop on the LLVM Compiler Infrastructure in HPC, pp. 1–6, 2015b.

Laurenceau-Cornec, E. C., Moigne, F. A. L., Gallinari, M., Moriceau, B., Toullec, J., Iversen, M. H., Engel, A., and Rocha, C. L. D. L.: New guidelines for the application of Stokes' models to the sinking velocity of marine aggregates, Limnology and Oceanography, 65, 1264–1285, https://doi.org/10.1002/lno.11388, 2020.

Logan, B. E., Passow, U., Alldredge, A. L., Grossarts, . H.-P., and Simon+, M.: Rapid formation and sedimentation of large aggregates is predictable from coagulation rates (half-lives) of transparent exopolymer particles (TEP), 1995.

López, A. G., Wilkin, J. L., and Levin, J. C.: Doppio-a ROMS (v3.6)-based circulation model for the Mid-Atlantic Bight and Gulf of Maine: Configuration and comparison to integrated coastal observing network observations, Geoscientific Model Development, 13, 3709–3729, https://doi.org/10.5194/gmd-13-3709-2020, 2020.

Lucas, L. V. and Deleersnijder, E.: Timescale methods for simplifying, understanding and modeling biophysical and water quality processes in coastal aquatic ecosystems: A review, Water, 12, 2717, 2020.

Lynch, D. R., Greenberg, D. A., Bilgili, A., McGillicuddy Jr, D. J., Manning, J. P., and Aretxabaleta, A. L.: Particles in the coastal ocean: Theory and applications, Cambridge University Press, 2014.

MacWilliams, M. L., Ateljevich, E. S., Monismith, S. G., and Enright, C.: An Overview of Multi-Dimensional Models of the Sacramento–San Joaquin Delta, San Francisco Estuary and Watershed Science, 14, https://doi.org/10.15447/sfews.2016v14iss4art2, 2016.

Malcherek, A., Piechotta, F., and Knoch, D.: Mathematical Module SediMorph Validation Document-Version 1.1, Tech. rep., The Federal Waterways Engineering and Research Institute (BAW), 2005.

Martens, N., Russnak, V., Woodhouse, J., Grossart, H.-P., and Schaum, C.-E.: Metabarcoding reveals potentially mixotrophic flagellates and picophytoplankton as key groups of phytoplankton in the Elbe estuary, Environmental Research, 252, 119 126, https://doi.org/10.1016/j.envres.2024.119126, 2024.

Matthies, M., Berlekamp, J., Lautenbach, S., Graf, N., and Reimer, S.: System analysis of water quality management for the Elbe river basin, Environmental Modelling and Software, 21, 1309–1318, https://doi.org/10.1016/j.envsoft.2005.04.026, 2006.

McGuire, A. D., Lawrence, D. M., Koven, C., Clein, J. S., Burke, E., Chen, G., Jafarov, E., MacDougall, A. H., Marchenko, S., Nicolsky, D., Peng, S., Rinke, A., Ciais, P., Gouttevin, I., Hayes, D. J., Ji, D., Krinner, G., Moore, J. C., Romanovsky, V., Schädel, C., Schaefer, K., Schuur, E. A., and Zhuang, Q.: Dependence of the evolution of carbon dynamics in the northern permafrost region on the trajectory of climate change, Proceedings of the National Academy of Sciences of the United States of America, 115, 3882–3887, https://doi.org/10.1073/pnas.1719903115, 2018.

McIntosh, R. P.: The Background of Ecology, Cambridge University Press, https://doi.org/10.1017/CBO9780511608537, 1985.

Middelburg, J. J. and Herman, P. M.: Organic matter processing in tidal estuaries, Marine Chemistry, 106, 127–147, https://doi.org/10.1016/j.marchem.2006.02.007, 2007.

Moore, A. M., Arango, H. G., Broquet, G., Powell, B. S., Weaver, A. T., and Zavala-Garay, J.: The Regional Ocean Modeling System (ROMS) 4-dimensional variational data assimilation systems: Part I–System overview and formulation, Progress in Oceanography, 91, 34–49, 2011.

Muylaert, K. and Sabbe, K.: Spring phytoplankton assemblages in and around the maximum turbidity zone of the estuaries of the Elbe (Germany), the Schelde (Belgium/The Netherlands) and the Gironde (France), Journal of Marine Systems, 22, 133–149, https://doi.org/10.1016/S0924-7963(99)00037-8, 1999.

Naeem, S., Ingram, J. C., Varga, A., Agardy, T., Barten, P., Bennett, G., Bloomgarden, E., Bremer, L. L., Burkill, P., Cattau, M., Ching, C., Colby, M., Cook, D. C., Costanza, R., DeClerck, F., Freund, C., Gartner, T., Goldman-Benner, R., Gunderson, J., Jarrett, D., Kinzig, A. P., Kiss, A., Koontz, A., Kumar, P., Lasky, J. R., Masozera, M., Meyers, D., Milano, F., Naughton-Treves, L., Nichols, E., Olander, L., Olmsted, P., Perge, E., Perrings, C., Polasky, S., Potent, J., Prager, C., Quétier, F., Redford, K., Saterson, K., Thoumi, G., Vargas, M. T., Vickerman, S., Weisser, W., Wilkie, D., and Wunder, S.: Get the science right when paying for nature's services: Few projects adequately address design and evaluation, https://doi.org/10.1126/science.aaa1403, 2015.

Neumann, A., Hass, H. C., Möbius, J., and Naderipour, C.: Ballasted flocs capture pelagic primary production and alter the local sediment characteristics in the coastal German bight (North sea), Geosciences (Switzerland), 9, https://doi.org/10.3390/geosciences9080344, 2019.

Nienhuis, P. H., Smaal, A. C., and Knoester, M.: The Oosterschelde estuary: an evaluation of changes at the ecosystem level induced by civil-engineering works, Hydrobiologia, 282-283, 575–592, https://doi.org/10.1007/BF00024657, 1994.

Nightingale, L.: ONE HUNDRED PORTS 2022, URL https://lloydslist.com/one-hundred-container-ports-2022, 2022.

Noormets, A., Epron, D., Domec, J. C., McNulty, S. G., Fox, T., Sun, G., and King, J. S.: Effects of forest management on productivity and carbon sequestration: A review and hypothesis, https://doi.org/10.1016/j.foreco.2015.05.019, 2014.

Passow, U.: Species-specific sedimentation and sinking velocities of diatoms, Marine Biology, 108, 449–455, https://doi.org/10.1007/BF01313655, 1991.

Passow, U., Alldredge, A. L., and Logant, B. E.: The role of particulate carbohydrate exudates in the flocculation of diatom blooms, 1994.

Pein, J., Eisele, A., Hofmeister, R., Sanders, T., Daewel, U., Stanev, E. V., Beusekom, J. V., Staneva, J., and Schrum, C.: Nitrogen cycling in the Elbe estuary from a joint 3D-modelling and observational perspective, Biogeosciences Discussions, 2019, 1–34, https://doi.org/10.5194/bg-2019-265, 2019.

Pein, J., Eisele, A., Sanders, T., Daewel, U., Stanev, E. V., van Beusekom, J. E. E., Staneva, J., and Schrum, C.: Seasonal Stratification and Biogeochemical Turnover in the Freshwater Reach of a Partially Mixed Dredged Estuary, Frontiers in Marine Science, 8, https://doi.org/10.3389/fmars.2021.623714, 2021.

Pilarczyk, K. W.: Impact of the Delta Works on the Recent Developments in Coastal Engineering, pp. 1–37, WORLD SCIENTIFIC, https://doi.org/10.1142/9789814360579_0001, 2012.

Planchat, A., Kwiatkowski, L., Bopp, L., Torres, O., Christian, J. R., Butenschön, M., Lovato, T., Séférian, R., Chamberlain, M. A., Aumont, O., Watanabe, M., Yamamoto, A., Yool, A., Ilyina, T., Tsujino, H., Krumhardt, K. M., Schwinger, J., Tjiputra, J., Dunne, J. P., and Stock, C.: The representation of alkalinity and the carbonate pump from CMIP5 to CMIP6 Earth system models and implications for the carbon cycle, Biogeosciences, 20, 1195–1257, https://doi.org/10.5194/bg-20-1195-2023, 2023.

Postma, L., Boderie, P. M. A., van Gils, J. A. G., and van Beek, J. K. L.: Component Software Systems for Surface Water Simulation, pp. 649–658, https://doi.org/10.1007/3-540-44860-8_67, 2003.

Pusch, M. and Fischer, H.: Stoffdynamik und Habitatstruktur in der Elbe, vol. 5, Weißensee Verlag, 2006.

Quiel, K., Becker, A., Kirchesch, V., Schöl, A., and Fischer, H.: Influence of global change on phytoplankton and nutrient cycling in the Elbe River, Regional Environmental Change, 11, 405–421, https://doi.org/10.1007/s10113-010-0152-2, 2011.

Ratter, B. and Weig, B.: Die Tide-Elbe - ein Kultur-, Natur- und Wirtschaftsraum aus Sicht der Bevölkerung, BAW, 2012.

Renes, J.: Niederländische Einflüsse auf Kulturlandschaften Europas, Diffusion oder Kolonisation; holländische Wege durch die Jahrhunderte in Mitteleuropa; Tagung am 19. Januar, Museum Altes Land, Jork, pp. 82–87, 2013.

Ross, O. N. and Sharples, J.: Recipe for 1-D Lagrangian particle tracking models in space-varying diffusivity, Limnology and Oceanography: Methods, 2, 289–302, 2004.

Sanders, T., Schöl, A., and Dähnke, K.: Hot Spots of Nitrification in the Elbe Estuary and Their Impact on Nitrate Regeneration, Estuaries and Coasts, 41, 128–138, https://doi.org/10.1007/s12237-017-0264-8, 2018.

Savelli, R., Bertin, X., Orvain, F., Gernez, P., Dale, A., Coulombier, T., Pineau, P., Lachaussée, N., Polsenaere, P., Dupuy, C., and le Fouest, V.: Impact of Chronic and Massive Resuspension Mechanisms on the Microphytobenthos Dynamics in a Temperate Intertidal Mudflat, Journal of Geophysical Research: Biogeosciences, 124, 3752–3777, https://doi.org/10.1029/2019JG005369, 2019.

Schartau, M., Riethmüller, R., Flöser, G., van Beusekom, J. E., Krasemann, H., Hofmeister, R., and Wirtz, K.: On the separation between inorganic and organic fractions of suspended matter in a marine coastal environment, Progress in Oceanography, 171, 231–250, https://doi.org/10.1016/j.pocean.2018.12.011, 2019.

Schöl, A., Hein, B., Wyrwa, J., and Kirchesch, V.: Modelling Water Quality in the Elbe and its Estuary – Large Scale and Long Term Applications with Focus on the Oxygen Budget of the Estuary, 81, 203–232, 2014.

Schroeder, F.: Water quality in the Elbe estuary: Significance of different processes for the oxygen deficit at Hamburg, Environmental Modeling and Assessment, 2, 73–82, https://doi.org/10.1023/a:1019032504922, 1997.

Schrum, C., John, M. S., and Alekseeva, I.: ECOSMO, a coupled ecosystem model of the North Sea and Baltic Sea: Part II. Spatial-seasonal characteristics in the North Sea as revealed by EOF analysis, Journal of Marine Systems, 61, 100–113, https://doi.org/10.1016/j.jmarsys.2006.01.004, 2006.

Sehili, A., Lang, G., and Lippert, C.: High-resolution subgrid models: Background, grid generation, and implementation, Ocean Dynamics, 64, 519–535, https://doi.org/10.1007/s10236-014-0693-x, 2014.

Sha, Z., Bai, Y., Li, R., Lan, H., Zhang, X., Li, J., Liu, X., Chang, S., and Xie, Y.: The global carbon sink potential of terrestrial vegetation can be increased substantially by optimal land management, Communications Earth and Environment, 3, https://doi.org/10.1038/s43247-021-00333-1, 2022.

Simons, R. D., Monismith, S. G., Johnson, L. E., Winkler, G., and Saucier, F. J.: Zooplankton retention in the estuarine transition zone of the St. Lawrence Estuary, Limnology and Oceanography, 51, 2621–2631, https://doi.org/10.4319/lo.2006.51.6.2621, 2006.

Smaal, A. C., Knoester, M., Nienhuis, P. H., and Meire, P. M.: Changes in the Oosterschelde ecosystem induced by the Delta works, 1991.

Smits, J. G. and van Beek, J. K.: ECO: A Generic Eutrophication Model Including Comprehensive Sediment-Water Interaction, PLoS ONE, 8, https://doi.org/10.1371/journal.pone.0068104, 2013.

Spieckermann, M., Gröngröft, A., Karrasch, M., Neumann, A., and Eschenbach, A.: Oxygen Consumption of Resuspended Sediments of the Upper Elbe Estuary: Process Identification and Prognosis, Aquatic Geochemistry, 28, https://doi.org/10.1007/s10498-021-09401-6, 2022.

Stanev, E. V., Jacob, B., and Pein, J.: German Bight estuaries : An inter-comparison on the basis of numerical modeling, Continental Shelf Research, 174, 48–65, https://doi.org/10.1016/j.csr.2019.01.001, 2019.

Steidle, L. and Vennell, R.: Phytoplankton retention mechanisms in estuaries: A case study of the Elbe estuary, Nonlinear Processes in Geophysics, 31, 151–164, https://doi.org/10.5194/npg-31-151-2024, 2024.

Stemmann, L., Jackson, G. A., and Ianson, D.: A vertical model of particle size distributions and fluxes in the midwater column that includes biological and physical processes - Part I: Model formulation, Deep-Sea Research Part I: Oceanographic Research Papers, 51, 865–884, https://doi.org/10.1016/j.dsr.2004.03.001, 2004.

Thomas Anderson, J.: The effect of seasonal variability on the germination and vertical transport of a cyst forming dinoflagellate, Gyrodinium sp., in the Chesapeake Bay, Ecological Modelling, 112, 85–109, https://doi.org/10.1016/S0304-3800(98)00074-X, 1998.

Thygesen, U. H.: How to reverse time in stochastic particle tracking models, Journal of Marine Systems, 88, 159–168, 2011.

van der Lee, W.: Parameters affecting mud floc size on a seasonal time scale: The impact of a phytoplankton bloom in the Dollard estuary, The Netherlands, in: Coastal adn Estuarine Fine Sediment Processes, 1989, pp. 403–421, https://doi.org/10.1016/S1568-2692(00)80134-5, 2000.

Van Sebille, E., Griffies, S. M., Abernathey, R., Adams, T. P., Berloff, P., Biastoch, A., Blanke, B., Chassignet, E. P., Cheng, Y., Cotter, C. J., et al.: Lagrangian ocean analysis: Fundamentals and practices, Ocean Modelling, 121, 49–75, 2018.

Vennell, R., Unwin, H., and Scheel, M.: Where's Our Plastic Going?, URL http://www.oceanplasticsimulator.nz, 2019.

Vennell, R., Scheel, M., Weppe, S., Knight, B., and Smeaton, M.: Fast lagrangian particle tracking in unstructured ocean model grids, Ocean Dynamics, 71, 423–437, https://doi.org/10.1007/s10236-020-01436-7, 2021.

von Alvensleben, N., Magnusson, M., and Heimann, K.: Salinity tolerance of four freshwater microalgal species and the effects of salinity and nutrient limitation on biochemical profiles, Journal of Applied Phycology, 28, 861–876, https://doi.org/10.1007/s10811-015-0666-6, 2016.

Walter, B., Peters, J., and van Beusekom, J. E.: The effect of constant darkness and short light periods on the survival and physiological fitness of two phytoplankton species and their growth potential after re-illumination, Aquatic Ecology, 51, 591–603, https://doi.org/10.1007/s10452-017-9638-z, 2017.

Warner, J. C., Geyer, W. R., and Lerczak, J. A.: Numerical modeling of an estuary: A comprehensive skill assessment, Journal of Geophysical Research: Oceans, 110, 1–13, https://doi.org/10.1029/2004JC002691, 2005.

Weilbeer, H., Winterscheid, A., Strotmann, T., Entelmann, I., Shaikh, S., and Vaessen, B.: Analyse der hydrologischen und morphologischen Entwicklung in der Tideelbe für den Zeitraum von 2013 bis 2018, Die Küste, 89, 57–129, URL https://doi.org/10.18171/1.089104., 2021.

Wilson, J. G.: Productivity, fisheries and aquaculture in temperate estuaries, Estuarine, Coastal and Shelf Science, 55, 953–967, https://doi.org/10.1006/ecss.2002.1038, 2002.

Winder, M. and Sommer, U.: Phytoplankton response to a changing climate, https://doi.org/10.1007/s10750-012-1149-2, 2012.

Windler, M., Leinweber, K., Bartulos, C. R., Philipp, B., and Kroth, P. G.: Biofilm and capsule formation of the diatom Achnanthidium minutissimum are affected by a bacterium, Journal of Phycology, 51, 343–355, https://doi.org/10.1111/jpy.12280, 2015.

Wirtz, K. W.: Non-uniform scaling in phytoplankton growth rate due to intracellular light and CO 2 decline, Journal of Plankton Research, 33, 1325–1341, https://doi.org/10.1093/plankt/fbr021, 2011.

Wolfram, P. J., Ringler, T. D., Maltrud, M. E., Jacobsen, D. W., and Petersen, M. R.: Diagnosing isopycnal diffusivity in an eddying, idealized midlatitude ocean basin via Lagrangian, in Situ, Global, High-Performance Particle Tracking (LIGHT), Journal of Physical Oceanography, 45, 2114–2133, 2015.

Yamazaki, H., Locke, C., Umlauf, L., Burchard, H., Ishimaru, T., and Kamykowski, D.: A Lagrangian model for phototaxis-induced thin layer formation, Deep Sea Research Part II: Topical Studies in Oceanography, 101, 193–206, https://doi.org/10.1016/j.dsr2.2012.12.010, 2014.

Ye, F., Zhang, Y. J., Wang, H. V., Friedrichs, M. A., Irby, I. D., Alteljevich, E., Valle-Levinson, A., Wang, Z., Huang, H., Shen, J., and Du, J.: A 3D unstructured-grid model for Chesapeake Bay: Importance of bathymetry, Ocean Modelling, 127, 16–39, https://doi.org/10.1016/j.ocemod.2018.05.002, 2018.

Zhang, Y. J., Ye, F., Stanev, E. V., and Grashorn, S.: Seamless cross-scale modeling with SCHISM, Ocean Modelling, 102, 64–81, https://doi.org/10.1016/j.ocemod.2016.05.002, 2016.